Karlsruher Institut für Technologie

Fakultät für Physik
Institut für Theorie der Kondensierten Materie

Quantum phase transitions in topological Josephson junctions

Zur Erlangung des akademischen Grades eines

DOKTORS DER NATURWISSENSCHAFTEN (Dr. rer. nat.)

von der KIT-Fakultät für Physik des
Karlsruher Instituts für Technologie (KIT)
angenommene

Dissertation

von
M. Sc. Adrian Reich

Tag der mündlichen Prüfung: 18. Juli 2025
Referent: Prof. Dr. Alexander Shnirman
Korreferent: Prof. Dr. Jörg Schmalian

Erklärung:

Ich versichere wahrheitsgemäß, die Arbeit selbstständig verfasst, alle benutzten Hilfsmittel vollständig und genau angegeben und alles kenntlich gemacht zu haben, was aus Arbeiten anderer unverändert oder mit Abänderungen entnommen wurde sowie die Satzung des KIT zur Sicherung guter wissenschaftlicher Praxis in der Fassung vom 30.09.2021 beachtet zu haben.

Ort, Datum	Unterschrift

List of Publications

Until the date of my thesis defense, I co-authored the following peer-reviewed publications, listed in reverse chronological order

- Ref. [114]: K. Piasotski, O. Lesser, **A. Reich**, P. Ostrovsky, E. Grosfeld, Y. Makhlin, Y. Oreg, and A. Shnirman, *Current flow in topological insulator Josephson junctions due to imperfections.* Phys. Rev. B 111, 174527 (2025)
- Ref. [98]: **A. Reich**, D. S. Shapiro, and A. Shnirman, *Berezinskii-Kosterlitz-Thouless transitions in a topological superconductor-ferromagnet-superconductor junction.* Phys. Rev. B 111, 205428 (2025)
- Ref. [47]: G. F. R. Ruiz, **A. Reich**, A. Shnirman, J. Schmalian, and L. Arrachea, *Binding zero modes with fluxons in Josephson junctions of time-reversal invariant topological superconductors.* Phys. Rev. B 110, 245427 (2024)
- Ref. [46]: **A. Reich**, E. Berg, J. Schmalian, and A. Shnirman, *Magnetization dynamics and Peierls instability in topological Josephson structures.* Phys. Rev. B 107, 245411 (2023)

as well as the preprint

- K. Piasotski, **A. Reich**, and A. Shnirman, *Topological Josephson vortices at finite voltage bias.* arXiv:2502.02192 (2025) (not cited in the thesis)

Contents

1

Chapter 1

Introduction

The story of Ettore Majorana's disappearance during a boat trip in 1938 is a notoriously enigmatic one, having prompted speculations and debate spanning several decades. [1–3] As fate would have it, this mystery is only accentuated by the fact that the type of particles he proposed in his last published paper [4] even more so continues to puzzle the physics community across a variety of disciplines, as they remain elusive to this day.

Majorana particles serve as an alternative to the realization of relativistic fermions introduced by Dirac. By deducing a representation of the Dirac equation which is solved by real-valued wave functions, Majorana opened the possibility for the existence of electrically neutral spin-$\frac{1}{2}$ fermions, which behave as their own antiparticles.

In the realm of particle physics, these types of elementary excitations are not part of the Standard Model, but only appear in extensions to it as e.g. possible solution to the neutrino mass problem or dark matter candidates. [5] In contrast, in condensed matter physics quasiparticles with Majorana character naturally emerge in the theory of superconductivity as coherent superpositions of electrons and holes.

Based on that, at the turn of the millennium it was realized that superconductors with pairing symmetries going beyond the standard Bardeen-Cooper-Schrieffer (BCS) mechanism [6] are able to host localized Majorana bound states at vortex cores or boundaries. [7–10] On top of being described by Majorana operators, these are furthermore expected to have the fascinating property of constituting non-abelian anyons, exhibiting exchange statistics which are neither fermionic nor bosonic. [9, 10] Realizing and controlling such exotic states in fact entails practical visions of allowing for fault-tolerant and topologically protected quantum computing [11], attracting not only academic but also prominent industrial research [12].

However, the quest for Majorana bound states in superconducting systems has not been in full swing until 2008, when Fu and Kane showed in their groundbreaking paper [13] that unconventional superconductors are not a strictly necessary requisite for this endeavor, but that effective topological superconductivity is achievable instead by means of ordinary s-wave superconductors in combination with the spin-momentum locked surface states of a topological insulator. This realization cleared the way for a large variety of experiments and theoretical proposals harnessing the superconducting proximity effect in a similar vein. [14]

Systems of particular significance in this regard are Josephson junctions formed within these topological structures. Depending on the details, they are able to host one-dimensional Majorana edge modes propagating along the junction as well as zero-dimensional Majorana bound states localized in Josephson vortices. The well-understood and rich landscape of experimentally accessible quantum phenomena in Josephson junctions then naturally lends itself as a testing ground and control platform for the coveted Majorana physics.

While the fabrication of such junctions on topological insulator surfaces has been carried out in several works, including characterization via the measurements of Josephson current [15–18], Shapiro steps [19] and Fraunhofer diffraction patterns [20, 21], conclusive proof of the existence of Majorana bound states, in particular distinguishing them from topologically trivial Andreev modes (let alone determining their non-abelian nature), continues to elude experiments.

In this thesis, in an effort to advance our theoretical understanding of these compelling structures, we extend the theoretical models for topological Josephson systems by including the dynamics of bosonic fields which couple to the one-dimensional Majorana modes propagating along the junction. In our analysis of the resulting field theories, we find evidence for the existence of a variety of quantum phase transitions. Furthermore, we establish a regime in which the frequently used effective description in terms of two counter-propagating Majorana modes is no longer applicable due to an emergence of additional low-energy degrees of freedom, previously overlooked.

Our main focus will lie on Josephson junctions on the surface of a three-dimensional strong topological insulator with a ferromagnet embedded between the two superconductors. Such a setup has in the past been proposed [22–25] as a means to manipulate and control the electronic surface states with a static magnetization. Since the magnetization in a ferromagnet is however not perfectly rigid, our aim is to deduce a theory which incorporates the dynamical magnetic degrees of freedom on equal footing with the electronic ones, in order to study the macroscopic consequences of their interplay. A similar model for the coupling between phase bias and edge modes in junctions of time-reversal invariant topological superconductors will be examined as well, in addition to the case of these junctions being subjected to an external magnetic field.

To this end, we begin in **Chapter 2** by introducing the already mentioned connections between topology, superconductivity and Majorana modes in more detail in order to establish the framework within which the subsequent chapters operate. Particularly, after providing a brief overview of the ideas that lead to the notion of topological insulators and topological superconductivity, we introduce the Fu-Kane system [13] and present how one- and zero-dimensional Majorana states can emerge there.

In **Chapter 3**, we introduce the topological superconductor-ferromagnet-superconductor (SMS) junctions and derive a corresponding low-energy effective theory in the case of a strong magnetic easy-axis anisotropy. Within mean-field theory, a Peierls instability ensuing a $\mathbb{Z}_2$ symmetry breaking with a tilting of the magnetization and opening of a Majorana mass gap can be identified, which we examine for its stability to deduce an estimate for the associated quantum phase diagram. A similar analysis is carried out for Josephson junctions comprised of time-reversal invariant topological superconductors. Both systems are finally investigated for the fermionic bound states carried by solitonic excitations.

Chapter 4 extends the considerations concerning the topological SMS junctions to allow for arbitrary magnetic anisotropy strengths. Employing a combination of mean-field and renormalization group arguments, we find Berezinskii-Kosterlitz-Thouless transitions to be present in both the easy-plane and weak easy-axis regime. In an effort to join these results with the above mentioned Peierls instability, we speculate on the existence of exotic multicritical points in the model.

Finally, in **Chapter 5** a fundamental limitation of the effective theory, which is employed here and in various other works, is pointed out using the example of a topological insulator Josephson junction threaded by a magnetic flux. Particularly, we show the naive low-energy approximation to fail for small effective velocities of the Majorana modes. While part of the resulting erroneous predictions can be remedied by the inclusion of higher-order corrections, we furthermore unveil a behavior reminiscent of a topological phase transition, which is completely missed by the usual approach.

Chapter 6 concludes the thesis and contains outlook for potential future research.

Chapter 2

2 Fundamentals: Josephson junctions on the surface of a topological insulator

To set the stage for this thesis, we begin by introducing the physical systems which will be of interest to us. We discuss the connection between unconventional superconductors, topology and Majorana modes in condensed matter systems and touch on why these quasiparticles have attracted an immense amount of attention in the recent decades. Next, we present the ingenious setup proposed by Liang Fu and Charles Kane, comprised of ordinary s-wave superconductors and three-dimensional topological insulators, which is able to host Majorana modes. Based on this, we finally turn to the structures which will be our main focus, namely Josephson junctions on the surface of a topological insulator. We introduce the associated central concepts and ideas, which makes us ready to dive into the main part of this thesis, in which we investigate its potential as a platform for a variety of quantum critical phenomena.

In Section 2.1 of this chapter, we loosely follow the review articles by Hasan and Kane [26], Alicea [14] and Aguado [27]. For a more thorough introduction to the topic, we refer the reader to these papers as well as the references cited therein.

2.1 Topological superconductivity and Majorana modes

2.1.1 Topological insulators

An (ordinary) insulator is characterized by the energy gap between its valence and conduction band. The same is true for the semiconducting band structure, which we can easily imagine to be obtained by a continuous deformation from an insulating state. In fact, deforming the gap to be as large as the energy required for electron-positron pair production, there is a sense in which we can even smoothly deform between an insulator and the vacuum. This is the basic idea on grounds of which the notion of a topological equivalency class can be defined, asking the question whether two band structures can be smoothly deformed into one another without closing the energy gap. Thus, ordinary insulators, semiconductors and the vacuum are from this topological point of view equivalent.

To be more precise, let us understand the band structure of a two-dimensional material as a mapping from the crystal momentum $\boldsymbol{k}$ in the first Brillouin zone (defined on a torus) to the Bloch Hamiltonian $\mathcal{H}(\boldsymbol{k})$, the eigenvalues $E_n(\boldsymbol{k})$ of which form bands indexed by n. The goal is now to define a quantity which is invariant under changes of $\mathcal{H}(\boldsymbol{k})$ which leave the energy gap intact, called a topological invariant.

One example of such a topological invariant is given by the total Berry flux $\mathcal{F}_m = \nabla_{\boldsymbol{k}} \times \mathcal{A}_m$ in the first Brillouin zone

$$N = \frac{1}{2\pi} \sum_{m \text{ occ.}} \int d^2k\, \mathcal{F}_m, \tag{2.1}$$

with $\mathcal{A}_m = i \langle u_m | \nabla_{\boldsymbol{k}} | u_m \rangle$ defined in terms of the Bloch wave functions for the m-th energy band $|u_m(\boldsymbol{k})\rangle$, where the sum runs over all occupied bands. N remains unchanged as long as there is a finite gap between occupied and unoccupied bands and is a so-called Chern number. Additionally, note that N is an integer (which can be understood in analogy to the quantization of the Dirac magnetic monopole [28]) and therefore also referred to as a $\mathbb{Z}$ invariant.

How this mathematical fact manifests physically has been first understood by Thouless, Kohmoto, Nightingale and den Nijs (TKNN)[29]. They showed the quantized Hall conductivity

$$\sigma_{xy} = Ne^2/h \tag{2.2}$$

to be determined by exactly this topological invariant N (with the Landau levels being interpreted as a band structure). The quantum Hall effect is well known to be caused by gapless edge modes [30] and TKNN thus found a deep connection between the topology of the bulk band structure and the existence of conducting edge states, known as the bulk-boundary correspondence: The topological invariant N, calculated by means of the bulk band structure, is invariably linked to the number of modes present at the edge of the material.

The existence of gapless edge modes in this context can actually be understood in a rather intuitive picture, since the energy gap at the boundary between two topologically distinct regions has to close by definition, allowing for states at low-energies bound to this line. In the case of the quantum Hall effect, this is the edge of the material, i.e. the boundary between the quantum Hall sample and the vacuum.

While a non-zero Chern number can only occur in systems with broken time-reversal symmetry $\mathcal{T}$, spin-orbit interaction (SOI) allows for a different class of topologically nontrivial systems where $\mathcal{T}$ is preserved. We therefore need to include spin into our discussion, which we have neglected to do until now.

To this end, recall Kramers theorem which states for spin-$\frac{1}{2}$ particles that all eigenstates of a $\mathcal{T}$-invariant Hamiltonian are at least two-fold degenerate. Without SOI, this is just the degeneracy between up- and down-states.

Now, consider the edge of a $\mathcal{T}$-invariant two-dimensional insulator with SOI. If there happen to be in-gap states present that are bound to the boundary region, they have to be degenerate at the $\mathcal{T}$-invariant points $k = 0$ and $k = \pi/a$ (where k is the crystal momentum parallel to the edge), see Fig. 2.1a. Away from these points, the spin-orbit interaction lifts the degeneracy. The shape of the edge state dispersion (recall the aforementioned bulk-boundary correspondence) depends on the properties of the bulk and can lead to one of two scenarios:

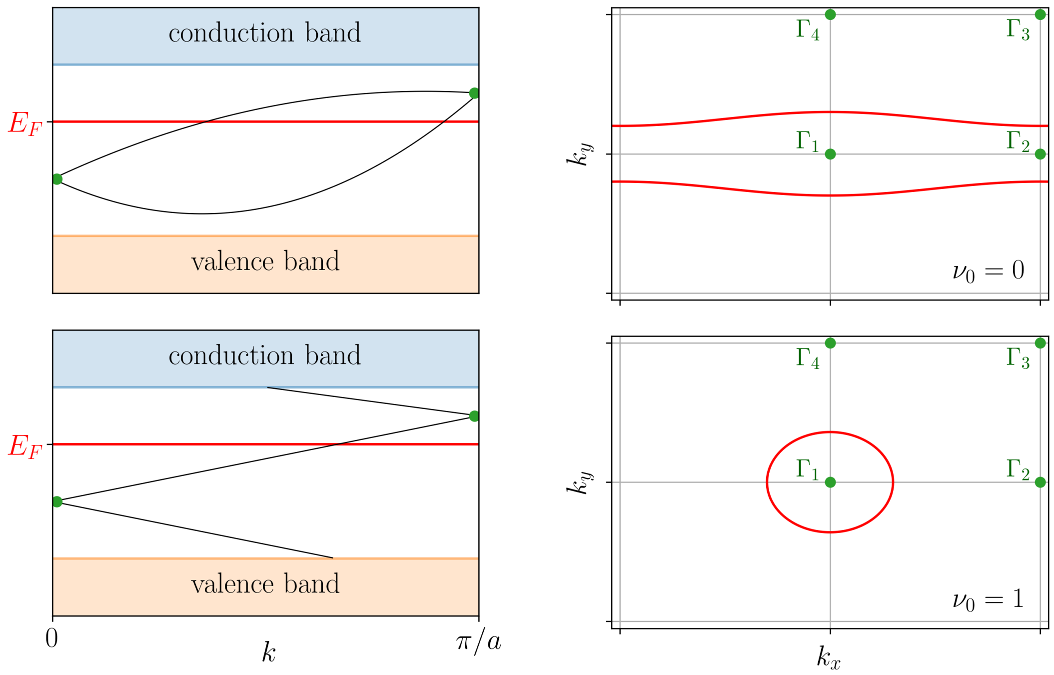

(a) (b)

Figure 2.1: **Sketches of the surface Brillouin zone.** (a) In the two-dimensional case, the dispersion of the surface states (black) either crosses the Fermi energy E_F an even ($\nu = 0$) or an odd ($\nu = 1$) number of times between the two Kramers degenerate points (green) at $k = 0$ and π/a. The orange and blue bands show the bulk valence and conduction bands, respectively. (b) In the three-dimensional case, where the red lines show the surface Fermi arcs, there are four Kramers degenerate Dirac points (green), which are pairwise connected in one of the two ways shown in (a). The example for the $\nu_0 = 0$ case corresponds to an odd number of crossings of the Fermi energy between Γ_1 and Γ_3 as well as between Γ_2 and Γ_4 (and accordingly between Γ_1 and Γ_2 as well as between Γ_1 and Γ_3 in the $\nu_0 = 1$ example).

If the Fermi energy is crossed by the edge states an even number of times between $k = 0$ and $k = \pi/a$, the in-gap states can be removed by continuous deformation of the band structure. In the case of an odd number of crossings, however, this is not possible and these metallic edge states are said to be topologically protected. The parity ν of the number of times the Fermi energy is crossed by the edge modes is thus a topological invariant, called the $\mathbb{Z}_2$ invariant. Their topological nature leads to them being robust against localization through disorder and weak electron interactions. [31] Note that $\mathcal{T}$-symmetry requires for every edge mode with momentum k the existence of a corresponding mode with momentum $-k$ propagating in the opposite direction. A physical realization is given by the quantum spin Hall state. [31–33]

Finally, we turn to the 3D generalization of these concepts and consider the two-dimensional surface of a three-dimensional insulator that exhibits SOI.

Four $\mathcal{T}$-invariant points $\{\Gamma_1, \Gamma_2, \Gamma_3, \Gamma_4\}$ occur in the surface Brillouin zone for which Kramers theorem dictates a degeneracy of the surface states, if they are present. Thus, in this case the surface Brillouin zone exhibits four 2D Dirac points. There are again two ways in which they can connect pairwise, and thus the state is characterized by four $\mathbb{Z}_2$ invariants. They can be chosen such that one of them, called ν_0, corresponds to the number of Dirac points enclosed by the surface Fermi arc.

The surface states for the simplest nontrivial example, given by stacking two-dimensional quantum spin Hall insulators, turn out to not be protected by $\mathcal{T}$ symmetry and can be localized in the presence of disorder. [34] This phase is therefore dubbed weak topological insulator. An example for a corresponding surface Fermi surface is shown in the top plot of Fig. 2.1b. It encloses an even number of Kramers Dirac points, $\nu_0 = 0$.

If instead the case sketched in the bottom of Fig. 2.1b applies, i.e. an odd number of Dirac points being enclosed by the surface Fermi arc, $\nu_0 = 1$, a distinct topological phase is realized, the so-called strong topological insulator. Here, the surface states do enjoy protection by $\mathcal{T}$ symmetry. [34] Consequently, if only one Dirac point is encircled, the surface states can be described by the Hamiltonian

$$H_{\text{Dirac}} = -iv_F \boldsymbol{\nabla} \cdot \boldsymbol{\sigma} - \mu, \tag{2.3}$$

where v_F is the Fermi velocity, μ the chemical potential and $\boldsymbol{\sigma} = (\sigma_x, \sigma_y)$, here and in the following, are Pauli matrices describing the spin.

The first 3D topological insulator was experimentally verified in 2008. [35]

These three-dimensional strong topological insulators form the basis for the structures we aim to explore in this thesis. Before we are ready to do so, however, the second ingredient, superconductivity, and its relation to topological band structures need to be introduced.

2.1.2 Majorana edge modes in spinless superconductors

The energy gap present in superconducting systems allows for an analogous topological classification. It turns out, however, that looking for topologically nontrivial superconducting states directly leads us to the notion of unconventional superconductivity, with pairing symmetries going beyond standard BCS theory.

In the conventional case, Cooper pairing is limited to two electrons of opposite spins, forming a spin-singlet and exhibiting a relative orbital angular momentum of $l = 0$, known as s-wave pairing. One possibility to achieve a pairing with $l \neq 0$, is to instead imagine a spin-polarized system with only one active spin degree of freedom, called a spinless superconductor. The Cooper pairs are then forced to be in a spin-triplet state and the orbital wave function thus needs to be antisymmetric, which makes p-wave pairing possible.

For a two-dimensional model system of such a case, the so-called chiral $p_x + ip_y$ superconductor, Read and Green [8] showed a topological phase transition to exist. Below, we will loosely follow their arguments to derive a corresponding edge mode.

The chiral $p_x + ip_y$ superconductor is described by the Bogoliubov-de Gennes (BdG) Hamiltonian

$$h_{\text{BdG}}(p_x, p_y) = \left(\frac{p_x^2 + p_y^2}{2m^*} - \mu \right) \tau_z - i\Delta(p_x - ip_y)\tau_+ + i\Delta^*(p_x + ip_y)\tau_-, \tag{2.4}$$

where we assume Δ to be constant and approximate the dispersion in the normal phase to be quadratic for small momenta p_x and p_y with effective mass m^* and chemical potential μ. The corresponding Nambu spinor does not have any spin structure $\hat{\Psi}(\boldsymbol{r}) = (\hat{c}(\boldsymbol{r}), \hat{c}^\dagger(\boldsymbol{r}))^T$ (here and in the rest of the thesis, τ_i denote Pauli matrices in Nambu space). From this, the quasiparticle spectrum can be determined to read

$$\varepsilon_\pm(p_x, p_y) = \pm\sqrt{\left(\frac{p_x^2 + p_y^2}{2m^*} - \mu\right)^2 + |\Delta|^2 \left(p_x^2 + p_y^2\right)}. \tag{2.5}$$

It exhibits an energy gap for all $\mu \neq 0$. The gap closing at $\mu = 0$ signalizes a topological transition between the instances with $\mu > 0$, called the (topologically non-trivial) weak-pairing phase, and the (topologically trivial) strong-pairing phase with $\mu < 0$.

Let us examine a boundary at $x = 0$ between the two phases $\mu(x > 0) > 0$ and $\mu(x < 0) < 0$. We are interested in the low-energy physics near the transition point, where μ is small and thus the momenta can be taken to be small as well, such that the BdG Hamiltonian for a definite p_y can be written as

$$h_{\mathrm{BdG}} = -\mu(x)\tau_z - \Delta(\partial_x + p_y)\tau_+ - \Delta^*(-\partial_x + p_y)\tau_-. \tag{2.6}$$

If $p_y = 0$ and $\Delta \in \mathbb{R}$, $h_{\mathrm{BdG}} = -i\Delta\partial_x\tau_y - \mu(x)\tau_z$ is equivalent to the one-dimensional Dirac Hamiltonian with mass profile $\mu(x)$, for which Jackiw and Rebbi [36] showed zero energy solutions to exist if there is an interface with a sign change of the mass. This zero energy state is then bound to this interface. Particularly, here the BdG eigenstate with vanishing energy reads

$$\Phi(x) \propto e^{-\int_0^x dx' \mu(x')/\Delta} \begin{pmatrix} 1 \\ 1 \end{pmatrix}. \tag{2.7}$$

The corresponding quasiparticle operator

$$\hat{\gamma} \propto \int dx\, e^{-\int_0^x dx' \mu(x')/\Delta} (\hat{c}(y) + \hat{c}^\dagger(y)) \tag{2.8}$$

is a special zero mode, which is its own adjoint $\hat{\gamma}^\dagger = \hat{\gamma}$, $\hat{\gamma}^2 = 1$, and therefore dubbed Majorana zero mode (MZM) or Majorana bound state (MBS). For finite p_y, chiral Majorana fermions propagating along the domain wall with the linear dispersion $E = -\Delta p_y$ are obtained

$$\Phi_{p_y}(x, y) \propto e^{ip_y y}\Phi(x), \tag{2.9}$$

analogous to the chiral edge modes in the quantum Hall state.

Note that the Majorana nature of these edge modes does not really come as a surprise, since it results from a generic property of excitations in superconductors described by a BdG Hamiltonian h, as has been pointed out in Ref. [37]. The (anti-unitary) charge conjugation symmetry $\mathcal{C}$, $\mathcal{C}h\mathcal{C}^{-1} = -h$, dictates that for every eigenstate with energy E_n there exists a corresponding negative energy eigenmode with energy $E_{-n} = -E_n$. Combined with the pseudo-reality constraint satisfied by the associated fermionic Nambu spinor $\mathcal{C}\hat{\Psi} = \hat{\Psi}$, it becomes clear that this charge conjugation symmetry is however not a real symmetry, but instead a redundancy in the description: the creation of a particle with positive energy is identical to the annihilation of the associated charge conjugated one with negative energy. The excitations follow to carry no charge and the full quantum field obeys Majorana-like anti-commutation relations.

In a similar way, one can show that discs with for example $\mu < 0$ surrounded by a region with $\mu > 0$ [38] and vortices in superconductors [9] can lead to zero-dimensional MZMs bound to them. Such in-gap modes with zero energy are topologically protected, since pushing them away from their energy would violate particle-hole symmetry, as BdG excitations with finite energy always come in pairs. Only a closing of the gap to other quasiparticle excitations would allow for the removal of a MBS. The number of (unpaired) MZMs is thus a topological invariant.

These zero-energy, zero-dimensional MBSs are furthermore special as they are the only stationary solutions to h with well-defined energy that exhibit the Majorana characteristic of being self-conjugate. It is important to note that as such, these cannot be characterized as a quasiparticle in the usual sense. Indeed, since $\hat{\gamma}^2 = 1$, there is no meaning to the level being occupied or not. Only pairs of MZMs can be combined to result in a fermionic state with well-defined occupation number. This leads (with one pair of MZMs) to a 2-fold degenerate ground state, where the two ground states are distinguished only by fermion parity, since MZMs do not contribute to the Hamiltonian.

These Majorana states making up a pair can still be localized arbitrarily far from each other, which guarantees their topological protection against local perturbations. Additionally, their combined fermionic state can thus encode highly non-local entanglement.

It can be shown as a consequence of these properties, that MZMs on top of that obey non-abelian exchange statistics in two dimensions: not only do they behave as anyons, i.e. neither bosons nor fermions, but as so-called non-abelian anyons, which means that in general two subsequent exchanges do not commute. [9]

Aside from their intrinsic academic appeal, this is the reason for the ubiquitous interest in these Majorana states within condensed matter research, and the resulting interest from our side in systems that may be able to host them: the non-abelian exchange statistics in combination with their topological nature opens avenues towards fault-tolerant and topologically-protected quantum computing (see e.g. Ref. [11] for a review).

2.1.3 Engineering topological superconductivity via the proximity effect

Although p-wave pairing has long been well understood to support Majorana bound states [8, 10], the question regarding materials realizing these exotic pairing symmetries is a different and difficult one, as the quest for an intrinsic topological superconductor is to this day an ongoing and hotly debated topic (see Ref. [39] and references therein).

It was therefore a major breakthrough, when in 2008 Fu and Kane [13] showed that an effective two-dimensional $p_x + ip_y$ superconductor can be engineered without the need of such a material, by instead combining an ordinary s-wave superconductor with a three-dimensional strong topological insulator (TI). The structures we are going to explore in this thesis are all based on this crucial insight, which in the following years has furthermore inspired many more proposals taking advantage of the superconducting proximity effect in a similar vein. [14]

To review their ideas, consider the surface of a 3D strong TI on which an s-wave superconductor is deposited. Due to the proximity effect [40], a superconducting gap $\Delta = \Delta_0 e^{i\varphi}$ is induced in the surface states. In the simplest case of only one Dirac point being encircled by the surface Fermi arc, the Hamiltonian describing this setup is thus given by $\hat{H} = \frac{1}{2}\int d\boldsymbol{r}\, \hat{\Psi}^\dagger h \hat{\Psi}$, where the Nambu spinor containing the electronic field operators is $\hat{\Psi} = (\hat{\psi}_\uparrow, \hat{\psi}_\downarrow, \hat{\psi}_\downarrow^\dagger, -\hat{\psi}_\uparrow^\dagger)^T$ and the BdG Hamiltonian reads

$$h = -iv_\mathrm{F}\tau_z \boldsymbol{\sigma}\cdot\boldsymbol{\nabla} - \mu\tau_z + \Delta_0(\cos\varphi\,\tau_x + \sin\varphi\,\tau_y). \tag{2.10}$$

Fu and Kane's intuition for why this has the potential to resemble the desired spinless p-wave superconductors stems from the fact that the TI surface states essentially comprise half of an ordinary metal: due to the spin-momentum locking, there is no spin degeneracy present at the Fermi surface.

Making this explicit by projecting onto the helical basis

$$\hat{c}_{\boldsymbol{k}} = \frac{1}{\sqrt{2}}\left(\hat{\psi}_{\boldsymbol{k},\uparrow} + e^{i\theta_{\boldsymbol{k}}}\hat{\psi}_{\boldsymbol{k},\downarrow}\right) \tag{2.11}$$

with $v_\mathrm{F}k_0 \simeq \mu$ and $\boldsymbol{k} = k_0(\cos\theta_{\boldsymbol{k}}, \sin\theta_{\boldsymbol{k}})^T$, one finds

$$\hat{H} = \int \frac{d\boldsymbol{k}}{(2\pi)^2}\left[(v_\mathrm{F}|\boldsymbol{k}| - \mu)\hat{c}_{\boldsymbol{k}}^\dagger \hat{c}_{\boldsymbol{k}} + \frac{1}{2}\left(\frac{\Delta}{|\boldsymbol{k}|}(k_x + ik_y)\hat{c}_{\boldsymbol{k}}^\dagger \hat{c}_{-\boldsymbol{k}}^\dagger + \text{h.c.}\right)\right], \tag{2.12}$$

which is indeed formally equivalent to the pairing in (2.4). However, it is important to note that there are a few key differences.

First, the spectrum of (2.10), in contrast to the $p_x + ip_y$ superconductor, is fully gapped for all values of μ. Furthermore, via a gauge transformation which rotates the phase to zero (assuming it is constant in space), (2.10) can be made time-reversal symmetric with the anti-unitary time-reversal operator $\mathcal{T} = i\sigma_y\mathcal{K}$ (where $\mathcal{K}$ denotes complex conjugation). The same does not hold for (2.4), which breaks this symmetry. Finally, since the examined two-dimensional surface is itself the boundary of a three-dimensional TI, it cannot have a boundary of its own. Thus, in order to obtain edge states, an additional part of the TI surface needs to be gapped out. One possibility is the breaking of time-reversal symmetry by depositing a ferromagnetic insulator next to the superconductor [41]. Another option is to open a second superconducting gap. The latter directly leads to the notion of Josephson junctions formed on the surface of a topological insulator, also considered in Ref. [13] and reviewed in the following.

2.2 Topological insulator Josephson junctions

2.2.1 Non-chiral Majorana wire

The geometry depicted in Fig. 2.2, with two superconductors deposited on a 3D strong TI surface forming a Josephson junction, is described by the BdG Hamiltonian

$$h = -iv_\mathrm{F}\tau_z \boldsymbol{\sigma}\cdot\boldsymbol{\nabla} - \mu\tau_z + \Delta_0(x)(\cos\varphi(x)\,\tau_x + \sin\varphi(x)\,\tau_y), \tag{2.13}$$

where $\Delta_0(x) = \Delta_0\,\theta(|x| - W/2)$ and the phase difference is $\varphi(x) = \varphi\,\theta(x)$. W is the width of the junction.

There may exist Andreev bound states (ABS) in this structure that are confined to the region between the two superconductors due to the energy gaps on either side of the junction. Since the system is translation invariant in y-direction, we can analyze it for a fixed momentum

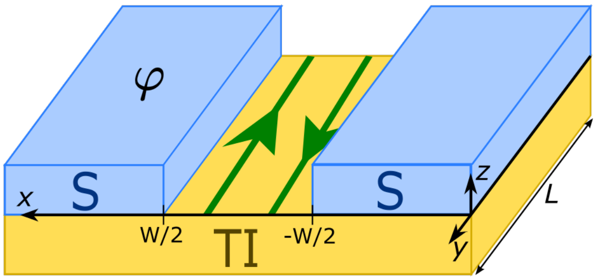

Figure 2.2: **Sketch of the S-TI-S junction** of width W and length L with a phase difference φ between the superconductors. The green arrows represent the one-dimensional Majorana modes counter-propagating along the junction.

$-i\partial_y \to q$. In the limit $W, \mu \to 0$, Fu and Kane [13] found only two branches of bound states to be present in the gap with a simple relativistic dispersion given by

$$\varepsilon_\pm(q) = \pm\sqrt{v_\mathrm{F}^2 q^2 + \Delta_0^2 \cos^2(\varphi/2)}. \tag{2.14}$$

Consequently, the spectrum is gapless for $\varphi = \pi$ and a low-energy effective theory incorporating finite W and μ can be deduced for $\epsilon = \pi - \varphi \sim 0$ and $q \sim 0$. To this end, one first solves the 'transverse' Hamiltonian for zero modes

$$h|_{q=\epsilon=0}\zeta_{1,2}(x) = 0, \quad \zeta(|x| \to \infty) = 0, \tag{2.15}$$

which can conveniently be chosen to be particle-hole symmetric $\mathcal{C}\zeta_{1,2} = \zeta_{1,2}$ with $\mathcal{C} = \tau_y\sigma_y\mathcal{K}$. The solutions read

$$\zeta_\pm(x) \equiv \zeta_1(x) \pm i\zeta_2(x) \propto \begin{pmatrix} 1 \\ \pm i \\ \pm i \\ -1 \end{pmatrix} e^{\pm i\mu x/v_\mathrm{F} - \int_0^x dx'\,\Delta_0(x')/v_\mathrm{F}}. \tag{2.16}$$

Now, projecting the Hamiltonian onto this basis by evaluating $\langle\zeta_a|q\tau_z\sigma_y|\zeta_b\rangle$ and $\langle\zeta_a|\epsilon\theta(x - W/2)\tau_y|\zeta_b\rangle$, the effective Hamiltonian

$$h_\mathrm{eff} = -iv\rho_x\partial_y + \frac{\epsilon}{2}\Delta_0\rho_y \tag{2.17}$$

is obtained, corresponding to a one-dimensional massive Dirac Hamiltonian with effective velocity v, where ρ_i are Pauli matrices acting on (ζ_1, ζ_2). The associated second-quantized Hamiltonian follows from defining the quasiparticle operators

$$\hat{\chi}_q^{R/L} := \int d\boldsymbol{r}\, (\xi_q^{R/L}(\boldsymbol{r}))^\dagger \hat{\Psi}(\boldsymbol{r}), \qquad \hat{\chi}_{R/L}(y) = \int \frac{dq}{2\pi} \hat{\chi}_q^{R/L} e^{iqy} \tag{2.18}$$

with $\xi_q^{R/L} = \frac{1}{\sqrt{2}}(\zeta_1 \pm \zeta_2)e^{iqy}$ to be given by

$$\hat{H}_\mathrm{eff} = \int dy \left[-\frac{iv}{2}(\hat{\chi}_R\partial_y\hat{\chi}_R - \hat{\chi}_L\partial_y\hat{\chi}_L) + i\epsilon\Delta_0\hat{\chi}_R\hat{\chi}_L\right]. \tag{2.19}$$

$\hat{\chi}_{R,L}(y)$ are real Majorana fields and thus a description of the low-energy physics of the junction in terms of one-dimensional counter-propagating Majorana modes has been achieved. The topological insulator Josephson junction can be understood as a non-chiral Majorana wire.

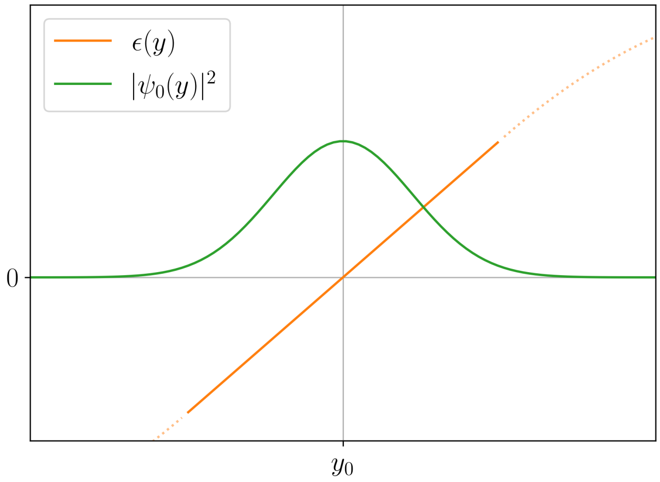

Figure 2.3: **Schematic depiction of a Majorana bound state** (probability density shown in green) localized at a zero crossing at $y = y_0$ of the mass term $\epsilon(y)$ (orange).

2.2.2 Zero-dimensional Majorana and Andreev bound states

The counter-propagating Majorana modes hybridize and thus open a Majorana mass gap if $\varphi \neq \pi$. Now, suppose the phase difference to be y-dependent, $\varphi = \varphi(y)$. If this spatial variation of the mass term is sufficiently slow, such that the semiclassical labeling in terms of the momentum q still applies, we may simply replace $\epsilon \to \epsilon(y)$ in (2.17). Points where ϵ changes sign correspond to Josephson vortices [42], which ensue the existence of zero-dimensional bound states in their center.

Particularly, a topologically protected zero-energy solution, i.e. a Majorana bound state, is guaranteed which, assuming $\epsilon(y)$ has a positive slope at its zero crossing, is given by (see Fig. 2.3)

$$\psi_0(y) \propto \begin{pmatrix} 0 \\ 1 \end{pmatrix} e^{-\frac{\Delta_0}{2v} \int_0^y dy' \, \epsilon(y')}. \tag{2.20}$$

Depending on the details, a number of additional localized Andreev bound states with finite energies may be present as well. [43, 44] We can understand this by linearizing the mass term in the vicinity of such a zero-crossing $\frac{\Delta_0}{2}\varepsilon(y) \simeq \alpha(y - y_0)$ and introducing the harmonic oscillator creation and annihilation operators via

$$y - y_0 := \sqrt{\frac{v}{2\alpha}}(a^\dagger + a), \quad -i\partial_y := i\sqrt{\frac{\alpha}{2v}}(a^\dagger - a). \tag{2.21}$$

It follows

$$h_{\text{eff}} = i\omega(a^\dagger \rho_- - a\rho_+), \tag{2.22}$$

where $\omega = \sqrt{2\alpha v}$ and $\rho_\pm = \frac{1}{2}(\rho_x \pm i\rho_y)$. Thus, with the usual harmonic oscillator eigenstates denoted $|n\rangle$, where $n = 0, 1, 2, \ldots$, one obtains a discrete spectrum of states $|\psi_n\rangle$ localized at

$y = y_0$ with energies $E_n = -E_{-n} = \omega\sqrt{n}$ given by

$$\begin{aligned} |\psi_0\rangle &= |0\rangle\,|{\downarrow}\rangle\,, \\ |\psi_{n>1}\rangle &= \frac{1}{\sqrt{2}}(|n-1\rangle\,|{\uparrow}\rangle + i\,|n\rangle\,|{\downarrow}\rangle), \\ |\psi_{-n<-1}\rangle &= \frac{1}{\sqrt{2}}(|n-1\rangle\,|{\uparrow}\rangle - i\,|n\rangle\,|{\downarrow}\rangle), \end{aligned} \tag{2.23}$$

where $\rho_z\,|{\updownarrows}\rangle = \pm\,|{\updownarrows}\rangle$.

Such a dependence of the phase difference on the location in the junction can be achieved by means of an external magnetic field. [42] Naturally, topological insulator Josephson junctions threaded by a magnetic flux have been proposed as platforms for creating and manipulating MBSs with regards to possible quantum computing applications. [45]

In Chapter 5 we therefore take a deeper look at these structures and identify the limitations of the here derived effective theory (and its generalizations). Before that, in Chapters 3 and 4, we extend the model by allowing the quantity which couples the Majorana modes to be an independent and dynamic degree of freedom, and examine the possible quantum phase transitions this entails. Of course, the above arguments hold regardless of the specific physical nature of the mass term and we are going to, for example, find magnetic domain walls which carry localized Majorana and Andreev bound states in analogy.

3

Chapter 3

Peierls instabilities in topological Josephson junctions

In the preceding chapter, we introduced the idea that two-dimensional topological Josephson junctions can be engineered by depositing bulk s-wave superconductors on the surface of a three-dimensional topological insulator, as originally envisioned by Fu and Kane [13]. The one-dimensional Majorana modes in such structures then become hybridized through the phase difference between the superconductors. As we will come to see in this chapter, the magnetization of an embedded ferromagnet can play an analogous role. Our goal is to analyze the interplay of the dynamics of these bosonic modes (the magnetization and the phase) with the Majorana fermions in the junction, in order to better understand the possibilities of controlling and manipulating Majorana bound states. To this end, we also take into consideration a different class of topological superconductivity, which hosts edge modes without the breaking of time-reversal symmetry. We find, as a generic feature of the type of coupling considered, the system to exhibit a Peierls-like instability towards the formation of a Majorana mass gap, stabilized by the parameters which govern the rigidity of the bosonic modes' dynamics. We finally examine the Majorana zero modes carried by solitonic excitations in these systems.

Section 3.1 of this chapter is based on Ref. [46], while Section 3.2 is based on parts of Ref. [47]. Large passages are taken verbatim or are adapted very closely from these publications.

3.1 SMS junction on the surface of a topological insulator

The embedding of a ferromagnetic insulator in the previously introduced topological insulator Josephson junctions has been in the past explored with the idea to manipulate Majorana zero modes and other physical properties of the system, like the supercurrent across the junction [22–25]. Within this avenue, not much attention has been given to the fact that the magnetization in a ferromagnet is not perfectly rigid but exhibits dynamics which can be described by the Landau-Lifshitz-Gilbert (LLG) equation [48–50]. Especially in view of the strong spin-orbit coupling in the topological surface states, the back-action of the electronic modes on the magnetization can be expected to yield a significant torque, which needs to be taken into account since it can lead to precession and reorientation of the magnetization direction. For non-topological systems, Josephson current-induced magnetization dynamics

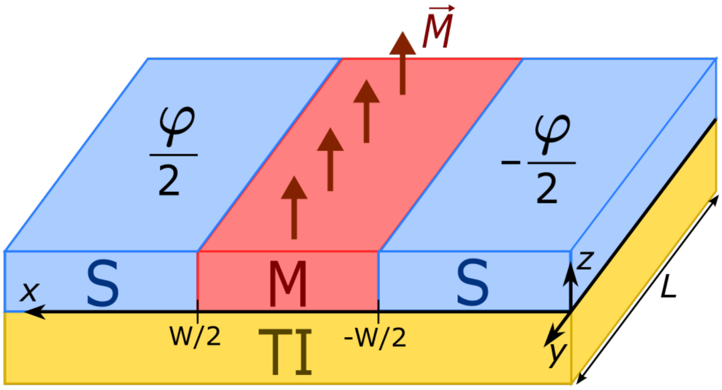

Figure 3.1: **Considered geometry of a superconductor-ferromagnet-superconductor (SMS) junction** of width W and length L on the surface of a 3D strong topological insulator (TI) with a phase difference φ between the superconductors. The magnetization $\vec{M}$ is y- and time-dependent.

has for example been discussed in Refs. [51–55]. In Ref. [56], this effect has been touched upon for topological Josephson junctions by incorporating an additional effective field in the LLG equation in the voltage driven regime, allowing for control of the magnetization direction by the Josephson current. In our work, we instead consider the zero-bias case and derive an effective low-energy theory for the superconductor-ferromagnet-superconductor (SMS) junction on the surface of a 3D TI, which describes the coupling between the magnons and the one-dimensional Majorana modes counter-propagating along the junction. Note that this section is dedicated to the limit of a strong magnetic easy-axis anisotropy, before we generalize to arbitrary anisotropies in Chapter 4.

In our analysis of this model, we are going to see that in the mean-field approximation the Peierls instability [57] occurs, leading to a splitting and tilting of the easy-axis and consequently an opening of a Majorana mass gap. Next, we will examine the corresponding quantum phase diagram by means of a fluctuation analysis, laying the basis towards the full quantum phase diagram of the model which will be further discussed in Chapter 4. Finally, experimental signatures of the symmetry breaking and solitonic excitations will be explored.

3.1.1 Low-energy effective theory for strong easy-axis anisotropy

The system we are interested in is schematically depicted in Fig. 3.1. The s-wave superconductors introduce superconducting gaps in the TI surface regions they cover due to the proximity effect, effectively forming a Josephson junction of two-dimensional topological superconductors (see Chapter 2). We assume the superconducting gaps to be of the same magnitude Δ_0 on both sides of the junction, but differing by a relative phase φ. The ferromagnetic insulator causes an effective exchange field $\vec{h}_{\text{eff}}$ in the underlying surface of the TI which couples to the electrons' spin and is proportional to the ferromagnet's magnetization $\vec{h}_{\text{eff}}(\boldsymbol{r}) = \alpha\vec{M}(\boldsymbol{r})$ with a proportionality constant α. Here and in the following, 3D vectors are denoted by an arrow above the symbol, while 2D vectors are written in bold.

The BdG Hamiltonian describing this setup is thus given by

$$h = -iv_{\text{F}}\tau_z\boldsymbol{\sigma}\cdot\boldsymbol{\nabla} - \mu\tau_z + \alpha\vec{M}(\boldsymbol{r})\cdot\vec{\sigma} + \Delta_0(y)(\cos\varphi(\boldsymbol{r})\tau_x + \sin\varphi(\boldsymbol{r})\tau_y)\ . \tag{3.1}$$

As described above

$$\begin{aligned}\Delta_0(x) = \Delta_0\,\Theta(|x| - W/2), \quad \varphi(\boldsymbol{r}) = \varphi(y)/2\,[\Theta(x - W/2) - \Theta(-(x + W/2))],\\ \vec{M}(\boldsymbol{r}) = M_\mathrm{S}\,\vec{m}(\boldsymbol{r})\Theta(W/2 - |x|)\end{aligned} \tag{3.2}$$

with v_F being the Fermi velocity and μ the chemical potential, which we for now assume to be constant everywhere (in Chapter 5 we are going to allow for a renormalization of the chemical potential due to proximity to the metallic superconductors.) The saturation magnetization is denoted by M_S and $|\vec{m}| = 1$.

The quasiparticle dispersion for the case of a ferromagnet with spatially homogeneous magnetization in z-direction $\vec{m}(\boldsymbol{r}) = \vec{e}_z$ deposited on a 3D TI reads $\varepsilon_{\text{TI-M}}(\boldsymbol{k}) = \sqrt{v_\mathrm{F}^2\boldsymbol{k}^2 + \alpha^2 M_\mathrm{S}^2} \pm \mu$, which is gapped when $\alpha M_\mathrm{S} \equiv M > \mu$, i.e. when the Fermi level lies within the mass gap of the Dirac spectrum induced by the exchange field. As shown in Ref. [41], a chiral 1D Majorana mode emerges at the interface between the regions with superconducting and magnetic gaps. For the geometry of Fig. 3.1, this results in two counter-propagating chiral Majorana modes near each interface. They hybridize with an amplitude $\propto \cos(\varphi/2)$ and, thus, decouple at $\varphi = \pi$. The hybridization in this case decreases exponentially with the width W of the junction.

If it instead holds $M < \mu$, no gap is induced for $|x| < W/2$ and, for a phase difference of $\varphi = \pi$, the junction becomes a non-chiral Majorana wire with two counter-propagating Majorana modes spread across its whole width (similar to the situation described in Ref. [13]). A deviation of the phase difference from a value of π, $\epsilon = \pi - \varphi$ hybridizes the two Majorana modes as in the above case, opening up a Majorana mass gap, which here however does not exponentially decrease with W.

Allowing the magnetization direction to deviate from the z-axis, we find that the m_x-component plays the same role as ϵ in hybridizing the two Majorana modes with some coupling constant g. In Appendix A.1, the corresponding low-energy effective Hamiltonian is derived. Since we are interested in the interplay between Majorana modes and the magnetization, we fix from now on $\epsilon = 0$. In Section 3.1.4 we will also consider deviations from $\varphi = \pi$ and examine the current-phase relation.

For the magnetization dynamics we employ a micromagnetic description [58]. For now, we introduce a large easy-axis anisotropy B in z-direction, such that the x- and y-components of the magnetization can reasonably assumed to be small $\vec{m} = \left(m_x, m_y, 1 - (m_x^2 + m_y^2)/2\right)^T$. We are going to lift this restriction and consider weak easy-axis anisotropies as well as an easy-plane anisotropy in Chapter 4. Furthermore, we take the junction's width to be small compared to the magnetic coherence length in order for the magnetization direction to only depend on the y-coordinate. The magnetic energy shall also include an exchange coupling A, such that the corresponding (real-time) Lagrangian reads

$$\mathcal{L} = \frac{M_\mathrm{S}}{2\gamma}(\dot{m}_x m_y - m_x \dot{m}_y) - \frac{1}{2}A\left((\partial_y m_x)^2 + (\partial_y m_y)^2\right) - \frac{1}{2}B\left(m_x^2 + m_y^2\right). \tag{3.3}$$

The associated equation of motion is the dissipationless LLG equation with gyromagnetic ratio γ. Note that, due to the restriction of $\vec{m}$ to the unit sphere, there is only one independent degree of freedom in the dynamics of the magnetization, leading to the equal-time commutator of the free quantized bosonic fields m_x and m_y being non-zero $[m_\alpha(x), m_\beta(x')] = i\frac{\gamma}{M_\mathrm{S}}\varepsilon_{\alpha\beta}\delta(x-x')$. [59]

In the absence of coupling to the fermions, the dispersion of the magnonic excitations is given by $\omega_q = \frac{\gamma}{M_\mathrm{S}}(Aq^2 + B)$.

Altogether, the effective Euclidean action reads

$$S = \frac{1}{2}\int d\tau\, dy \left[\bar{\chi}(v\partial\!\!\!/ + g m_x)\chi + \begin{pmatrix} m_x \\ m_y \end{pmatrix}^T \begin{pmatrix} -A\partial_y^2 + B & i\frac{M_\mathrm{S}}{\gamma}\partial_\tau \\ -i\frac{M_\mathrm{S}}{\gamma}\partial_\tau & -A\partial_y^2 + B \end{pmatrix} \begin{pmatrix} m_x \\ m_y \end{pmatrix}\right], \tag{3.4}$$

with the two-component Majorana spinor $\chi = (\chi_\mathrm{R}, \chi_\mathrm{L})^T$, $\bar{\chi} = \chi^T\gamma_0$, the Dirac (Pauli) matrices $\gamma_0 = \tilde{\sigma}_y$ and $\gamma_1 = \tilde{\sigma}_x$, as well as $\partial\!\!\!/ = \frac{1}{v}\gamma_0\partial_\tau + \gamma_1\partial_y$. v is the effective velocity of the Majorana modes (see Appendix A.1).

At $g = 0$ the action of the magnetization dynamics corresponds to a charged scalar with $U(1)$ symmetry. This $U(1)$ invariance reflects the spin rotation invariance in the x-y-plane in spin space and prevents spontaneous symmetry breaking. However, the coupling to the fermions, which are governed by spin-orbit interaction, breaks this symmetry down to $\mathbb{Z}_2$, where $\pm m_x$ describe degenerate configurations. Hence, the coupling to fermions may give rise to spontaneous symmetry breaking in the ground state.

Note that although this action has been motivated by a specific system, our considerations below are generalizable to other instances of one-dimensional fermionic modes coupled to a bosonic field, as we will see in a subsequent section.

3.1.2 Mean-field instability of the effective bosonic action

The action (3.4) is quadratic both in χ and in $(m_x, m_y)^T$. Since, in contrast to the free Majoranas, the spectrum of the magnetic degrees of freedom is gapped, in order to proceed it seems most natural to integrate out the bosons. The magnetic part of the action is diagonalized by introducing the complex scalar field ϕ with $m_x = \sqrt{\frac{\gamma}{2M_\mathrm{S}}}(\phi+\phi^*)$ and $m_y = -i\sqrt{\frac{\gamma}{2M_\mathrm{S}}}(\phi-\phi^*)$. One then straightforwardly obtains the effective four-fermion interaction

$$S_\mathrm{eff}^\mathrm{int} = -\frac{g^2}{2}\int dY dY'\, \chi_\mathrm{L}(Y)\chi_\mathrm{R}(Y)\mathcal{G}_\mathrm{m}(Y,Y')\chi_\mathrm{R}(Y')\chi_\mathrm{L}(Y') \tag{3.5}$$

where $Y = (y, \tau)$ and $\mathcal{G}_\mathrm{m}^{-1} = \frac{M_\mathrm{S}}{\gamma}\partial_\tau - A\partial_y^2 + B$. This interaction is non-local in both space and time with correlation lengths $\xi_{y,\mathrm{f}} \sim \sqrt{A/B}$ and $\xi_{\tau,\mathrm{f}} \sim M_\mathrm{S}/\gamma B$ respectively. For fixed B, the correlation length in space is thus governed by the exchange coupling or 'stiffness' of the magnetization, while the correlation length in time is proportional to the inverse of the magnonic excitation gap $1/\omega_{q=0}$. If the corresponding correlation lengths are sufficiently small, a gradient expansion of $\mathcal{G}_\mathrm{m}$ in (3.5) is justified. There, it has to be noted that the zeroth order term, involving no derivatives of the four Majorana fields taken at the same point in space and time, vanishes due to Fermi statistics. The lowest order non-vanishing contributions to the interaction are therefore of the form $\chi_\mathrm{R}(\partial_{Y_i}\chi_\mathrm{R})\chi_\mathrm{L}(\partial_{Y_j}\chi_\mathrm{L})$ $(i, j = 1, 2)$ and can be seen to be highly irrelevant by power counting, leaving the Majorana modes gapless and the magnetic degrees of freedom in a disordered phase. It is thus clear that in a parameter regime, where A and M_S/γ are small enough for a gradient expansion to be applicable, the interaction has no qualitative effects on the system. Symmetry breaking is a strong-coupling phenomenon, at least for any finite range interaction. In order to see whether increasing the values of A and/or M_S/γ leads to a cross-over to a non-trivial phase, it turns out to be advantageous to work in the bosonic picture instead.

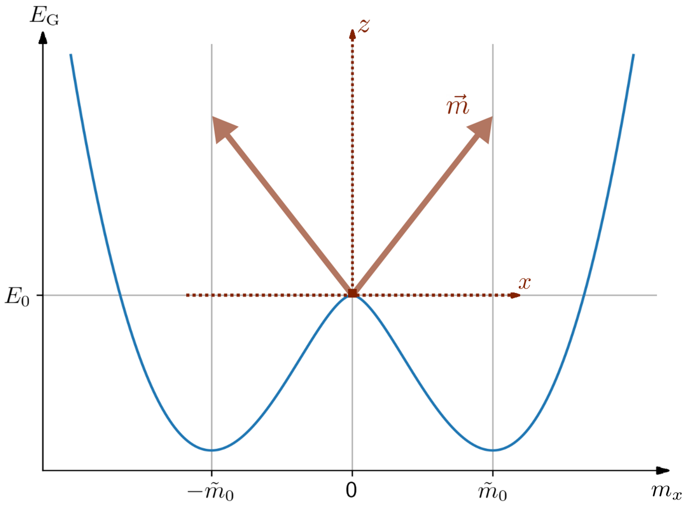

Figure 3.2: **The double well potential** arising for m_x in mean-field theory is shown in blue. The red arrows represent the two corresponding symmetry-broken ground state configurations of the magnetic field, tilted away from the z-axis with m_x acquiring a finite vacuum expectation value $\langle m_x \rangle = \pm\tilde{m}_0$.

Let us assume for the moment that the system breaks the $\mathbb{Z}_2$-symmetry. Then fermions are gapped and can be integrated out. Integrating out the fermionic degrees of freedom in (3.4) leaves us with the effective bosonic action

$$S_{\text{eff}} = S_{\text{m}} - \frac{1}{2}\text{tr}\log\mathcal{G}^{-1}, \tag{3.6}$$

where

$$\mathcal{G}^{-1} = \begin{pmatrix} \partial_\tau - iv\partial_y & igm_x \\ -igm_x & \partial_\tau + iv\partial_y \end{pmatrix} \tag{3.7}$$

and S_{m} is the purely magnetic part of (3.4). We assume for the moment that it is permissible to perform a mean field analysis. Below we will analyze fluctuations that go beyond the mean-field approach and discuss the stability of the assumption of long-range order.

For constant $m_x(y,\tau) = \tilde{m}_0$ and within the mean field theory, this action has a saddle point $\delta S/\delta m_x = 0$ at $\pm\tilde{m}_0 \neq 0$ satisfying the BCS-like gap equation

$$\frac{B}{g^2} = \int_0^\Lambda \frac{dk}{2\pi}\,\frac{\tanh(\sqrt{v^2k^2 + g^2\tilde{m}_0^2}/2T)}{\sqrt{v^2k^2 + g^2\tilde{m}_0^2}}, \tag{3.8}$$

where we took the limit $L \to \infty$ and introduced a UV momentum cut-off Λ.

Thus, at low temperatures,

$$g\tilde{m}_0 \equiv \tilde{\Delta} = 2v\Lambda e^{-2\pi vB/g^2} \tag{3.9}$$

and the corresponding ground state energy in terms of m_x exhibits the characteristic double-well shape $E_G/L = \frac{1}{2}[B + \frac{g^2}{2\pi v}(\log|\frac{gm_x}{2v\Lambda}| - \frac{1}{2})]m_x^2 + E_0/L$ (see Fig. 3.2), where E_0 is the contribution from $m_x = 0$. This spontaneous symmetry breaking at the mean-field level, signifying an instability of the easy axis with m_x acquiring a finite ground state expectation value, can be understood as follows: a positive energy cost, $\propto Bm_x^2$, of the magnetization deviating from the easy-axis direction is balanced by the energy gain, $\propto \frac{g^2}{2\pi v}(\log|\frac{gm_x}{2v\Lambda}| - \frac{1}{2})\, m_x^2$, emerging due to the opening of the fermionic gap. It is the Majorana fermion analog to the Peierls instability of the one-dimensional Fröhlich model [57, 60] in the commensurate regime, where the order parameter is real. A real order parameter furthermore means that the broken symmetry is discrete, such that the Mermin-Wagner theorem does not apply. Nevertheless, even if the mean-field solution turns out to be stable, with the system being one-dimensional any emerging long range order has to be expected to be prohibited by the formation of domain walls at $T > 0$ in the thermodynamic limit of large L. This is due to the fact that the energetic cost of creating domain walls, with m_x switching sign along the junction and interpolating between the two minima, is in 1D always outweighed by the ensuing gain in entropy, as is well-known from the Ising model and Peierls' argument [61, 62]. However, drawing the analogy between the Ising model and our system further, at any finite size L the coherence length ξ_m, given by the average distance between two domain walls, can be expected to be exponentially large at low temperatures $\xi_m \sim b\, e^{E_{\mathrm{DW}}/T}$, where b is the characteristic width of a domain wall and E_{DW} its energy, suggesting significantly large stretches of an ordered magnetic phase with hybridization between χ_{R} and χ_{L} to be realized. This is in contrast to the results we obtained in the gradient expansion of the fermionic picture above.

From this, one can suspect the existence of a cross-over or a phase transition from a phase with small A and M_{S}/γ, where the fermionic gradient expansion is valid and any mean-field considerations in the bosonic picture are rendered unusable due to large fluctuations, to a phase with large A or large M_{S}/γ, where the fluctuations are suppressed and the mean-field solution is stabilized such that domain walls are a meaningful concept with the interaction in the fermionic picture being very long-ranged.

Qualitative arguments for analogous mechanisms have already been given in earlier publications. In Refs. [63] and [64] devoted to the Peierls instability, the validity of mean-field theory is assumed based on slow response times of the phononic modes. In Ref. [65], the authors expect a large temporal stiffness of the bosons mediating the interaction in a Tomonaga-Luttinger liquid to stabilize the symmetry-broken phase (they call this regime "adiabatic limit"). In the following, we aim to verify and quantify these qualitative considerations on the level of a Gaussian approximation for the fluctuations around the mean-field solution.

3.1.3 Fluctuation analysis and phase diagram

We examine the conjectured transition when varying A and M_{S}/γ by analyzing the way in which Gaussian fluctuations around a mean-field solution at zero temperature affect the gap equation, as was done for the BCS theory in Refs. [66] and [67].

Our reasoning is motivated by the following logic: Since symmetry breaking in the Ising universality class is allowed in principle at $T = 0$, we assume a finite value of the order parameter. Then, we study Gaussian fluctuations. If they are small, the assumption of order is justified and consistent. If fluctuations are large, they likely destroy long-range order and the above mean-field approach is not justified. While formally this is an uncontrolled approximation to a strong-coupling problem, it gives insights into the parameter regime where Ising order is allowed and provides the order of magnitude of the microscopic parameters where this order prevails.

To this end, we expand the action (3.6) around some assumed minimum $m_x = m_0$, which is not necessarily the mean-field minimum $\tilde{m}_0$ from above, up to second order in the fluctuations $(\delta m_x, \delta m_y)$ around it, $m_x(x,\tau) = m_0 + \delta m_x(x,\tau)$ and $m_y(x,\tau) = \delta m_y(x,\tau)$, to find

$$S_{\text{eff}} = \frac{1}{2}\frac{T}{L}\sum_{q,\omega_m}\begin{pmatrix}\delta m_x\\ \delta m_y\end{pmatrix}^T \mathcal{D}^{-1}_{q,\omega_m}\begin{pmatrix}\delta m_x\\ \delta m_y\end{pmatrix} + \frac{1}{2}\frac{L}{T}Bm_0^2 - \frac{1}{2}\operatorname{tr}\log\mathcal{G}_0^{-1}, \tag{3.10}$$

where

$$\mathcal{D}^{-1}_{q,\omega_m} = \begin{pmatrix} Aq^2 + B + \Pi(q,\omega_m) & \frac{M_\text{S}}{\gamma}\omega_m \\ -\frac{M_\text{S}}{\gamma}\omega_m & Aq^2 + B \end{pmatrix}, \tag{3.11}$$

and

$$\mathcal{G}_0^{-1} = \mathcal{G}^{-1}\big|_{m_x(x,\tau)=m_0}. \tag{3.12}$$

Further

$$\Pi(q,\omega_m) = \frac{g^2}{2}\frac{T}{L}\sum_{k,\varepsilon_n}\operatorname{tr}_{2\times 2}\Big[\mathcal{G}_0(k,\varepsilon_n)\tilde{\sigma}_y\mathcal{G}_0(k+q,\varepsilon_n+\omega_m)\tilde{\sigma}_y\Big] \tag{3.13}$$

with ω_m and ε_n being the bosonic and fermionic Matsubara frequencies respectively. The linear terms in δm_x only contain $\delta m_x(q=0,\omega_m=0)$-contributions and can therefore safely be omitted when determining m_0.

From the partition function $Z = \int \mathcal{D}(\delta m_x, \delta m_y)\, e^{-S_{\text{eff}}}$ one obtains the ground state energy

$$\frac{E_\text{G}}{L} = \frac{1}{2}\left[B + \frac{g^2}{2\pi v}\left(\log\frac{gm_0}{2v\Lambda} - \frac{1}{2}\right)\right]m_0^2 + \frac{1}{2}\frac{T}{L}\sum_{q,\omega_m}\log\det\nolimits_{2\times 2}\left(\mathcal{D}^{-1}_{q,\omega_m}\right)\Bigg|_{T\to 0} + \frac{E_0}{L}, \tag{3.14}$$

and the corresponding gap equation reads

$$\frac{2}{L}\frac{dE_\text{G}}{d(\Delta^2)} = \frac{1}{2\pi v}\log\frac{\Delta}{\tilde{\Delta}} + X = 0, \tag{3.15}$$

where $\Delta \equiv gm_0$ and X denotes the contribution due to the fluctuations

$$X = \int\frac{dq\,d\omega}{(2\pi)^2}\frac{\frac{d}{d(\Delta^2)}\det_{2\times 2}\mathcal{D}^{-1}_{q,\omega}}{\det_{2\times 2}\mathcal{D}^{-1}_{q,\omega}}\Bigg|_{T\to 0}. \tag{3.16}$$

Obviously, without fluctuations, the mean-field solution $\Delta = \tilde{\Delta}$ is recovered. In order to take the fluctuations into account, Eq. (3.16) and, thus, $\Pi(q,\omega)$ need to be evaluated. Following Ref. [68], in Appendix A.2 we show that

$$\Pi(q,\omega) = \frac{g^2}{2\pi v}\left[\log\frac{\Delta}{2v\Lambda} + \frac{\sqrt{1+r^2}}{r}\operatorname{Arsinh}(r)\right], \tag{3.17}$$

with $r = \sqrt{v^2q^2+\omega^2}/2\Delta$ being the radial coordinate in the $\left(\frac{vq}{2\Delta}, \frac{\omega}{2\Delta}\right)$-plane. It follows

$$X = \frac{1}{2\pi v}\frac{4}{\pi}\int_0^\infty dr\int_0^{\pi/2} d\varphi\,\frac{\operatorname{Arsinh}(r)}{\sqrt{1+r^2}}\frac{F(r,\varphi;\mathcal{A},z)}{G(r,\varphi;\mathcal{A},\mathcal{M},\lambda,z)} \tag{3.18}$$

with

$$F(r,\varphi;\mathscr{A},z) \equiv \mathscr{A}z^2r^2\cos^2\varphi + 1, \tag{3.19}$$

$$G(r,\varphi;\mathscr{A},\mathscr{M},\lambda,z) \equiv \left(\frac{F-1}{\lambda} + \log z + \frac{\sqrt{1+r^2}}{r}\mathrm{Arsinh}(r)\right)F + \frac{\mathscr{M}}{\lambda}z^2r^2\sin^2\varphi \tag{3.20}$$

where we defined the dimensionless parameters

$$\mathscr{A} \equiv \frac{4\tilde{\Delta}^2}{v^2B}A, \quad \mathscr{M} \equiv \frac{4\tilde{\Delta}^2}{B^2}\frac{M_\mathrm{S}^2}{\gamma^2}, \quad z \equiv \frac{\Delta}{\tilde{\Delta}}, \quad \lambda \equiv \frac{g^2}{2\pi vB}. \tag{3.21}$$

The solution to the gap equation relative to the mean-field solution z thus depends on the values of $\mathscr{A}$, $\mathscr{M}$ and the "BCS parameter" λ. If no solution to Eq. (3.15) exists, i.e. if X, which is always positive, is too large to be compensated by the logarithm in (3.15), the minimum of the ground state energy is shifted back to $\Delta = 0$ due to the fluctuations.

Note that for $A = M_\mathrm{S}/\gamma = 0$ the integral (3.18) is logarithmically UV-divergent, complying with the results in BCS theory in Ref. [66]. This divergence is remedied as soon as either A or M_S/γ take on a finite value, in accordance with our conjecture that either of these parameters allow the fluctuations to be controlled. The numerical solutions to the gap equation for different combinations of the dimensionless parameters can be seen in Fig. 3.3. We find that indeed for small values of $\mathscr{A}$ and $\mathscr{M}$ the fluctuations do not allow for any notion of spontaneous symmetry breaking and mean-field theory fails completely, while above a certain threshold (even if either of the parameters vanishes), the minima of the ground state energy persist and the only effect is a lowering of the Majorana mass gap Δ to values as low as $z \sim 0.6$.

This threshold can be interpreted as the transition region, separating the two regimes (I) without broken symmetry, with short magnetic coherence length and free massless Majorana modes and (II) with broken magnetic symmetry and spin canting, leading to a finite ground state expectation value $\langle gm_x\rangle = \Delta$, establishing a finite Majorana mass gap and a magnetic coherence length which is exponentially large at low temperatures.

In Fig. 3.3, the quantum phase transition between (I) and (II) seems to be of first order with the order parameter discontinuously jumping to zero at the boundary (see also Fig. 3.4, where the shape of the fluctation-corrected ground state energy is depicted as a function of the stiffnesses). In Refs. [69, 70], apparently related phase transitions, respectively in a system of an anti-ferromagnet coupled to the edge of a $p_x + ip_y$ superconductor and Majorana chains with minimally nonlocal interactions, have been found to be described by the tricritial Ising (TCI) conformal field theory with central charge $c = 7/10$. Most likely, our transition belongs to this universality class as well (see also Section 3.1.5) and the Gaussian approximation employed here cannot be trusted in its vicinity, but only provides evidence for the existence of the two distinct phases. In addition, it offers an estimate on the parameter regime in which the transition takes place.

A further insight into the problem is provided by analyzing the relation between the Higgs frequency of the order parameter and the fermionic gap. It is well known that in the case of phonon-induced superconductivity, the Higgs mass, which is the frequency of the Higgs mode at $q = 0$, is given by $\omega(q = 0) = 2\tilde{\Delta}$ and thus lies exactly on the edge of the quasiparticle continuum [71, 72]. In contrast, in Peierls systems, $\omega(q = 0) \ll \tilde{\Delta}$. This result has been obtained in Refs. [63] and [64] and was also discussed in detail in Ref. [65]. In our case, the Higgs mass is determined by $\det \mathcal{D}^{-1}_{q=0,i\omega} = 0$. For $\Delta = \tilde{\Delta}$, $M_\mathrm{S}/\gamma = 0$, it follows to

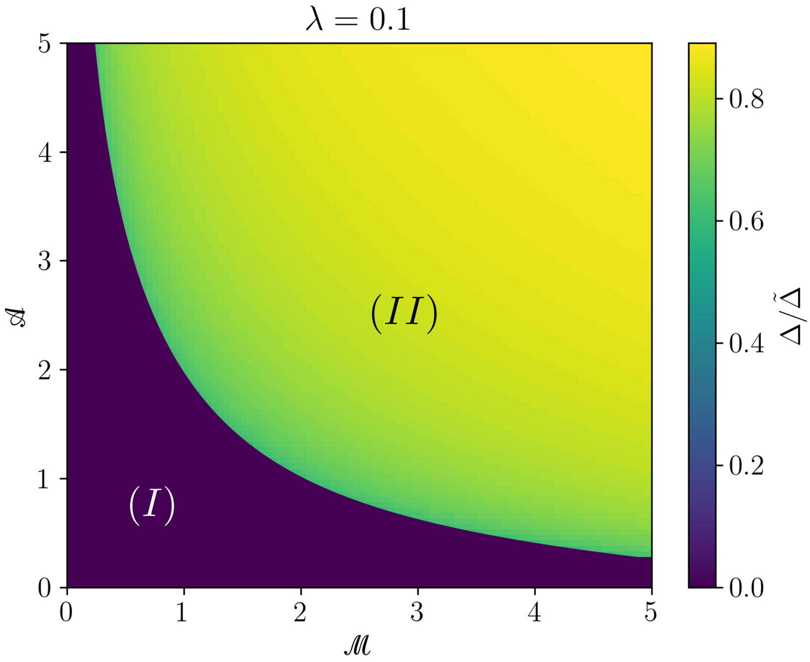

Figure 3.3: **Phase diagram of the SMS junction with strong easy-axis anisotropy.** Shown by color are the solutions $\Delta/\tilde{\Delta}$ to the gap equation (3.15) for $\lambda = 0.1$. $\Delta = 0$ corresponds to no solution existing. Regions of order with broken Ising symmetry and magnetization canting are labeled (II), and the disordered phase, where fluctuations destroy the ordered state, is labeled (I). If $\mathscr{A} = 0$, a solution $\Delta/\tilde{\Delta} \neq 0$ is obtained for $\mathscr{M} \gtrsim 13$ and vice versa.

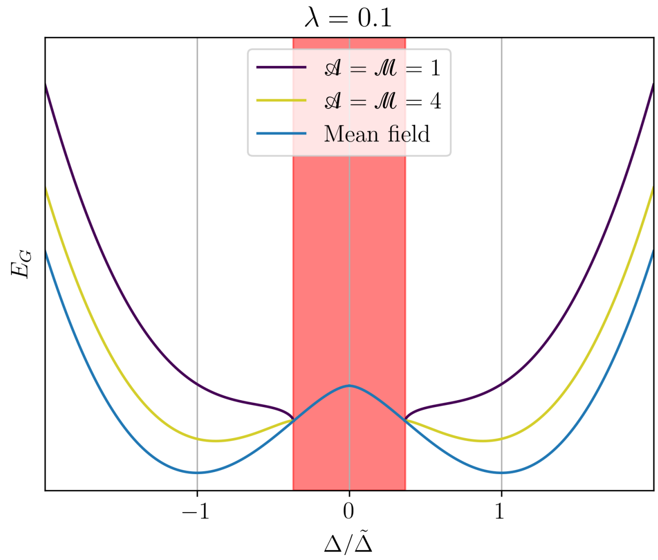

Figure 3.4: **Fluctuation-corrected ground state energies** of the SMS junction as a function of the order parameter $\Delta/\tilde{\Delta}$ following from Eq. (3.14) for $\mathscr{A}, \mathscr{M} \to \infty$ (corresponding to mean-field theory) as well as $\mathscr{A} = \mathscr{M} = 1$ and $\mathscr{A} = \mathscr{M} = 4$. In the latter case, the minima are preserved but shifted to $\Delta/\tilde{\Delta} < 1$ (cf. Fig. 3.3), while for smaller values of the stiffnesses, the minima vanish, which we interpret as the disordered phase with zero order parameter. Note that the second-order expansion in δm_x resulting in Eq. (3.14) is unstable for $\Delta/\tilde{\Delta} < 1/e$ (red area in the figure) but since the minima vanish well before that point, our argument remains valid.

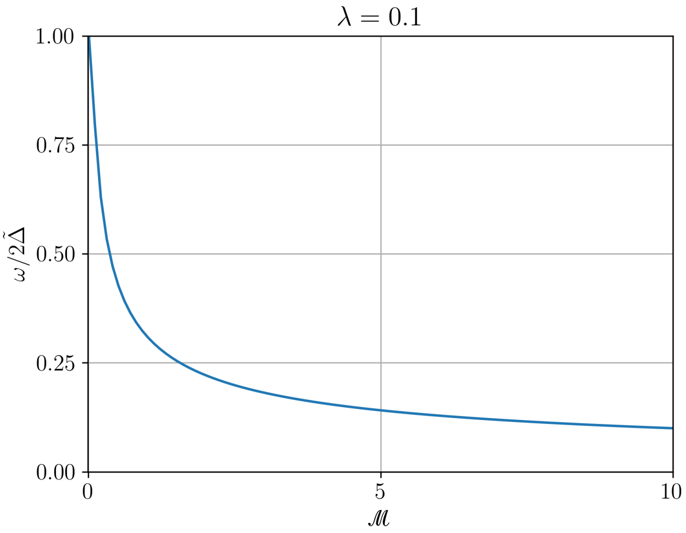

Figure 3.5: **The Higgs gap**, following from $\det \mathcal{D}^{-1}_{q=0,i\omega} = 0$, as a function of $\mathscr{M}$ (for simplicity with $\Delta = \tilde{\Delta}$). For increasing $\mathscr{M}$, it is shifted further and further away from the quasiparticle continuum at $\omega = 2\tilde{\Delta}$.

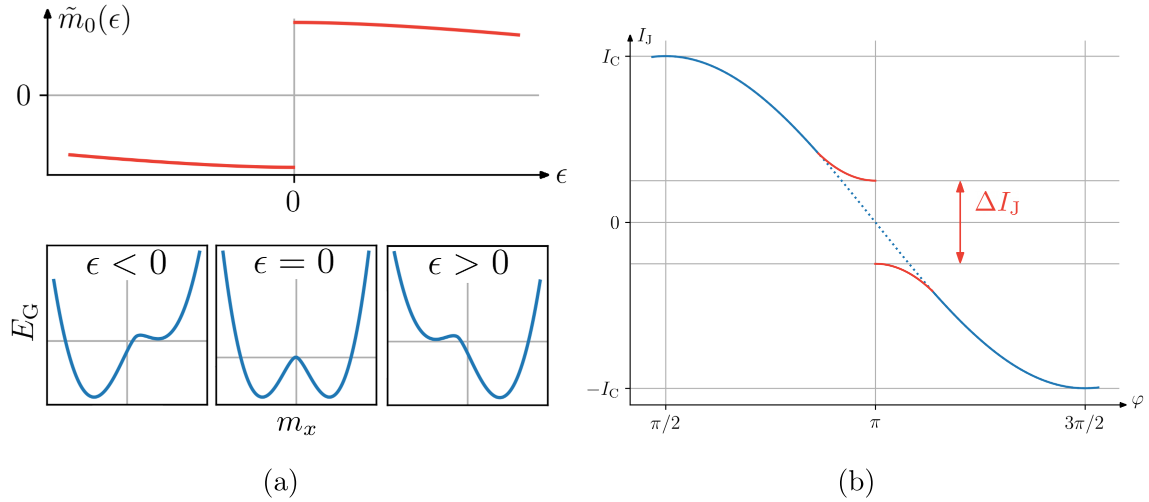

Figure 3.6: **Jump in the current-phase relation.** a) Allowing for the phase difference φ between the superconductors to deviate from π by $\epsilon = \pi - \varphi$ lifts the ground state degeneracy. The mean-field value of m_x is positive (negative) for positive (negative) ϵ with a first order transition at $\epsilon = 0$. b) At mean-field level, this leads to a discontinuity of magnitude $\Delta I_J = 4eBL\tilde{m}_0$ in the current-phase relation, which could be probed experimentally.

be $\omega(q = 0) = 2\tilde{\Delta}$. A non-zero value of M_S/γ now reduces the Higgs mass, as illustrated in Fig. 3.5, in accordance with the above cited works on Peierls systems. This departure from the continuum leads to the Higgs mode being underdamped. Increasing the value of A additionally shifts the spectral weight of the fluctuations to lower energies.

3.1.4 Experimental signature: Discontinuity in the current-phase relation

Until now we have assumed the phase difference between the superconductors to be fixed to $\varphi = \pi$. In Appendix A.1, it is shown that allowing $\epsilon = \pi - \varphi$ to take on a small, non-zero value leads to a hybridization between the Majorana modes of the form

$$H_{\text{hybr.}} = -ig \int dy \left(m_x + \frac{v_F}{2MW}\epsilon \right) \chi_R \chi_L . \tag{3.22}$$

The mean-field ground state energy then is given by

$$\frac{E_G}{L} = \frac{E_0}{L} + \frac{1}{2}Bm_x^2 + \frac{g^2}{4\pi v}\left(\log \left| \frac{g\left(m_x + \frac{v_F}{2MW}\epsilon\right)}{2v\Lambda} \right| - \frac{1}{2} \right) \left(m_x + \frac{v_F}{2MW}\epsilon \right)^2 . \tag{3.23}$$

As sketched in Fig. 3.6a, a deviation of φ from π thus lifts the degeneracy of the ground state and, in the mean-field approximation, m_x takes on a value $\tilde{m}_0(\epsilon > 0) > 0$ and vice versa. The transition at $\epsilon = 0$ is of first order. It corresponds to the standard first-order transition in the ordered phase of the Ising model, where ϵ plays the role of an external magnetic field (see also Section 3.1.5).

The Josephson current is given by $I_J = 2e\,\partial F/\partial\varphi$, where F is the free energy. At zero temperature, the current carried by the Majorana modes near $\varphi = \pi$ consequently reads

$$\frac{I_{\mathrm{J}}^{\mathrm{Maj}}}{L} = -\frac{2e}{L}\frac{\partial E_G}{\partial \epsilon} = 2eB\tilde{m}_0(\epsilon). \tag{3.24}$$

In particular, it exhibits a discontinuity at $\epsilon = 0$. In the parameter regime (II) of Fig. 3.3, this discontinuous jump persists when taking Gaussian fluctuations of m_x around the mean-field value into account. As it is an IR effect, the discontinuity will furthermore not be compensated by considering the higher-energy scattering states in addition to the Majorana modes. A sketch of the expected current-phase relation is provided in Fig. 3.6b.

Measuring the Josephson current in the phase-biased junction and examining it for a discontinuous jump thus provides a possibility to experimentally confirm the Ising-like properties we predict.

In order to estimate the magnitude of the jump compared to the critical Josephson current, let us for simplicity assume that $K \approx 1$, where K is the parameter defined in Appendix A.1. This is the case if for example $W \ll v_{\mathrm{F}}/\sqrt{\mu^2 - M^2}$. The ratio between the jump $\Delta I_{\mathrm{J}} = 4eBL\tilde{m}_0(\epsilon = 0)$ and the characteristic current scale $I_0 = eL\Delta_0^2/v$ is then given by

$$\frac{\Delta I_{\mathrm{J}}}{I_0} = \frac{4}{\pi}\frac{g}{\Delta_0}\frac{e^{-1/\lambda}}{\lambda}, \tag{3.25}$$

where $g/\Delta_0 = MW/v_{\mathrm{F}}$ and we took the cut-off to be $v\Lambda = \Delta_0$. Now, suppose $\lambda^{-1} = 10$, as we did above. The Fermi velocity of the topological insulator $\mathrm{Bi_2Se_3}$ has been experimentally determined to be $\hbar v_{\mathrm{F}} \approx 0.4\,\mathrm{eV\,nm}$ with a Fermi energy of $\mu \approx 0.3\,\mathrm{eV}$[73, 74]. Assuming the junction to have a width of $W \sim 1\,\mu\mathrm{m}$, it follows that a value of $\Delta I_{\mathrm{J}}/I_0 \sim 0.05$ could be achieved with a magnetization energy of $M \approx 30\,\mathrm{meV}$, which is experimentally feasible [75, 76] (see also the discussion in Section 4.3).

3.1.5 Similarities to the Blume-Capel model

In Ref. [70], an insightful similarity between Majorana systems which exhibit a $\mathbb{Z}_2$ symmetry breaking phase transition and the Blume-Capel model [77, 78] is pointed out. Since it provides a framework with which to understand a seemingly fine-tuned point, in form of the TCI universality class, to be generically realized here, we would like to present their argument in the following.

The Blume-Capel model is given by a quantum spin-1 chain

$$H_{\text{B-C}} = -\sum_j \left[S_j^z S_{j+1}^z - \gamma S_j^x - \delta (S_j^z)^2\right] \tag{3.26}$$

and corresponds to a two-dimensional classical Ising model with annealed vacancies (with chemical potential δ). Since $\delta \to -\infty$ suppresses the occurrences of these vacancies, the model maps in this limit to the standard transverse field Ising model and thus exhibits a second order Ising phase transition as a function of γ between a paramagnetic and a ferromagnetic phase. For $\gamma = 0$ on the other hand, the model is classical and a first order phase transition can be determined. The point where these two transition lines meet is the TCI point. The corresponding phase diagram is sketched in Fig. 3.7a.

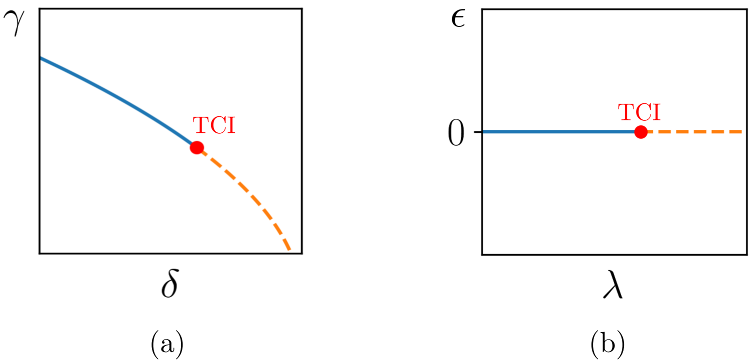

(a) (b)

Figure 3.7: **Phase diagram of the Blume-Capel model** in (a) and the analogous sketch for the SMS junction in (b). The blue solid line corresponds to a second order Ising phase transition, which meets a first order transition line (orange dashed) at the tricritical Ising point (red).

We can make out an analogy between the Blume-Capel model and our problem by recognizing that the two corresponding dimensionless parameters can, for instance for fixed values of M_S and A, be taken to be λ and $\epsilon = \pi - \varphi$. As soon as ϵ is non-zero, there is a Majorana mass and the system is gapped out (corresponding to the staggering in Ref. [70]). For $\epsilon = 0$ and small λ, the system exhibits free Majoranas, which we know to be equivalent to the critical Ising CFT. For large values of λ, we argued in Section 3.1.4 a first order phase transition to take place when ϵ crosses zero. All in all, we can thus speculate the phase diagram, as sketched in Fig. 3.7b, to closely resemble the Blume-Capel model. With this in mind, it starts to become clear that the TCI class might be the most natural way to transition from a $c = \frac{1}{2}$ massless Majorana, i.e. critical Ising, phase to one with an Ising-like spontaneously broken symmetry.

3.1.6 Magnetic solitons

In the parameter regime (II) of Fig. 3.3 we argued, in analogy with the Ising model, the magnetic coherence length to be given by $\xi_m \sim b\, e^{E_{\mathrm{DW}}/T}$ with E_{DW} and b the energy and width of a domain wall between regions with $\langle m_x \rangle = \pm m_0$, respectively. Such domain walls, which are responsible for the lack of long-range order at $T > 0$, correspond in mean-field theory to saddle points of the effective action (3.6) with non-constant m_x. For static but spatially varying configurations $m_x = m_0(y)$ which extremize the effective action, it holds

$$(-A\partial_y^2 + B)\, m_0(y) = \frac{ig}{2} \sum_j u_j(y) v_j^*(y) \tanh(E_j/2T) \tag{3.27}$$

with $(u_j(y), v_j(y))$ being the solutions to the BdG equation in $(\chi_{\mathrm{R}}, \chi_{\mathrm{L}})$-space with eigenenergies E_j

$$\begin{pmatrix} -iv\partial_y & igm_0(y) \\ -igm_0(y) & iv\partial_y \end{pmatrix} \begin{pmatrix} u_j(y) \\ v_j(y) \end{pmatrix} = E_j \begin{pmatrix} u_j(y) \\ v_j(y) \end{pmatrix}. \tag{3.28}$$

A single domain wall, or soliton, in the system is then given by the configuration $m_0(y)$ self-consistently solving these two equations and asymptotically approaching the mean-field solutions $m_0(y \to \pm\infty) = \pm\tilde{m}_0$ or $m_0(y \to \pm\infty) = \mp\tilde{m}_0$ with a single switch of the sign at some value of y, which we take to be 0 without loss of generality.

In this case the BdG solutions generally consist of a continuous spectrum for energies $|E_j| > g\tilde{m}_0$, one zero-energy MBS as well as other ABS with discrete non-zero in-gap energies localized near $y = 0$, where the number of ABS is dependent on the width of the soliton, while the MBS is always present at a zero-crossing (see Refs. [36, 79] and Section 2.2.2).

For the case $A = 0$, in the present model with the fluctuations thus dampened by a sufficiently large $\mathcal{M}$, there is extensive literature [80–84] on the exact one-soliton and multi-soliton solutions to this and generalized problems. The solutions are obtained by employing methods of inverse scattering theory. The one-soliton solution is shown to read

$$m_0(y) = \pm\tilde{m}_0 \tanh(y/b) \tag{3.29}$$

with the width of the domain wall given by $b = \frac{v}{g\tilde{m}_0}$. This soliton only carries a single bound state, namely a MBS. The energy E_{DW} is given by the difference between the mean-field energy in presence of a soliton $E_{\mathrm{MF}}[m_0(y)]$ and the ground-state energy $E_{\mathrm{G}} = E_{\mathrm{MF}}[\tilde{m}_0]$ and follows to be [82]

$$E_{\mathrm{DW}} = E_{\mathrm{MF}}[m_0(y)] - E_{\mathrm{MF}}[\tilde{m}_0] = \frac{g\tilde{m}_0}{2\pi}, \tag{3.30}$$

wherein the zero-energy state also contributes by lowering the continuum density of states through its appearance.

It is to be expected that a small, non-zero value of A will in a first approximation only alter the length scale of the transition, making it wider and at some point leading to additional bound states to arise, while the overall shape of the soliton is preserved.

Finding a uniformly moving soliton-solution is non-trivial and cannot be achieved by a simple ‘boost’ of the stationary solution, as only the fermionic part of the action is Lorentz invariant, while the magnetic action possesses Galilean invariance in the following sense: if $(m_x(y,t), m_y(y,t))^T$ is a solution to the (real-time) equations of motion of the free magnetization field, so is

$$\begin{pmatrix} \cos\phi_u(y,t) & -\sin\phi_u(y,t) \\ \sin\phi_u(y,t) & \cos\phi_u(y,t) \end{pmatrix} \begin{pmatrix} m_x(y-ut) \\ m_y(y-ut) \end{pmatrix}, \tag{3.31}$$

where $\phi_u(y,t) = \frac{uM_{\mathrm{S}}}{2\gamma A}\left(y - \frac{u}{2}t\right)$ (this is analogous to the Galilean invariance of the 1D nonlinear Schrödinger equation). The coupling between m_x and m_y, present due to M_{S}/γ if either of the magnetization field components is time dependent, therefore necessitates a moving soliton to include rotation of the magnetization around the z-axis.

However, as is the case deep in the ordered phase of the transverse-field Ising model, the dynamical soliton mass can be expected to be very large and the inclusion of only stationary solutions to the statistical argument thus to provide a good approximation.

We leave further analysis of the cases with non-zero A and non-stationary solitons for possible future work.

3.2 Junctions of time-reversal invariant topological superconductors

Until now we have considered topological superconductivity engineered by depositing an s-wave superconductor on the surface of a 3D strong TI. In order to understand whether the physics we

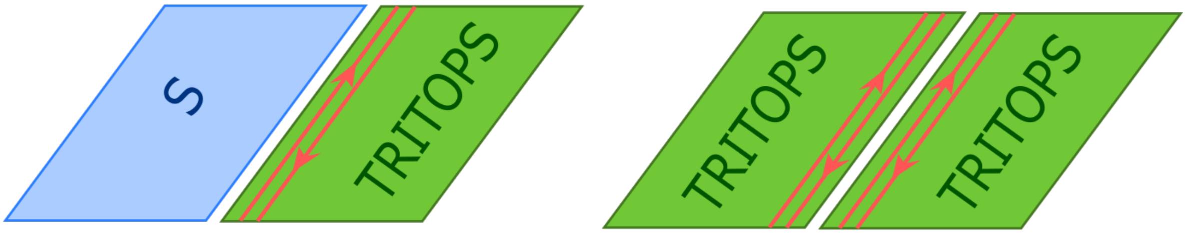

Figure 3.8: **Sketches of the TRITOPS-S and TRITOPS-TRITOPS junction.** In the TRITOPS-S case, the Kramers pair of edge modes of the 2D time-reversal invariant topological superconductor (TRITOPS) can couple via the supragap states of the non-topological superconductor (S). The same holds true in the TRITOPS-TRITOPS junction, but in addition the edge modes on either side directly couple with each other as well.

discussed above is more broadly applicable, in the following we are instead interested in a more general class of models describing topological superconductivity which preserve time-reversal symmetry. Specifically, we consider models belonging to the DIII-class defined in Ref. [85], which are often referred to as TRITOPS (time-reversal invariant topological superconductors). Consequently, edge modes appear in Kramers pairs here. Some proposals for realizing this topological phase in one- and two-dimensional systems can be found in Refs. [86–92].

Josephson junctions involving two-dimensional TRITOPS (see Fig. 3.8) were previously studied in Ref. [93]. The hybridization of the Kramers pairs of counter-propagating helical Majorana modes in these Josephson junctions defines, depending on the nature of the system, up to two masses $m_1(\varphi)$ and $m_2(\varphi)$, which depend on the phase bias φ. Interestingly, when the junction is formed between a TRITOPS and a time-reversal invariant non-topological superconductor (S), the behavior of $m_2(\varphi)$ turns out to be such that a quantum phase transition to a state with spontaneously broken time-reversal symmetry at the junction is possible, in analogy to the Peierls instability in the SMS junction we studied above. In this symmetry-broken state the equilibrium value of the phase takes values $\varphi \neq n\pi$ with n integer.

Analogously to Section 3.1.3, in the following we aim to analyze fluctuations of φ in the TRITOPS-S junction and the stability of the state with broken time-reversal symmetry. Additionally, we introduce and study the effect of vortices in these types of junctions as well as in TRITOPS-TRITOPS junctions, where no spontaneous breaking of time-reversal symmetry takes place.

3.2.1 Description of the junctions

We consider the 1+1D effective action $S = S_\varphi + S_{\eta-\varphi}$, which describes the joint dynamics of the phase bias along the junction φ and its coupling to the TRITOPS' edge modes η. The two contributions read

$$S_\varphi = \int dy\, dt \left\{ \frac{K}{2} \left(\frac{1}{c_{\mathrm{J}}} \left(\partial_t \varphi\right)^2 - c_{\mathrm{J}} \left(\partial_y \varphi\right)^2 \right) - E_{\mathrm{J}} \left(1 - \cos\varphi\right) \right\} \tag{3.32}$$

as well as

$$S_{\eta-\varphi} = \frac{1}{2} \int dy\, dt\, \eta^\dagger \left(i\partial_t - \mathcal{H}\right) \eta, \tag{3.33}$$

with the Dirac Hamiltonian

$$\mathcal{H} = -iv\alpha\partial_y + g_1(\varphi)\beta_1 + g_2(\varphi)\beta_2. \tag{3.34}$$

The precise expressions for the matrices α and $\beta_{1,2}$ depend on the type of junction and will be given below. Compared to the action in Eq. (3.4), in addition to the different nature and dynamics of the involved bosonic fields, note that the Majorana spinor η can either have two components, as before, when considering TRITOPS-S junctions, or four components when considering TRITOPS-TRITOPS junctions.

S_φ describes the dynamics of the phase, taking into account the effect of the states above the gap only and corresponds to the sine-Gordon equation [42].

E_J is the Josephson energy density per length, which is related to the amplitude of the Josephson current density (per length) $J(\varphi) = J_0 \sin(\varphi)$ via $J_0 = 2eE_\mathrm{J}/\hbar$.

The gradient contributions to S_φ originate in the energies of the electric and magnetic fields. The action assumed here corresponds to a 3D situation, i.e. a junction of sufficiently large height $h_z \gg \lambda_{1,2}$, where $\lambda_{1,2}$ are the respective London penetration depths. In this regime the junction forms a wave guide with most of the magnetic and electric energies bound to its volume. The phase rigidity K and the effective light velocity (Swihart velocity) c_J are then determined by the geometry of the junction and given by $c_\mathrm{J}^2 = c^2 d_0/d$, $K = ch_z/(16\pi e^2\sqrt{dd_0})$. Here d_0 is the width of the insulating barrier separating the two superconductors and $d = d_0 + \lambda_1 + \lambda_2$ [94]. If h_z becomes too small, $h_z \ll \lambda_{1,2}$, stray magnetic fields extending outside of the junction need to be considered, leading to a non-local effective action [95].

Although the effective models for the topological superconductors considered in the present work are two-dimensional, the mechanisms to generate such phases are typically by proximity to three-dimensional superconductors. [92] We assume these 3D superconductors to provide the necessary suppression of the stray magnetic fields through their height h_z, acting as a wave guide and allowing us to consider a purely local theory. Note that in the usual 3D Josephson junctions the Josephson energy density E_J per length is also proportional to h_z [94, 96]. In that case, one introduces the Josephson energy density per area so that the height h_z becomes a prefactor of the whole action S_φ, which can effectively be reformulated such that K is the prefactor of S_φ. In contrast, here the Josephson tunneling takes place only between the 2D superconducting layers, thus our Josephson energy density per length, E_J, is completely unrelated to K.

$S_{\eta-\varphi}$ describes the coupling between the Majorana edge states and the phase. The details depend on the type of junction, which is characterized by the mass terms $m_{1,2}(\varphi)$ and the number of Kramers pairs of counterpropagating Majorana modes involved. The latter defines the structure of the spinor η (see Ref. [93]). v is the velocity of the Majorana modes.

In the action introduced in Eqs. (3.32)-(3.34) we consider two mass terms. The first one is denoted by $m_1(\varphi)\beta_1$ and corresponds to a coupling between the edge modes on both sides of the junction. Its leading contribution is of first order in the tunneling element t_J.

The second mass term in Eq. (3.34), denoted by $m_2(\varphi)\beta_2$, is due to the virtual coupling of edge modes on one side of the junction to states above the gap on the other side. Hence, it effectively couples the edge modes within each superconductor and is of order $t_\mathrm{J}^2/\Delta_\mathrm{eff}$ with Δ_eff being the magnitude of the superconducting gap. Obviously, for the TRITOPS-S junction m_2 is the only possible mass term.

We now summarize the description on the basis of low-energy Hamiltonians describing a spin-preserving tunneling (t_{J}) at the Josephson junction, in part making use of the results presented in Ref. [93]. For the TRITOPS-S junction there is a single pair of counter-propagating Majorana modes. Consequently, η is a two-component spinor and we have

$$\alpha = \tilde{\sigma}_z, \quad \beta_2 = \tilde{\sigma}_y, \tag{3.35}$$

$$g_1(\varphi) = 0, \quad g_2(\varphi) = g_2^{(0)} \sin(\varphi). \tag{3.36}$$

(TRITOPS-S)

The Pauli matrices $\tilde{\sigma}$ act on the two members of the Majorana Kramers pair. The edge modes of the TRITOPS are coupled to the supragap states of the non-topological superconductor S. As mentioned before, the non-vanishing mass term $g_2^{(0)} \propto t_{\mathrm{J}}^2/\Delta_{\mathrm{eff}}$ is originated in a second-order process in the tunneling amplitude.

In distinction, for the TRITOPS-TRITOPS junction, η is a spinor with four components corresponding to the two Kramers pairs associated to the two TRITOPS (labeled by S_1, S_2), and we have

$$\alpha = \tilde{\tau}_z\tilde{\sigma}_z, \quad \beta_1 = \tilde{\tau}_y\tilde{\sigma}_z, \quad \beta_2 = \tilde{\tau}_0\tilde{\sigma}_y, \tag{3.37}$$

$$g_1(\varphi) = g_1^{(0)} \cos(\varphi/2), \quad g_2(\varphi) = g_2^{(0)} \sin(\varphi). \tag{3.38}$$

(TRITOPS-TRITOPS)

$\tilde{\tau}_j$ are Pauli matrices acting in the S_1, S_2 subspace. Here, the mass term modulated by $g_1^{(0)} \propto t_{\mathrm{J}}$ is generated by the hybridization of the Majorana edge states at both sides of the junction. This is the leading order in the tunneling t_{J} and it becomes exact when the superconducting gap is large enough $\Delta_{\mathrm{eff}}/t_{\mathrm{J}} \to \infty$ to prevent the hybridization of the edge modes on one side of the junction with the supragap states of the other side. The second mass term $g_2(\varphi)$ is a second-order perturbation with $g_2^{(0)} \propto t_{\mathrm{J}}^2/\Delta_{\mathrm{eff}}$ and has to be taken into account when the edge states on one of the TRITOPSs hybridize, not only with the edge states, but also with the supragap states of the other TRITOPS.

To identify the 4×4 matrices α and $\beta_{1,2}$ of Eq. (3.37) that determine the Dirac Hamiltonian $\mathcal{H}$ for the TRITOPS-TRITOPS junction, we analyze the behavior under time reversal, charge conjugation, and under the exchange of the two identical TRITOPS. Time reversal corresponds to simultaneously transforming $\varphi \to -\varphi$ and $\mathcal{T} = i\tilde{\tau}_0\tilde{\sigma}_y\mathcal{K}$ in the fermion sector. The charge conjugation operator $\mathcal{C} = U_C\mathcal{K}$ acts on the BdG Hamiltonian as $U_C\mathcal{H}U_C^{-1} = -\mathcal{H}^*$. We use a basis with real field operators $\eta^\dagger = \eta$. In this basis $U_C = 1$ and thus $\mathcal{H} = -\mathcal{H}^*$. Finally, the exchange symmetry of the two superconductors S_1 and S_2 corresponds to simultaneously transforming $\varphi \to -\varphi$ and $U_X = \tilde{\tau}_x\tilde{\sigma}_x$ in the fermion sector. The conditions of time-reversal, charge-conjugation, and exchange symmetry uniquely determine the matrices for the TRITOPS-TRITOPS junction. In Appendix A.3 we give further details on the derivation of these symmetries. The underlying assumptions are $p_\pm$ type of pairing in both superconductors and spin-preserving tunneling at the junction.

The transformation $\varphi \to -\varphi$ is necessary if the phase φ is a genuine dynamic variable. However, if one considers the properties of the fermionic sector for a fixed configuration $\varphi\,(y)$, the mass term $g_2\,(\varphi)$ breaks both, the time-reversal and the exchange symmetry. This will be important when we analyze the fermionic spectrum near given soliton solutions of the phase.

3.2.2 Fluctuation analysis and phase diagram

The distinct dependency of the edge-mode mass $g_{1,2}(\varphi)$ for the two junctions, given in Eqs. (3.36) and (3.38), gives rise to qualitatively distinct behavior. For the TRITOPS-TRITOPS junction, the net mass at $\varphi = 0$ is finite while it vanishes for the TRITOPS-S junction. This is consistent with the bulk-boundary correspondence; see Ref. [93] for a discussion. As we will see in the proceeding section, a fermion zero mode will only be associated with a phase slip soliton if the fermion is massive at constant phase. For the TRITOPS-S, this requires spontaneously breaking time-reversal symmetry with an equilibrium phase $\tilde{\varphi}_0 \neq n\pi$. In this case, the protecting symmetry of the massless edge modes is spontaneously broken for the TRITOPS-S junction and the bulk-boundary correspondence does not apply.

We will see below that the stability of the time-reversal symmetry broken state depends on the value of the rigidity K, analogously to the situation in Section 3.1.3. The symmetry is broken for large values of K and hence large values of h_z, while at small K quantum fluctuations are important and restore the symmetry. The ordered state is characterized by an Ising variable that describes the two states $\pm\tilde{\varphi}_0 \,\mathrm{mod}(2\pi)$. The quantum phase transition is then expected to be in the tricritical Ising universality class, the natural transition from an Ising ordered phase to a massless, critical phase that corresponds to the critical point in the usual Ising model (see Refs. [69, 70] and Section 3.1.5).

In our analysis we are rather interested in the quantitative location and parameter dependence of this transition and in the properties of phase slips on the ordered side of the transition. The ordered state can be described in a controlled fashion in the limit of large rigidity K. To estimate the phase boundary, like in Section 3.1.3, we go beyond the mean field limit, valid at $K \to \infty$, and include fluctuation effects; the transition is estimated from the parameter regime where these fluctuations start to dominate the equation of state.

In a semi-classical approach, where the fermionic modes are treated in a full quantum mechanical framework, while $\varphi(y, t)$ is regarded as a classical field defined by its mean value with $K \to \infty$ in Eq. (3.32), the total energy density after integrating out all the fermionic modes of the junction in $\langle H_{\eta-\varphi}\rangle$ and adding the contribution of the supragap states reads

$$E_{\mathrm{G}}(\varphi)/L = E_{\mathrm{J}}\left[1-\cos(\varphi)\right] - \frac{g^2(\varphi)}{8\pi v}\left[1+\log\left(\frac{4v^2\Lambda^2}{g^2(\varphi)}\right)\right], \tag{3.39}$$

where $g^2(\varphi) = g_1^2(\varphi) + g_2^2(\varphi)$ is the net mass and $v\Lambda$ a high-energy cutoff of the order of the effective superconducting gap Δ_{eff}.

The contribution of the states above the superconducting gap, i.e. all states except for the edge modes, is given by the first term of Eq. (3.39) which has a minimum at $\varphi = 0$. As discussed above, the effect of the edge modes given by the second term does not affect this minimum in the TRITOPS-TRITOPS junction since $g(\varphi) \propto g_0 \neq 0$ at small φ, while a competing minimum may develop for the TRITOPS-S junction. In what follows we analyze the stability of this time-reversal symmetry breaking solution in the TRITOPS-S junction against the effect of the phase fluctuations introduced by a finite K in Eq. (3.32).

Under the assumption $\varphi \ll 1$, one finds the minima of the ground state energy-density (3.39) to be

$$\tilde{\varphi}_0^{(1/2)} = \pm\frac{2v\Lambda}{g_0}\exp\left(-\frac{\pi v E_{\mathrm{J}}}{g_0^2}\right) \neq 0, \tag{3.40}$$

hinting, as discussed, at a spontaneous symmetry breaking. However, we already know that one has to keep in mind the possibility of quantum fluctuations of φ destroying the phase with $\tilde{\varphi}_0 \neq 0$. This is exemplified by expanding the action in Eq. (3.32) up to second order in φ, which yields the Gross-Neveu-Yukawa (GNY) model in 1+1 dimensions, a bosonized version of the Gross-Neveu model [97], $S \approx S_\varphi^{(0)} + S_{\eta-\varphi}$ with

$$S_\varphi^{(0)} = \int dy\, dt \left\{ \frac{K}{2} \left(\frac{1}{c_\mathrm{J}} (\partial_t \varphi)^2 - c_\mathrm{J} (\partial_y \varphi)^2 \right) - \frac{E_\mathrm{J}}{2} \varphi^2 \right\}. \tag{3.41}$$

In the limit $K \to 0$, integrating out φ results in a local 4-Majorana interaction which is RG irrelevant and thus no symmetry breaking takes place: in this limit, the mean-field approach is invalidated by fluctuations. Since the stiffness K suppresses the fluctuations (and renders the effective 4-Majorana interaction non-local), we expect a quantum phase transition at some positive value of K, beyond which the non-zero expectation value of φ is stabilized. K plays here the role the magnetic rigidities took for the SMS junction.

Following the reasoning laid out in Section 3.1.3, we expand the GNY action up to second order in the fluctuations $\delta\varphi$ around some assumed minimum $\langle \varphi \rangle \equiv \varphi_0$ of the ground state energy, $\varphi(x,t) = \varphi_0 + \delta\varphi(x,t)$. After integrating out $\delta\varphi$, we derive the equation of state for φ_0 and examine whether it allows for solutions $\varphi_0 \neq 0$, i.e. whether the mean-field solution is consistent and only weakly affected by fluctuations. If this is the case, we conclude that fluctuations are small and the treatment in the limit of large rigidity therefore justified. If not, fluctuations are large, suppress long-range order, and the symmetry remains unbroken.

The fluctuation-corrected equation of state determining the gap in the Majorana spectrum reads

$$\frac{dE_\mathrm{G}}{d(\varphi_0^2)} = 0 \quad \Leftrightarrow \quad \log \left| \frac{\varphi_0}{\tilde{\varphi}_0} \right| + X_\varphi = 0, \tag{3.42}$$

with

$$X_\varphi = \frac{4}{\pi} \int_0^{\pi/2} d\theta \int_0^\infty dr \, \frac{\mathrm{Arsinh}(r)}{\sqrt{1+r^2}} \left[8\pi K \varphi_0^2 r^2 \left(\frac{v}{c_\mathrm{J}} \sin^2\theta + \frac{c_\mathrm{J}}{v} \cos^2\theta \right) \right. \\ \left. + \log \left| \frac{\varphi_0}{\tilde{\varphi}_0} \right| + \frac{\sqrt{1+r^2}}{r} \mathrm{Arsinh}(r) \right]^{-1}. \tag{3.43}$$

Here, (r, θ) are polar coordinates in the $\left(\frac{\omega}{2g_0\varphi_0}, \frac{vq}{2g_0\varphi_0}\right)$-plane. We calculate the integral numerically for different values of v/c_J and find the curve of critical values $\Gamma_c(v/c_\mathrm{J})$ depicted in Fig. 3.9, representing the minimum value $K\tilde{\varphi}_0^2$ needs to take on in order for solutions to Eq. (3.42) to exist and thus the symmetry breaking to be stable against Gaussian fluctuations.

The relevant experimental scenario corresponds to small values of $v/c_\mathrm{J} \ll 1$ ($\simeq 10^{-4} - 10^{-3}$), in which case a small value of $K\tilde{\varphi}_0^2$ is enough to guarantee the stability of the mean field solution. The precise value of K should anyway depend on the geometric details of the junction.

As already has been noted in Section 3.1.3, within the Gaussian fluctuation framework, the quantum phase transition is of first order. However, there is no reason to expect that the employed approximation properly describes the critical fluctuations at this transition correctly. As stated above, the quantum phase transition is expected to be in the tricritical Ising universality class, where all exponents are exactly known, while our approach is useful in getting an estimate of the phase boundary as function of the system parameters.

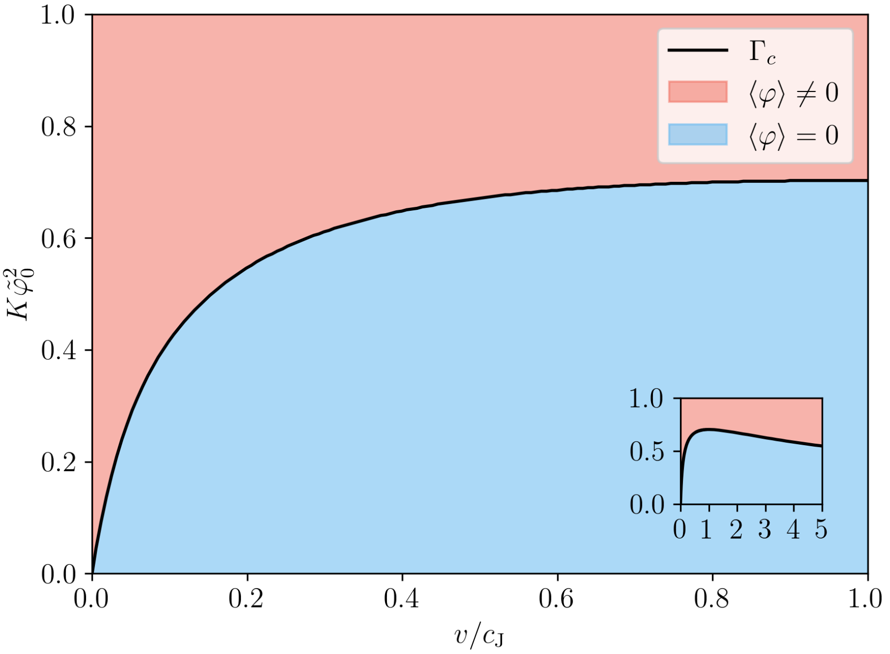

Figure 3.9: **Phase diagram of the TRITOPS-S junction** with the boundary Γ_c between symmetry broken (red) and unbroken (blue) phase determined from Eq. (3.42) for $v/c_\mathrm{J} \in [0, 1]$ (inset: $v/c_\mathrm{J} \in [0, 5]$).

3.2.3 Fermionic bound states at fluxons

Fluxons trapped in Josephson junctions lead to vortices and the formation of phase slip solitons. Specifically, one flux quantum corresponds to a 2π-phase slip along the junction [42]. Due to the logarithmic instability in the TRITOPS-S junction, however, assuming the system to be in the symmetry broken regime, two distinct types of solitonic solutions $\varphi_{S,1/2}(y)$ are possible, for which asymptotically $\varphi_{S,1}(y \to -\infty) = \varphi_0 \,(\mathrm{mod}\, 2\pi)$, $\varphi_{S,1}(y \to \infty) = 2\pi - \varphi_0 \,(\mathrm{mod}\, 2\pi)$ and $\varphi_{S,2}(y \to \pm\infty) = \pm\varphi_0 \,(\mathrm{mod}\, 2\pi)$, respectively, as depicted in Fig. 3.10. The equations governing the form and dynamics of these solitons is further discussed in Ref. [47]. For our purposes, knowledge of the asymptotic behavior is sufficient. Each type of soliton is associated with a phase change less than 2π and therefore a fractional fluxon (see Fig. 3.10b). Since both types of solitons still lead to a sign change of the mass term $g_2(\varphi)$ (see Fig. 3.10c), they each carry a Majorana zero mode

$$\Psi_0^{(1/2)}(y) \propto \begin{pmatrix} 1 \\ \pm 1 \end{pmatrix} e^{\mp \frac{1}{v} \int^y dy' g_2(\varphi_{S,1/2}(y'))}. \tag{3.44}$$

In contrast, time-reversal symmetry remains unbroken in the ground state of the TRITOPS-TRITOPS case and the equilibrium values of φ are separated by 2π. Taking into account for now only the larger of the two mass terms $g_1(\varphi)$, we find for solitonic profiles $\varphi_T(y)$ two (Kramers) degenerate Majorana zero modes near each fluxon

$$\Psi_{0,\uparrow}(y) \propto \begin{pmatrix} 1 \\ 0 \\ 1 \\ 0 \end{pmatrix} e^{\frac{1}{v} \int^y dy' g_1(\varphi_T(y'))}, \quad \Psi_{0,\downarrow}(y) = \mathcal{T}\Psi_{0,\uparrow}(y) \propto \begin{pmatrix} 0 \\ 1 \\ 0 \\ 1 \end{pmatrix} e^{\frac{1}{v} \int^y dy' g_1(\varphi_T(y'))}. \tag{3.45}$$

Now, including a generic but fixed configuration of the second mass term $g_2(\varphi)$ breaks time-reversal symmetry, as discussed in Section 3.2.1. Hence, one expects the Kramers degeneracy to be lifted. However, as long as both mass terms have a well defined parity under $y \to -y$ the spectrum continues to be doubly degenerate. For the soliton solution, both mass terms are odd under $y \to -y$. In this case one can identify two "pseudo-parity" operators

$$P_1 = \tilde{\tau}_0 \tilde{\sigma}_x p, \tag{3.46}$$

$$P_2 = \tilde{\tau}_x \tilde{\sigma}_z p, \tag{3.47}$$

with $pf(y) = f(-y)$. Both commute with the Hamiltonian $\mathcal{H}$ of Eq. (3.34), but do not commute with each other. More generally, P_1 and P_2 commute with $\mathcal{H}$ if $\varphi \to 2\pi - \varphi$ under $y \to -y$. Hence, the spectrum of $\mathcal{H}$ with masses that are odd under $y \to -y$ is doubly degenerate. To prove this, let Ψ_1 be a simultaneous eigenstate of $\mathcal{H}$ and P_1, then $\Psi_2 = P_2\Psi_1$ is a distinct eigenstate with same energy; the only alternative would be $\Psi_2 = 0$, which is not allowed since $P_2\Psi_2 = \Psi_1$ due to $P_2^2 = 1$. For $g_2 = 0$ we have exactly one pair of Kramers degenerate normalizable zero modes. As charge conjugacy requires eigenstates to occur in pairs of opposite energy, the pair must remain at zero energy, i.e. the pair of zero modes cannot be split by the mass term $g_2\beta_2$. Notice $\Psi_2 \neq \mathcal{T}\Psi_1$, i.e. the two zero modes are not Kramers pairs, but protected by the fact that both masses are odd in y. They do adiabatically connect to Kramers pairs at $g_2 \to 0$ though. In Appendix A.4 we explicitly demonstrate the

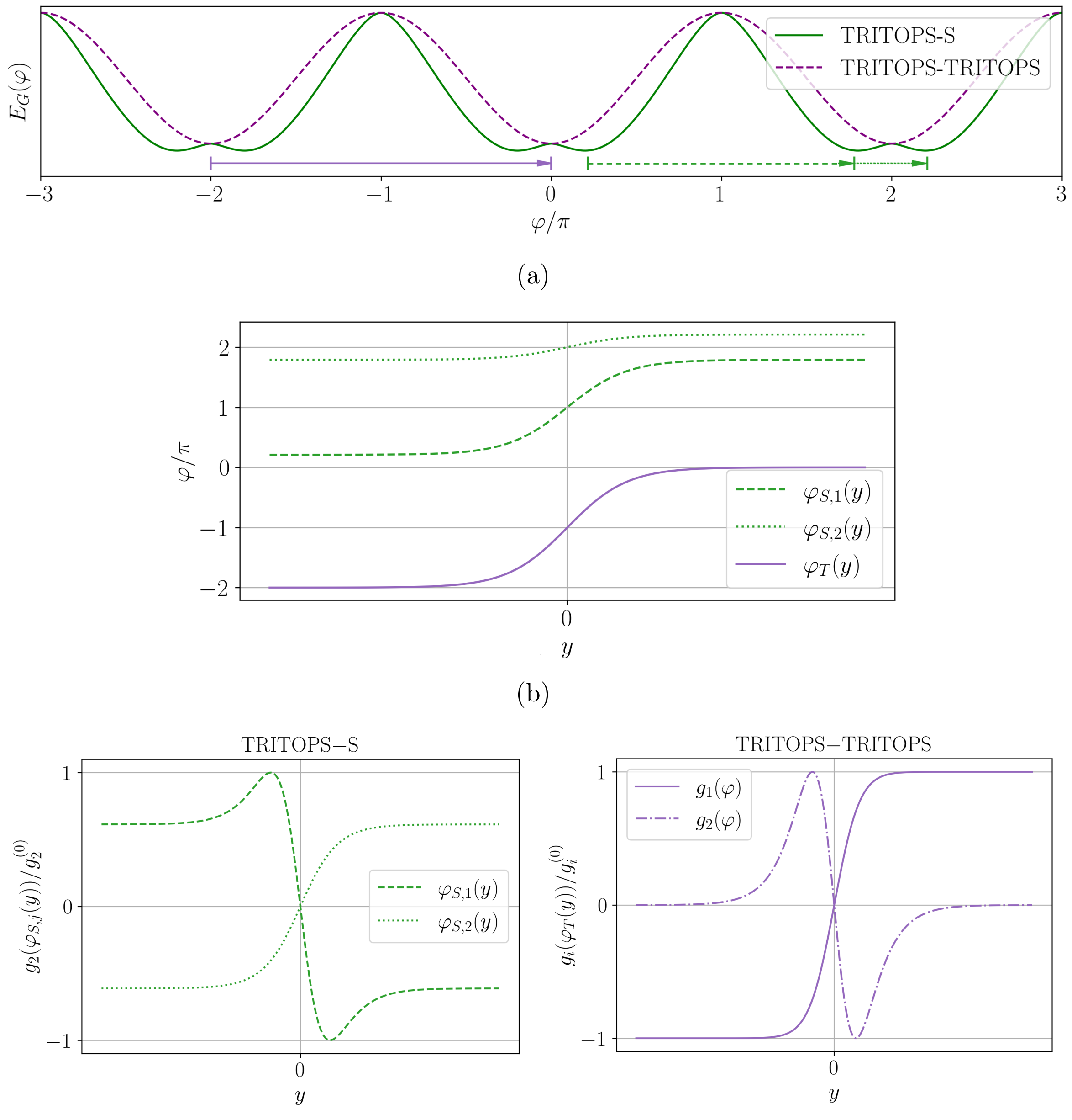

(a)

(b)

(c) (d)

Figure 3.10: **Solitons in TRITOPS junctions.** a) Sketch of the TRITOPS-S and TRITOPS-TRITOPS ground state energies as a function of φ. The minima connected by the solitons are depicted below for each case. Due to the spontaneous symmetry breaking in TRITOPS-S junctions, there are two distinct types of solitons possible. b) Sketch of the solitons as a function of y. c) Sketch of the mass profiles $g_2(\varphi_{S,j}(y))$ for the two kinds of solitons in the TRITOPS-S junction. d) Sketch of the two mass profiles $g_i(\varphi_T(y))$ for the soliton in the TRITOPS-TRITOPS junction. Note that $g_2(y \to \pm\infty) \to 0$.

existence of doubly-degenerate normalizable zero modes for given antisymmetric mass profiles $g_1(y)$ and $g_2(y)$, with $g_2(y)$ vanishing for $y \to \pm\infty$.

A discussion on the consequences of the presence of these bound fermionic modes on the collision dynamics of the solitons can be found in Ref. [47].

3.3 Summary

In this chapter, we have studied the dynamics of a ferromagnet's magnetization with large easy-axis anisotropy coupled to the one-dimensional Majorana modes in a topological insulator Josephson junction, as well as the corresponding situation regarding the phase bias in Josephson junctions comprised of at least one time-reversal invariant topological superconductor.

In both cases, we have encountered logarithmic Peierls-like instabilities, which lead to the formation of a Majorana mass gap if the stiffnesses of the respective bosonic field are sufficiently large. We estimated the location of the corresponding phase boundary beyond which the gap is stable against quantum fluctuations and, by analogy to related models, furthermore deduced the associated phase transition to likely belong to the tricritical Ising universality class.

Solitonic excitations in the gapped phase bind Majorana zero modes. In the SMS junction, these correspond to magnetic domain walls with nontrivial dynamics. In the TRITOPS-S junction, they can be understood as fractional fluxons.

In contrast, in the TRITOPS-TRITOPS junction, no Peierls instability and thus spontaneous breaking of time-reversal symmetry occurs. Despite the explicit breaking of time-reversal symmetry by introducing a fluxon, we found the would-be Kramers degeneracy to persist as a result of the well-defined soliton-parity.

Additionally, in the magnetic case we proposed an experiment which is able to probe whether the system is in the symmetry-broken phase. Namely, there we predict the Josephson current-phase relation to exhibit a discontinuity near a phase difference of $\varphi = \pi$, based on a first order phase transition taking place, as a value $\varphi \neq \pi$ lifts the $\mathbb{Z}_2$ ground state degeneracy.

4

Chapter 4

BKT transitions in topological SMS junctions

Our goal in this chapter is to generalize our earlier analysis of the topological SMS junction to take into account arbitrary magnetic anisotropy strengths. The phase transitions we encountered in the previous chapter can be brought in connection to the tricritical Ising point, since the disordered phase is described by a critical Ising theory itself – a direct result of the fermions' Majorana nature. In the SMS junction, this disordered phase corresponded to the magnetization being pinned to the z-axis, since we assumed a strong easy-axis anisotropy to be present in this direction. Relaxing this simplifying assumption, employing mean-field and renormalization group techniques, in the following we are able to reveal additional intriguing critical phenomena to exist in this model in the form of Berezinskii-Kosterlitz-Thouless (BKT) transitions. Notably, one of the BKT phases unexpectedly arises from a novel interplay between the anisotropy of the magnons and their interaction with the Majorana fermions. In combination with the tricritical Ising and possible further multicritical points, we thus are going to find these kinds of hybrid structure to be a promising platform for the realization of exotic quantum critical phenomena.

This chapter is based on Ref. [98] and most of its content has been adapted verbatim or very closely from this publication.

4.1 Generalization to arbitrary magnetic anisotropy strengths

As mentioned earlier in this thesis, the deposition of a ferromagnet in a topological insulator Josephson junction is usually proposed as practical means to alter and control the electronic surface states and the associated properties of the junction. In studying the interplay of magnetic and electronic degrees of freedom in the previous chapter, we have shown that this can result in a quantum phase transition. In the following, we would like to generalize the earlier effective theory to examine whether further such transitions occur in the model.

The effective action for the SMS junction on the surface of a 3D TI given in (3.4) has been derived for a strong magnetic easy-axis anisotropy with $m_x, m_y \ll 1$. If the exchange coupling between the magnetization and the TI surface states $\alpha|\vec{M}|$ in the Hamiltonian (3.1) can be treated perturbatively, this action can be generalized to arbitrary magnetic anisotropies.

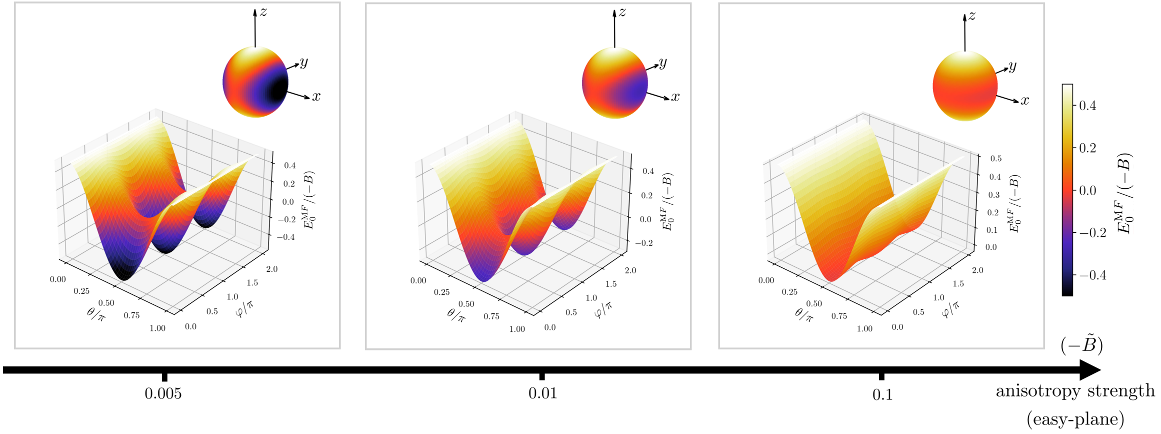

Figure 4.1: **Mean-field ground state energy in the easy-plane regime** $E_0^{\mathrm{MF}}(\theta, \varphi)$, given by (4.2), divided by the anisotropy strength $(-B)$ for a fixed value of the coupling constant $\tilde{g}^2 = 0.01$. The small diagrams show the projection onto the unit sphere.

Specifically in the experimentally relevant regime $\mu \gg \alpha|\vec{M}|, \Delta_0$, we find

$$\begin{aligned} S = \int d\tau\, dy \Bigg[&\frac{1}{2}\bar{\chi}(v\not{\partial} + g\sin\theta\cos\varphi)\chi \\ &-iM(\partial_\tau\varphi)(1-\cos\theta) + \frac{A}{2}\left((\partial_y\theta)^2 + (\partial_y\varphi)^2\cos^2\theta\right) - \frac{B}{2}\cos^2\theta \Bigg], \end{aligned} \tag{4.1}$$

where the angles $(\theta(y), \varphi(y))$ parameterize the magnetization direction in spherical coordinates $\vec{m} = (\sin\theta\cos\varphi, \sin\theta\sin\varphi, \cos\theta)^T$. The effective fermionic velocity is given by $v \simeq \frac{\Delta_0^2}{\mu^2}\left|\cos(\mu W/v_F)\right| v_{\mathrm{F}}$ and the coupling constant by $g \simeq \alpha|\vec{M}|\frac{W}{v_{\mathrm{F}}/\Delta_0}$ (see Appendix A.1). The scalar anisotropy B in z-direction can here take on either positive values, corresponding to an easy-axis anisotropy, or negative values, leading instead to an easy-plane anisotropy.

4.2 Easy-plane anisotropy

In contrast to the case discussed in Chapter 3, in the following we are going to consider an easy-plane anisotropy with $B < 0$, before returning to the case $B > 0$ in Section 4.3.

One-dimensional ferromagnetic chains with a sufficiently large easy-plane anisotropy are known to be well described by an XY-type model [99]. If the continuous symmetry in the easy-plane is broken by means of a Zeeman field, the long-wavelength dynamics can be mapped to a sine-Gordon action for the azimuthal angle φ and the Zeeman field can thus induce a BKT transition [99, 100]. In the following, we will see that the Majorana-magnon interaction in our system plays a very similar role to such a Zeeman field by breaking the continuous symmetry and pinning the magnetization.

4.2.1 Mean-field theory

Integrating out the fermions from (4.1) and for now simply assuming θ and φ to be constant, one finds the mean-field ground state energy density E_0^{MF} to read

$$\frac{1}{v\Lambda^2} E_0^{\mathrm{MF}}(\theta, \varphi) = -\frac{\tilde{B}}{2}\cos^2\theta + \frac{\tilde{g}^2}{8\pi}\sin^2\theta\cos^2\varphi \left\{ \log\left(\frac{\tilde{g}^2}{4}\sin^2\theta\cos^2\varphi\right) - 1 \right\}, \tag{4.2}$$

where we introduced the dimensionless parameters $\tilde{B} = B/(v\Lambda^2)$ and $\tilde{g} = g/(v\Lambda)$. The resulting energy landscape for different values of $(-\tilde{B})$ and $\tilde{g}$ is plotted in Fig. 4.1.

For large values of $(-\tilde{B}) \gg \tilde{g}^2$, the first term in (4.2) dominates and the situation resembles the pure easy-plane picture one would expect: the energy is minimal for configurations with $\vec{m}$ in the x-y-plane, i.e. with $\theta = \pi/2$, and there is an approximate continuous symmetry regarding rotations around the z-axis, i.e. the energy does not depend on φ. This suggests the strong easy-plane case to correspond to a phase with φ fluctuating freely, while θ is fixed to $\pi/2$, i.e. a pure XY model. If in contrast $(-\tilde{B}) \ll \tilde{g}^2$, the interaction with the Majorana fermions dominates and leads to pronounced minima on the x-axis at $\varphi = 0$ and $\varphi = \pi$ (still with $\theta = \pi/2$). With regards to the action (4.1), this signals a fermionic gap opening with a spontaneous $\mathbb{Z}_2$ symmetry breaking akin to the strong easy-axis case discussed in Section 3.1. Note however, that there the mean field minima were exponentially close to each other, whereas here they lie on opposite ends of the unit sphere. In analogy to our earlier discussion, we then expect the stability against quantum fluctuations of this massive phase, emerging in the mean-field picture, to be dependent on sufficiently large values of the stiffnesses A and/or M. The less pronounced the minima, i.e. the larger $(-\tilde{B})$ compared to $\tilde{g}^2$, the larger the A- and M-values required for the stability become. If the stiffnesses are too small, the minima get smeared out and the system resides in a massless phase with free φ.

Note that we operate here and below under the assumption, that even the “small” stiffnesses are large enough to sufficiently suppress fluctuations in θ-direction, i.e. fluctuations out of the easy-plane, which is reasonable for a ferromagnet.

4.2.2 Effective theory near the easy-plane and RG analysis

In the strong easy-plane anisotropy case, $(-\tilde{B}) \gg \tilde{g}^2$, we saw that it is natural to limit the theory to the x-y-plane and only consider small fluctuations around it, $\theta \simeq \pi/2 + \delta\theta$ with $\delta\theta \ll 1$, as is reflected in the mean-field results in Fig. 4.1. Furthermore, the mean-field picture suggests that for the possible phase transition to a phase with massive fermions and the rotational φ-symmetry broken down to a spontaneously broken $\mathbb{Z}_2$-symmetry, only configurations in the x-y-plane are of importance as well. We therefore proceed by deriving an effective field theory valid in the vicinity of the x-y-plane (see Fig. 4.2).

Replacing $\theta = \pi/2 + \delta\theta$ in the action (4.1) and only keeping terms involving $\delta\theta$ up to Gaussian order, it follows

$$\begin{aligned} S \simeq -iM \int d\tau\, dy\, (\partial_\tau \varphi) + \int d\tau\, dy\, \Big[& \frac{v}{2}\bar{\chi}\partial\!\!\!/\chi + iM(\partial_\tau\varphi)\delta\theta \\ & + \frac{A}{2}\left((\partial_y\delta\theta)^2 + (\partial_y\varphi)^2\right) - \frac{B}{2}\delta\theta^2 + \frac{g}{2}\bar{\chi}\chi\cos\varphi \Big]. \end{aligned} \tag{4.3}$$

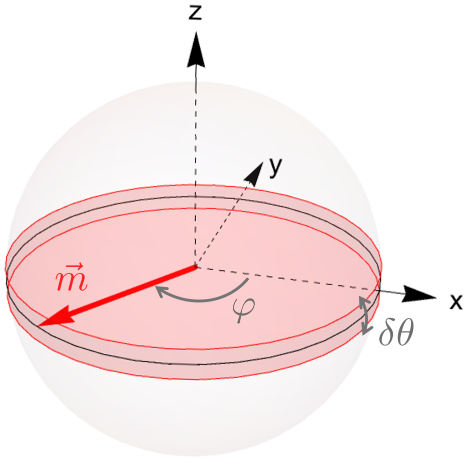

Figure 4.2: **Sketch of the magnetization direction on the unit sphere, illustrating the restriction of the theory to the vicinity of the easy-plane.** Only small values of $\delta\theta$ are taken into account, such that after integrating it out, an effective theory with the magnetization direction $\vec{m}$ being fully characterized by the azimuthal angle φ is obtained.

The first term is a theta term, which is trivial in the present case and can be omitted. Integrating out $\delta\theta$ yields

$$S = \int d\tau\, dy \left[\frac{v}{2}\bar{\chi}\not{\partial}\chi + \frac{g}{2}\bar{\chi}\chi\cos\varphi\right] + \frac{1}{2}\int \frac{d\omega\, dq}{(2\pi)^2}\varphi_{-q,-\omega}\left(\frac{M^2\omega^2}{A'q^2 - B} + Aq^2\right)\varphi_{q,\omega} \tag{4.4}$$

where $\varphi(y,\tau) = \int \frac{d\omega\, dq}{(2\pi)^2}\,\varphi_{q,\omega}e^{iqy-i\omega\tau}$ and we introduced the new parameter A', which microscopically equals A but scales differently under RG than the A already present. In particular, we find at tree-level $dA'/dl = -2A'$. A' is thus strongly irrelevant and will be omitted in the following. In Appendix B.2, we explicitly check that even if $A'\Lambda^2 \gg (-B)$ holds microscopically, the A'-term can safely be neglected from the outset without qualitatively altering the resulting phase diagrams.

Additionally, we will see that a $\cos 2\varphi$-term is generated under RG flow and the resulting effective theory can thus be written as

$$S = \int d\tau\, dy \left[\frac{v}{2}\bar{\chi}\not{\partial}\chi + \frac{1}{2}\left(\frac{1}{c}(\partial_\tau\phi)^2 + c(\partial_x\phi)^2\right) + u\cos 2\beta\phi + \frac{g}{2}\bar{\chi}\chi\cos\beta\phi\right]. \tag{4.5}$$

Here, we defined $\beta^2 = \sqrt{-B/(M^2A)}$, the effective bosonic velocity $c = \sqrt{-BA/M^2}$ and the rescaled field $\phi = \varphi/\beta$. Microscopically, $u = 0$.

This model is evocative of the supersymmetric sine-Gordon (SSG) model, which it corresponds to for $c = v$, $g^2 = -4\beta^2 u$ and $u < 0$. It is known that the SSG model always flows to a gapped phase [101], which can be checked to be consistent with Eqns. (4.7)-(4.9).

Employing a momentum-shell RG analysis, for which the details can be found in Appendix B.1, yields the flow equations (up to second order in $\tilde{u} = u/(v\Lambda^2)$ and $\tilde{g}$) below. They are valid as long as $\beta^2 > \pi/2$ and read

$$\frac{dc}{dl} = \frac{\beta^2 \tilde{g}^2}{16\pi v/c}\left(\frac{v^2}{c^2} - 1\right) c, \tag{4.6}$$

$$\frac{d\beta^2}{dl} = -2C_1 \frac{v^2}{c^2}\beta^6 \tilde{u}^2 - \frac{\beta^4 \tilde{g}^2}{8\pi v/c}, \tag{4.7}$$

$$\frac{d\tilde{u}}{dl} = 2\tilde{u}\left(1 - \frac{\beta^2}{2\pi}\right) - \frac{\tilde{g}^2}{8\pi}, \tag{4.8}$$

$$\frac{d\tilde{g}}{dl} = \tilde{g}\left(1 - \frac{\beta^2}{4\pi} - C_2 \frac{v}{c}\beta^2 \tilde{u}\right), \tag{4.9}$$

where $C_{1/2}$ are numerical constants. Similar flow equations for this type of model have been obtained in Ref. [102].

From Eq. (4.6) follows an emergent Lorentz symmetry. The flow of the remaining three parameters, starting in the $\tilde{u} = 0$-plane relevant for this problem, is shown in Fig. 4.3a. It exhibits the characteristics of a BKT transition: there is a line of fixed points on the β^2-axis, and a transition near $\beta^2 = 4\pi$, from a regime with the couplings running to zero (orange) to a strong coupling regime with $\tilde{g} \to \infty$ and $\tilde{u} \to -\infty$ (purple).

This corresponds to a phase transition from unbounded fluctuations of φ, being described by a free massless theory, to a massive phase with $\langle \varphi \rangle = 0$ or π, i.e. the magnetization being pinned to the x-axis, spontaneously breaking the inversion symmetry. An expectation value $\langle \varphi \rangle \neq \pm\pi/2$, and thus $\langle m_x \rangle \neq 0$, gaps out the Majorana fermions.

Plotting the resulting phase diagram in terms of the original parameters of the problem in Fig. 4.3b, reveals that the RG considerations confirm the mean-field picture: the larger the easy-plane anisotropy ($-B$), the larger the stiffnesses A and/or M need to be in order to stabilize the massive phase.

4.3 Easy-axis anisotropy

In Section 3.1, we examined the case of an easy-axis anisotropy $B > 0$ of such a magnitude, that only configurations of the magnetization with $m_x, m_y \ll 1$, i.e. near the z-axis, were of interest. For weaker easy-axis anisotropies, no such immediate simplifications of the problem are obvious. Still, in the following, we are going to attempt a generalization to weaker easy-axis anisotropies based on observations within mean-field theory: there, as we will see below, a regime can be identified in which an effective easy-plane is spanned by the easy-axis and the axis perpendicular to the junction, along which the interaction with the Majoranas takes place. This allows us, using similar arguments as above, to again postulate an effective field theory for which an RG analysis can be performed.

We would like to stress, however, that, compared to the previous section, the arguments that lead to the effective theory here are of rather conjectural character. Still, we interpret the consistency between the mean-field and RG results to be an indication of the merit of this approach as a step towards an understanding of the full phase diagram.

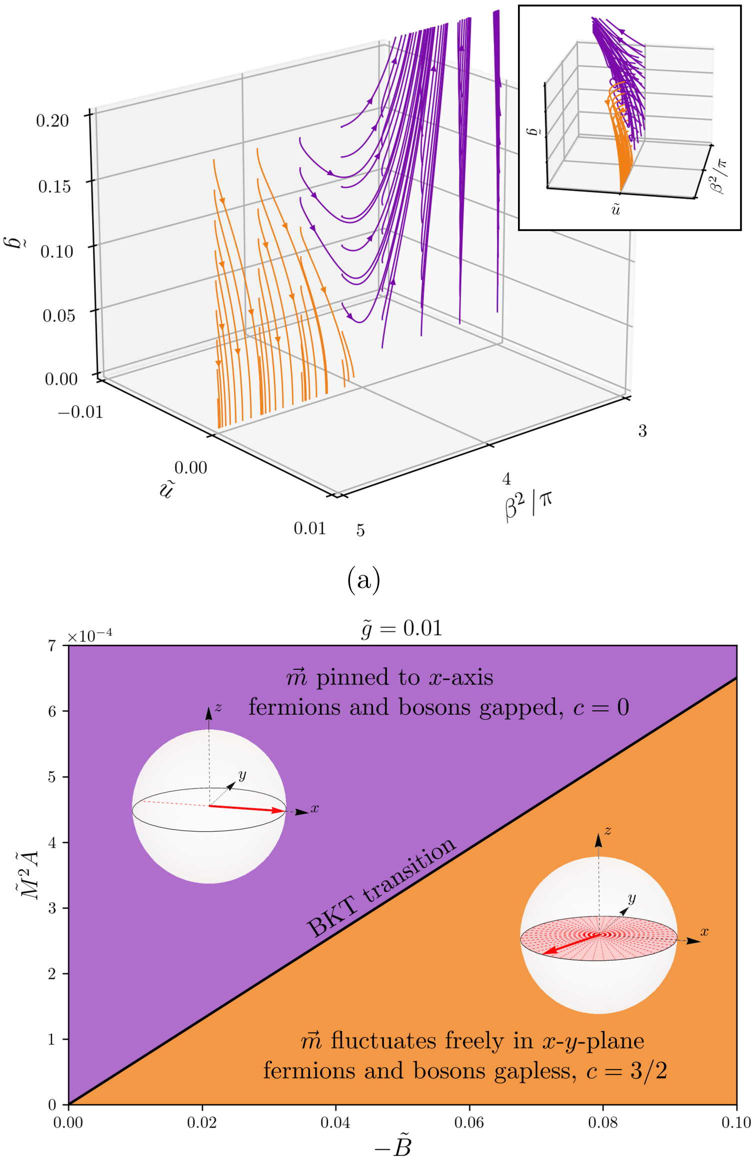

(a)

(b)

Figure 4.3: **Results from RG analysis of the easy-plane case.** (a) RG flow corresponding to Eqns. (4.7)-(4.9) starting in the $\tilde{u} = 0$-plane. The characteristic BKT flow with a transition from a regime with $\tilde{u}, \tilde{g} \to 0$ (orange) to a strong-coupling regime (purple) is evident. The inset shows the same diagram from a rotated perspective to make the flow towards negative $\tilde{u}$ visible. (b) Resulting phase diagram in terms of the original parameters at $\tilde{g} = 0.01$, showing increasing critical values of the stiffnesses for increasing anisotropy ($\tilde{A} = A/v, \tilde{M} = M/\Lambda$). The slope of the critical line diminishes when increasing the coupling constant $\tilde{g}$.

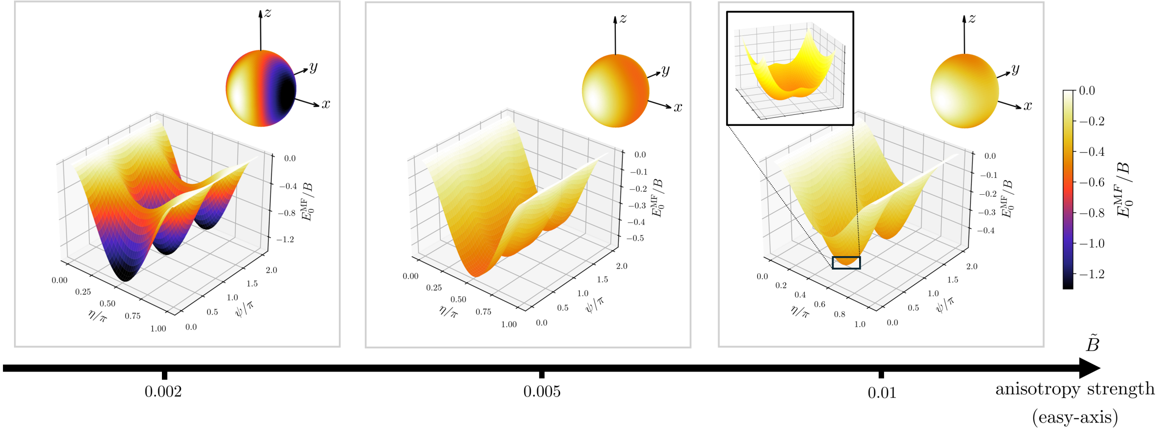

Figure 4.4: **Mean-field ground state energy in the easy-axis regime** $E_0^{\mathrm{MF}}(\eta,\psi)$ divided by the anisotropy strength B for a fixed value of the coupling constant $\tilde{g}^2 = 0.01$. The small diagrams show the projection onto the unit sphere.

4.3.1 Mean-field theory

In the easy-axis case $B > 0$, configurations with $\vec{m}$ pointing in z-direction will be important. In the parametrization we used until now, this is problematic, as φ is not well defined if $\theta = 0$ or π. Let us therefore introduce new angles (η,ψ) with which $\vec{m} = (\sin\eta\cos\psi, -\cos\eta, \sin\eta\sin\psi)^T$. The resulting mean-field ground state energy density is plotted in Fig. 4.4 for different values of $\tilde{B}$. Analogously to the easy-plane case, at weak anisotropies $\tilde{B} \ll \tilde{g}^2$ the interaction dominates and leads to minima near the x-axis, whereas at $\tilde{B} \gtrsim \tilde{g}^2$ the regime discussed in Section 3.1 with minima near the z-axis is recovered. For $\tilde{B} \sim \tilde{g}^2/2$, the system resides in a transitional regime between these two edge cases, as the minima, stemming respectively from interaction and anisotropy, merge. Remarkably, this results in an energy landscape which resembles an easy-plane anisotropy, as the energy is minimal and nearly degenerate for all ψ at $\eta = \pi/2$. Effectively, in this regime one can think of an easy-plane being spanned by the easy-axis-direction and the magnon-Majorana interaction. Mean-field theory thus suggests that here only configurations in the x-z-plane are of importance, as furthermore the energy barriers for fluctuations in η-direction are always larger than for the ones in ψ-direction. In analogy to our approach of the easy-plane case, we therefore suggest the low-energy physics to be reasonably well captured by an effective theory for ψ which is valid near $\eta = \pi/2$.

4.3.2 Effective theory near the emergent easy-plane and RG analysis

Motivated by mean-field theory, we thus only consider small fluctuations out of the x-z-plane and take $\eta \simeq \pi/2 + \delta\eta$ with $\delta\eta \ll 1$ (see Fig. 4.5). Once again, only keeping terms involving $\delta\eta$ up to Gaussian order, subsequently integrating out $\delta\eta$ and omitting the irrelevant A'-contribution, results in an action of the form (4.5),

$$S = \int d\tau\, dy \left[\frac{v}{2}\bar{\chi}\not{\partial}\chi + \frac{1}{2}\left(\frac{1}{c}(\partial_\tau\Psi)^2 + c(\partial_x\Psi)^2\right) + u\cos 2\beta\Psi + \frac{g}{2}\bar{\chi}\chi\cos\beta\Psi \right], \tag{4.10}$$

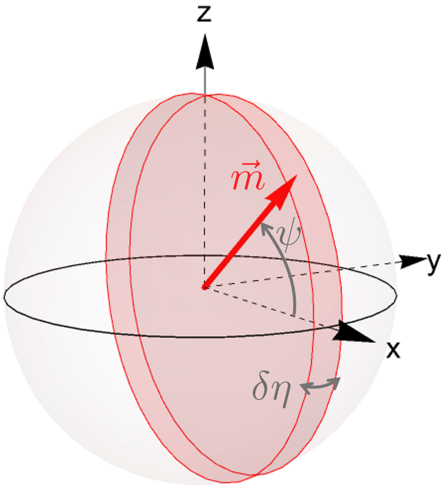

Figure 4.5: **Sketch of the magnetization direction on the unit sphere, illustrating the restriction of the theory to the vicinity of the emergent easy-plane with rotated spherical coordinates.** Only small values of $\delta\eta$ are taken into account, such that after integrating it out, an effective theory with the magnetization direction $\vec{m}$ being fully characterized by the new azimuthal angle ψ is obtained.

where now $\beta^2 = \sqrt{B/(2M^2A)}$, $c = \sqrt{AB/(2M^2)}$, $u = B/4$ and $\Psi = \psi/\beta$. Crucially, even though this is of course the same theory with the same flow equations (4.6)-(4.9) as in the easy-plane case, here $u \neq 0$ microscopically, which results in a more involved phase structure. Specifically, note that positive values of $\tilde{u}$ slow and may even revert the growth of $\tilde{g}$. If the initial value of $\tilde{u}$ is sufficiently large, the flow might lead into a different strong-coupling regime than the one above (which is still present here, of course), namely one with $\tilde{u} \to \infty$ and $\tilde{g} = 0$, see Fig. 4.6a. This would hint at $\langle\psi\rangle = \pm\pi/2$, i.e. the magnetization pointing in z-direction, corresponding to the regime with critical Majorana fermions discussed in Section 3.1. In between these two possible strong-coupling limits, $\tilde{u}$ and $\tilde{g}$ are growing in competition with each other. Rigorously differentiating between the strong-coupling regimes (green in Fig. 4.6a) is not possible in this framework, on account of the derived flow equations only being valid for $\beta^2 > \pi/2$ and the result of a weak-coupling expansion. Still, the BKT transitions near the β^2-axis are well controlled. This allows the identification of a massless phase (red), where $\tilde{u}, \tilde{g} \to 0$ with ψ fluctuating without bound.

Looking at the resulting phase diagram at fixed g in the M^2A-B-plane shows a non-monotonous behaviour of the critical value of the stiffnesses with a maximum at finite B (see Fig. 4.6b). This is in agreement with what can be expected from the mean-field picture: the energy landscape is the shallowest in the transitional regime between weak and strong anisotropy, which is why there the largest values for the stiffnesses are necessary in order to stabilize a phase with $\langle\psi\rangle \neq 0$.

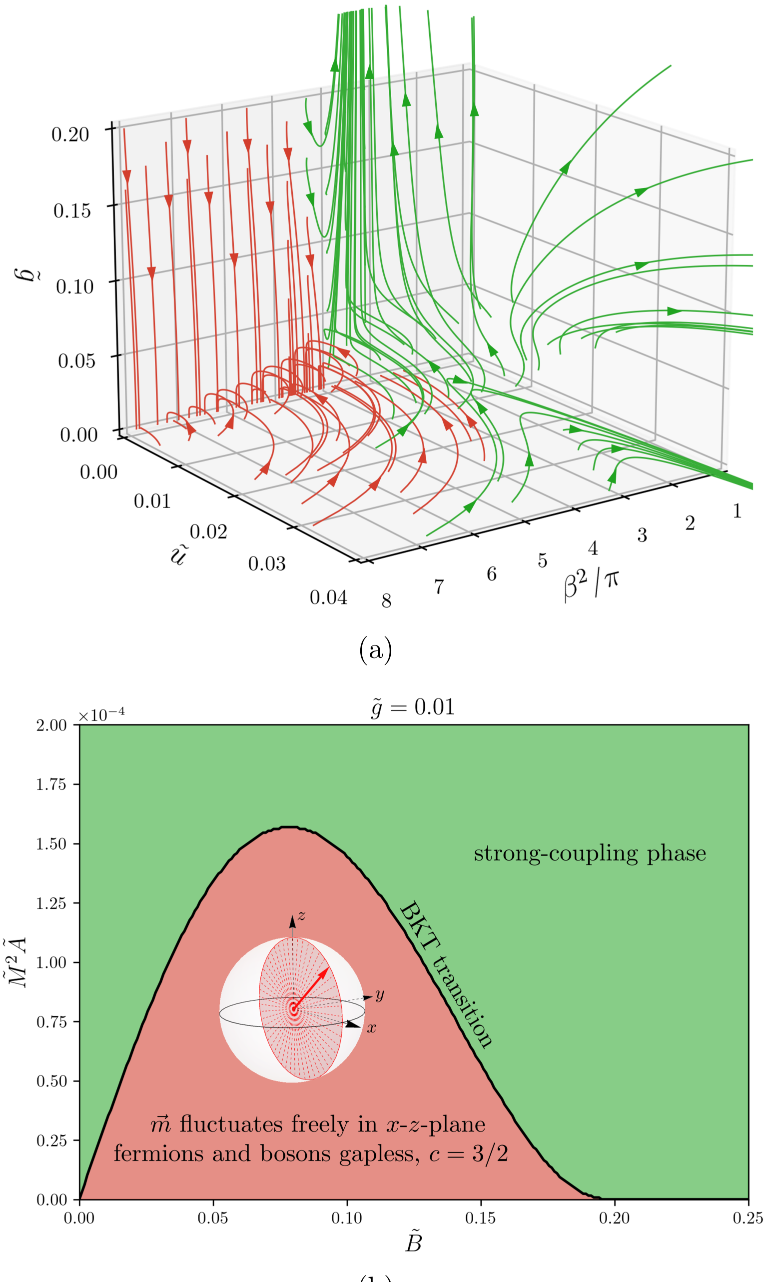

(b)

Figure 4.6: **Results from RG analysis of the easy-axis case.** (a) RG flow corresponding to Eqns. (4.7)-(4.9). As compared to Fig. 4.3a, an additional BKT transition to a different strong coupling regime ($\tilde{u} \to \infty, \tilde{g} \to 0$) emerges, most clearly visible in the vicinity of the $\tilde{g} = 0$-plane. The interpolation between the BKT transitions in the $\tilde{u} = 0$- and the $\tilde{g} = 0$-plane forms a critical surface, separating the different strong-coupling regimes (green) from the one with $\tilde{u}, \tilde{g} \to 0$ (red). (b) Resulting phase diagram in terms of the original parameters at $\tilde{g} = 0.01$, showing a non-monotonous behaviour of the critical values of the stiffnesses as a function of the anisotropy. This can be linked to the observation that in mean-field theory the energy landscape becomes shallowest and thus allows for the largest fluctuations at some finite value of B.

4.3.3 Experimental accessibility

Our analysis is primarily focused on qualitative aspects of the quantum phase structure of the given model. Still, for the sake of completeness, we proceed by roughly estimating the experimental accessibility of the identified relevant parameter regimes.

In Refs. [75, 76], evidence for magnetic exchange gaps $\alpha|\vec{M}|$ induced in TI surface states via covering with a ferromagnetic insulator as large as several tens meV has been provided. Assuming a superconducting gap corresponding to a few Kelvins as the high-energy cut-off $v\Lambda = \Delta_0 \sim 0.1 - 1\,\mathrm{meV}$, we thus see that the coupling constant $g \sim \alpha|\vec{M}|\frac{W}{\xi}$ can be on the order of the cut-off even for very conservative estimates of the magnetic exchange coupling and/or very narrow junctions. The small values of g/Δ_0, needed for our analysis to hold true, can therefore be presumed to be readily attainable.

In order to estimate the regions which are accessible in the $\tilde{M}^2\tilde{A}$-$\tilde{B}$-phase diagram with realistic materials, consider for example the 3D TI $\mathrm{Bi_2Se_3}$. Its surface states exhibit a Fermi energy of $\mu \simeq 300\,\mathrm{meV}$ and a Fermi velocity of $v_\mathrm{F} \simeq 400\,\mathrm{meV\,nm}$ [73, 74]. The corresponding superconducting coherence length is $\xi = v_\mathrm{F}/\Delta_0 \sim 400{-}4000\,\mathrm{nm}$. Values for the micromagnetic parameters of ferromagnetic insulators (see e.g. Refs. [103–107]) typically fall in the range of $A/(DW) \sim 10^{-12} - 10^{-11}\,\mathrm{Jm^{-1}}$ for the exchange stiffness, $B/(DW) \sim 10^3 - 10^6\,\mathrm{Jm^{-3}}$ for the scalar anisotropy constant as well as $|\vec{M}|/(DW) \sim 10^4 - 10^5\,\mathrm{Am^{-1}}$ for the saturation magnetization, which leads to a ratio between saturation magnetization and gyromagnetic ratio ($\gamma \sim 10^{11}\,\mathrm{s^{-1}T^{-1}}$) of $M/(DW) \sim 10^{27} - 10^{28}\hbar\,\mathrm{m^{-3}}$. Here, D is the thickness of the magnetic covering. The characteristic length scale over which the magnetization varies is given by the magnetic exchange length $l_\mathrm{ex} = \sqrt{2A/\mu_0|\vec{M}|^2} \sim 10 - 400\,\mathrm{nm}$. As indicated in the listed references, these properties are generally not purely material-specific, but depend on the geometry and temperature of the sample.

The values of the dimensionless parameters we are interested in are given by $\tilde{B} = vB/\Delta_0^2$ as well as $\tilde{M}^2\tilde{A} = vM^2A/\Delta_0^2$. They are thus proportional to $v \propto |\cos(\mu W/v_\mathrm{F})|$.

With the given estimates, we find experimentally viable parameters, depending on the width W and thickness D of the magnetic film, to read $\tilde{B} \simeq 10^{-5} - 10^{-2}\,\frac{DW}{\mathrm{nm}^2}|\cos(\mu W/v_F)|$, $\tilde{M}^2\tilde{A} \simeq 10^{-2} - 10^1\,\left(\frac{DW}{\mathrm{nm}^2}\right)^3|\cos(\mu W/v_F)|$. Consequently, due to the large stiffnesses naturally associated with ferromagnets, in order to roughly land in the region of the phase diagram that is examined in Fig. 4.6, a small cross sectional area with e.g. $D \sim W \sim 0.6 - 0.8\,\mathrm{nm}$ is necessary, which corresponds to few atomic layers in each direction. While typically the dimensions of magnetic thin films for applications like spintronics range from a few nanometers to a few micrometers, atomically thin layers exhibiting ferromagnetism have been succesfully realized in the past (see e.g. Refs. [107–110]). A reduction of the saturation magnetization, for example in diluted ferromagnets, would also allow for the parameters in larger, more readily available junction geometries to be found in the desired region. It can thus be said, that the predicted BKT transition likely resides at the boundary between current experimental capabilities and what are foreseeable advancements.

It is worth noting that generally a larger number of fermion flavors stabilizes the mean-field results, where an ordinary (complex) fermion can be understood as two (real) Majorana fermions. Therefore, if we considered a one-dimensional channel of “ordinary” instead of Majorana modes (e.g. quantum Hall edge states), this BKT transition would likely not be attainable in realistic systems, since in that case even smaller stiffnesses of the magnetization would be

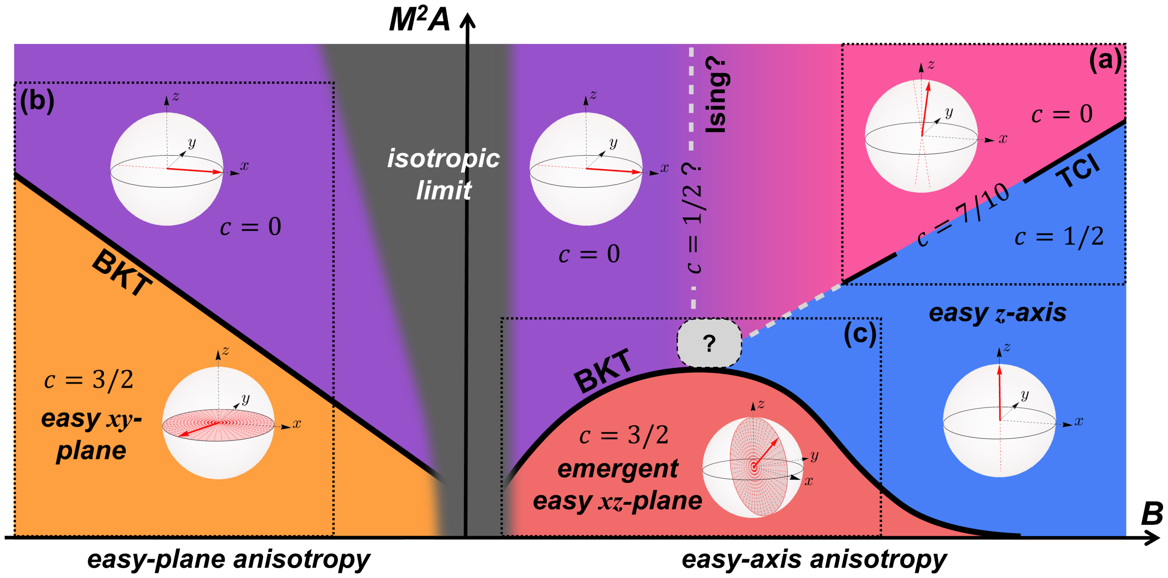

Figure 4.7: **Conjecture for the full phase diagram** at a fixed, finite g. The dotted boxes mark the areas for which we conducted an analysis in this work, the areas outside of that are a subject of speculation. The TCI transition in the dotted box (a) is discussed in Section 3.1, the BKT transitions in the dotted boxes (b) and (c) are analyzed and discussed in Sections 4.2 and 4.3, respectively. The (green) strong coupling phase of Fig. 4.6b for $B > 0$ is here comprised of the phases colored blue, pink and purple. The speculations of Section 4.4 furthermore lead us to expecting an Ising transition to take place between a phase with both x- and z-inversion symmetry spontaneously broken (pink) and one with x-inversion spontaneously broken (purple). The way in which the Ising and the TCI line connect to each other and/or the BKT line remains an open question. The isotropic limit $B \to 0$ (dark grey) is out of the scope of this work but likely characterized by strong fluctuations.

necessary to access it. It is the Majorana nature of the fermions that allows the transition to take place at higher values of $\tilde{M}$ and $\tilde{A}$.

In contrast, for the TCI transition at strong easy-axis anisotropies discussed in Section 3.1, consider the case where $\tilde{B} \sim \tilde{g} \sim 1$. With the estimates from the fluctuation analysis carried out there (assuming a ratio $\tilde{A}\tilde{B}/\tilde{M}^2 \sim 10^7$ in accordance with the experimentally relevant values), we find for this transition critical stiffnesses of $\tilde{M}^2\tilde{A} \sim 10^5$. According to our estimates above, this transition is thus accessible by devices with a more readily attainable magnetic cross-sectional area of $DW \sim 100\,\mathrm{nm}^2$.

4.4 Conjectured phase structure in strong-coupling regime and full phase diagram

As mentioned above, within our framework it is not possible to rigorously differentiate between the different strong-coupling phases which may emerge for $B > 0$. Let us here speculate about this part of the phase diagram, which is not accessible to our calculations, and subsequently present a conjecture for the full phase diagram, resulting from combining these speculations with our analysis in this work.

We expect three strong-coupling phases to exist for $B > 0$:

(i) one with the x-inversion symmetry spontaneously broken ($\langle m_x \rangle = \pm 1$, purple in Fig. 4.7),

(ii) one with z-inversion symmetry spontaneously broken ($\langle m_z \rangle = \pm 1$, blue in Fig. 4.7),

(iii) and one with both x- and z-inversion broken ($0 < |\langle m_x \rangle|, |\langle m_z \rangle| < 1$, pink in Fig. 4.7).

The latter two phases are the ones identified and discussed in Section 3.1, expected to be separated by a TCI transition. This claim can be further supported by noticing that the large B-limit corresponds to $\beta\Psi$ being restricted to small values in (4.10). Expanding the cosine terms for small arguments then yields the action of the Gross-Neveu-Yukawa model, for which a TCI transition has been theorized in Ref. [69].

In contrast, the transition between (i) and (iii) is one between two massive phases. It seems therefore most natural for it to belong to the Ising universality class with $c = 1/2$. This is supported by the fact that close to the x-axis, where this transition happens, i.e. at $\eta \simeq \pi/2$ and $\psi \simeq 0$ or π, integrating out the (massive) Majorana fermions, one arrives at an effective ϕ^4-theory.

The way in which the TCI and the Ising critical line connect to the BKT transition remains an open question to be investigated. A relation to the considerations in Ref. [111], where a supersymmetric multicritical point at the intersection of an Ising and a BKT transition is identified, seems very likely. A possible connection to such kind of a supersymmetric multicriticality is further supported by the similarity between the supersymmetric sine-Gordon model and the effective theory that arises here.

Together with the analysis and discussion presented in Sections 3.1, 4.2 and 4.3, we arrive at the conjectured phase diagram presented in Fig. 4.7.

4.5 Summary

Extending and generalizing the considerations on the topological superconductor-ferromagnet-superconductor junction of Chapter 3 to include arbitrary magnetic anisotropies, we here proposed this system as a platform for hosting 1+1-dimensional BKT transitions, in addition to the TCI phase transitions we found earlier.

In the case of an easy-plane anisotropy, such a BKT transition separates a massless phase, with unbounded fluctuations of the magnetization within the easy-plane, from a massive phase with gapped out Majorana fermions and the magnetization pinned to the axis perpendicular to the junction, spontaneously breaking a $\mathbb{Z}_2$ symmetry. The massive phase is, as before, stabilized by the spatial and temporal rigidity of the magnetic modes.

For the weak easy-axis anisotropy, the derivation of an effective theory is less straightforward than in the easy-plane and strong easy-axis case. Starting from mean-field considerations, we arrived at a conjecture for an effective low-energy theory based on an emerging effective easy-plane (oriented perpendicular to the propagation direction of the Majorana modes). Therein, we again identified a BKT transition separating a phase with unbounded fluctuations in the effective easy-plane from a strong-coupling regime with pinned magnetization, leading either to a phase with massive fermions or, if the magnetization is pinned to the easy-axis direction, a different phase with critical Majoranas. This pinning of the magnetization is again enabled by the magnetic stiffnesses dampening the fluctuations.

Finally, we presented a suggestion for the phase diagram of the topological SMS junction spanning all values of the magnetic anisotropy, based on mutually complementary mean-field and RG arguments. For the regions in parameter space not accessible within our framework, we provided speculative conjectures including a possible multicriticality.

5

Chapter 5

Limitations of the effective theory and emergence of additional zero modes

The results of the preceding chapters are based on an effective low-energy description of the topological Josephson junction in terms of two linearly dispersing one-dimensional Majorana modes. While this approach has proven to be extremely insightful, as for all approximations, one has to keep in mind its regime of applicability. In this chapter, we show that the effective theory breaks down at points where the effective velocity of the Majorana modes becomes too small. This is in contradiction to the naive expectation one might infer from the Fu-Kane logic, in which the effective velocity seems to appear as a perturbative correction. This failure of the description can be in part remedied by taking into account virtual processes involving the quasiparticle continuum. However, as we will come to see by means of an alternative approach, the points of zero effective velocity furthermore mark the emergence of additional low-energy modes, which do not appear in the effective theory, but have to be expected to contribute significantly to the physics of the junction.

The results of this chapter have been discussed and developed in collaboration with Kiryl Piasotski and Alexander Shnirman.

5.1 The low-energy approximation and its applications

The effective low-energy theory employed throughout this thesis and based on the groundbreaking insights by Fu and Kane [13, 41], in which the topological insulator Josephson junction is described by means of a 2×2 Hamiltonian in one spatial dimension, has in the past been utilized in a variety of works.

As a reminder, the main idea can be sketched as follows: starting from a 4×4 BdG Hamiltonian in the form of (3.1), describing two-dimensional TI surface states, a projection onto the 2×2 subspace of linearly dispersing one-dimensional Majorana modes is carried out, yielding the Hamiltonian

$$h_{\text{eff}} = -iv_{\text{eff}}\rho_x\partial_y + \varepsilon(y)\rho_z \tag{5.1}$$

with an effective velocity v_{eff}, where one operates under the assumption that the effective mass term $\varepsilon(y)$ only varies slowly with the coordinate y along the junction. ρ_i are here Pauli matrices acting in the low-energy subspace. The effective velocity arises as a correction from the p_y contribution of the original Hamiltonian, in which all parameters are initially treated as effectively y-independent.

Based on this description, experimental signatures of Majorana modes in the form of the (anomalous) Josephson current [25, 44], lifting of zeros in the Fraunhofer diffraction pattern [21, 45] as well as braiding operations [45, 112] have been examined.

Recently, the treatment has been generalized to more carefully take into account the y-dependence of the model parameters and thereby arrive at a Hamiltonian of the form

$$h_{\text{eff}} = -\frac{i}{2}\{v_{\text{eff}}(y), \partial_y\}\rho_x + \varepsilon(y)\rho_z, \tag{5.2}$$

involving an effective velocity $v_{\text{eff}} \to v_{\text{eff}}(y)$ which depends on the position along the junction as well. [113, 114] We are going to elaborate on its derivation in the next section. In Ref. [114], it has been proposed that this spatial dependence of v_{eff} in combination with irregularities of the fabricated junctions can explain the anomalous Josephson currents experimentally observed in Refs. [115, 116].

Note that the effective velocity is an oscillating quantity as a function of some system parameters like the chemical potential μ and the width of the junction W. E.g. in the experimentally relevant limit $\mu \gg \Delta_0$, Fu and Kane [13] found for the S-TI-S junction $v_{\text{eff}} \propto \cos(\mu W/v_F)$ with v_F the surface state Fermi velocity. In a similar calculation for ballistic graphene, Titov and Beenakker [117] obtained $v_{\text{eff}} \propto \sin(\mu_N W/v_F)$, where μ_N is the chemical potential in the non-superconducting region. Realistic systems thus might feature points at which the effective velocity vanishes, $v_{\text{eff}} \to 0$. In the following, we are going to examine such points and will come to the conclusion that the low-energy approximation fails in their vicinity. Crucially, in subsequent sections we will see that the occurrences of these points furthermore mark the emergence of additional low-energy degrees of freedom, reminiscent of a topological phase transition, which the effective theory does not capture either. Thus, we will be able to define a wide range of system parameters for which the frequently employed low-energy description is in fact not directly applicable.

5.2 'Black holes' and the breakdown of the low-energy approximation

5.2.1 Topological Josephson junction in a transverse magnetic field

Since we are here not interested in the additional complications stemming from a dynamic magnetization, we fix $\alpha\vec{M} = M\vec{e}_z$ in the Hamiltonian (3.1). Instead, we include a magnetic field $\vec{B} = \vec{\nabla} \times \vec{A}$ perpendicular to the TI surface into our considerations which induces a position-dependent phase difference $\varphi(y)$ (see Fig. 5.1). Additional y-dependencies, which we will not discuss here, might arise e.g. from irregularities of the width of the junction or the chemical potential [114]. This type of setup is of current experimental interest [115, 116] and has been theoretically proposed as a platform for creating and manipulating Majorana zero modes [44, 45]. These Majorana zero modes as well as low-energy Andreev states are localized at points y_n at which $\varphi(y_n) = (2n+1)\pi$, $n \in \mathbb{Z}$, in the center of Josephson vortices (see Section 2.2.2). They are known as Caroli-de Gennes-Matricon (CdGM) states. [118]

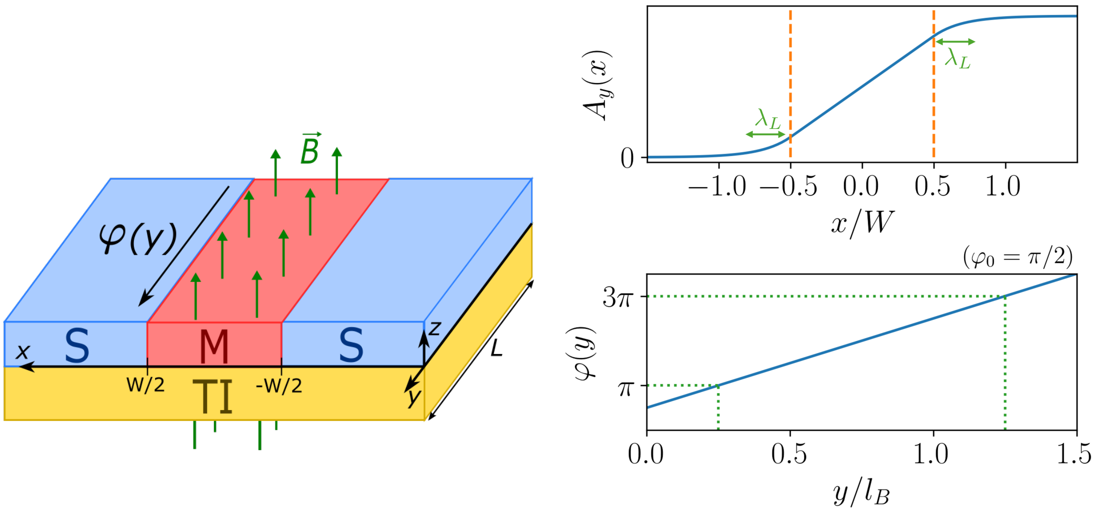

(a)

(b)

Figure 5.1: **SMS junction on the surface of a 3D TI in an external magnetic field.** a) Sketch of the system, where the green arrows indicate the magnetic field $\vec{B}$, while the magnetization is fixed to point in z-direction, $\vec{M} \propto \hat{e}_z$. b) Top: Sketch of the vector potential $A_y(x)$, as given in Eq. (5.5), which generates the magnetic field in z-direction. λ_L denotes the length scale over which the magnetic field penetrates into the superconductors while decaying exponentially, the London penetration depth. Bottom: The running phase difference $\varphi(y)$ along the junction resulting from the magnetic flux. The y-intercept is here chosen as $\varphi_0 = \pi/2$. Josephson vortices are centered at the points at which $\varphi = (2n+1)\pi$, indicated by the dotted lines, separated by one magnetic length l_B.

The corresponding BdG Hamiltonian reads

$$\begin{aligned} h(x,y) = \Big[&-iv_F\partial_x\sigma_x + \left(-iv_F\partial_y + \frac{ev_F}{c}A_y(x)\tau_z\right)\sigma_y - \mu(x)\Big]\tau_z \\ &+ M(x)\sigma_z + \Delta_0(x)\left(\cos\varphi(x,y)\tau_x + \sin\varphi(x,y)\tau_y\right) \end{aligned} \tag{5.3}$$

where

$$\begin{gathered} \Delta_0(x) = \Delta_0\,\theta(|x| - W/2), \qquad \varphi(x,y) = \varphi(y)\,\theta(x), \\ M(x) = M\,\theta(W/2 - |x|), \\ \mu(x) = \mu_N\,\theta(W/2 - |x|) + \mu_S\,\theta(|x| - W/2). \end{gathered} \tag{5.4}$$

To account for a possible renormalization of the chemical potential due to proximity to the metallic superconductors, we additionally allow μ to exhibit a step-like profile in x-direction. The orbital effects of the applied magnetic field are accounted for by the vector potential $\vec{A} = (0, A_y(x), 0)^T$ in Landau gauge, which, under the assumption of London screening with London penetration depth λ_L, is given by

$$\frac{e}{c}A_y(x) = \frac{\pi}{l_B W} \times \begin{cases} \lambda_L e^{(x+\frac{W}{2})/\lambda_L}, & x < -W/2, \\ \left(x + \frac{W}{2} + \lambda_L\right), & |x| \leq W/2, \\ \left(W + \lambda_L\left(2 - e^{-(x-\frac{W}{2})/\lambda_L}\right)\right), & x > W/2. \end{cases} \tag{5.5}$$

We introduced the magnetic length l_B, which is inversely proportional to the strength of the applied magnetic field. Under the assumption $l_B \ll \lambda_J$, where λ_J is the Josephson penetration depth of the junction, the phase difference then grows linearly

$$\varphi(y) = \frac{2\pi}{l_B}y + \varphi_0 \tag{5.6}$$

with some phase offset φ_0 and l_B is equal to the distance between two neighboring Josephson vortices.

5.2.2 Deriving the effective one-dimensional low-energy theory

In order to now give a sketch of the general approach with which to obtain the effective low-energy theory, consider first some generic 2D BdG Hamiltonian which can be separated into two Hamiltonians h_0 and h_1 of the form,

$$h(x,y) = h_0(x, \vec{R}_0(y)) + h_1(y, \vec{R}_1(x)), \tag{5.7}$$

such that h_0 only parametrically depends on y via some quantities collected in $\vec{R}_0$, and accordingly for h_1. For definiteness, since this is the form which is of interest to us, let us take $h_0 = -iv_F\tau_z\sigma_x\partial_x + \vec{R}_0(y)\cdot\vec{T}$ and $h_1 = -iv_F\tau_z\sigma_y\partial_y + \vec{R}_1(x)\cdot\vec{T}$, where $\vec{T} = (\tau_0\sigma_0, \tau_0\sigma_x, \ldots, \tau_z\sigma_z)^T$. If we are then able to find the solutions to

$$h_0(x, \vec{R}_0(y))\xi_n(x, \vec{R}_0(y)) = \varepsilon_n(\vec{R}_0(y))\xi_n(x, \vec{R}_0(y)) \tag{5.8}$$

for each y (where due to particle-hole symmetry we can arrange the solutions such that $\varepsilon_n = -\varepsilon_{-n}$), we may make the ansatz

$$\psi(x,y) = \sum_n \alpha_n(y)\xi_n(x, \vec{R}_0(y)) \tag{5.9}$$

for the solution to the full problem $(h_0 + h_1)\psi = E\psi$. This can be understood as 'gluing' together of one-dimensional slices at fixed y in a way dictated by h_1. Since $\{\xi_n(x, \vec{R}_0(y))\}$ form a complete basis for every y, this is an exact procedure. The corresponding effective Hamiltonian acting on $\alpha_n(y)$ follows to be

$$h_{\text{eff}}^{(m,n)}(y) = -iv_F \langle m|\tau_z\sigma_y|n\rangle \partial_y - iv_F \langle m|\tau_z\sigma_y|\partial_y n\rangle + \langle m|\vec{R}_1(x)\cdot\vec{T}|n\rangle + \varepsilon_n(\vec{R}_0(y))\delta_{m,n}, \tag{5.10}$$

where $\langle\cdot|\cdot|\cdot\rangle$ only entails integration over x and $\langle x|n\rangle = \xi_n(x, \vec{R}_0(y))$.

Rewriting

$$\langle m|\tau_z\sigma_y|\partial_y n\rangle = \frac{1}{2}\partial_y \langle m|\tau_z\sigma_y|n\rangle + \frac{1}{2}\Big(\langle m|\tau_z\sigma_y|\partial_y n\rangle - \langle \partial_y m|\tau_z\sigma_y|n\rangle\Big), \tag{5.11}$$

it follows

$$h_{\text{eff}}^{(m,n)}(y) = -\frac{1}{2}\big\{v_{mn}(y), i\partial_y\big\} - \frac{1}{2}B_{mn}(y) + \langle m|\vec{R}_1(x)\cdot\vec{T}|n\rangle + \varepsilon_n(\vec{R}_0(y))\delta_{m,n}, \tag{5.12}$$

where we defined

$$v_{mn}(y) := v_F \langle m|\tau_z\sigma_y|n\rangle, \quad B_{mn}(y) := iv_F\Big(\langle m|\tau_z\sigma_y|\partial_y n\rangle - \langle \partial_y m|\tau_z\sigma_y|n\rangle\Big). \tag{5.13}$$

Consider now a situation in which the spectrum of h_0 for each value of y can be separated into $2N$ low-energy solutions with $\varepsilon_{|n|\leq N} < \Delta_0$ separated from the rest of the spectrum $\varepsilon_{|n|>N} \geq \Delta_0$ by a finite energy gap. If then $E \ll \Delta_0$, it seems reasonable to assume that the full solution can be well approximated by

$$\psi(x,y) \approx \sum_{|n|\leq N} \alpha_n(y)\xi_n(x, \vec{R}_0(y)). \tag{5.14}$$

If there are only two branches of states in the gap (connected by particle-hole symmetry), as is the case in all our considerations of the previous chapters, one thus obtains an effective 2×2-Hamiltonian which is only dependent on y.

5.2.3 Application to the topological Josephson junction

Following the procedure outlined in the previous section, we separate the Hamiltonian (5.3) into two parts $h = h_0 + h_1$, where we take $h_1 = -iv_F\tau_z\sigma_y\partial_y + \frac{ev_F}{c}A_y(x)\sigma_y$. $h_0 = -iv_F\partial_x\sigma_x\tau_z - \mu(x)\tau_z + M(x)\sigma_z + \Delta_0(x)\left(\cos\varphi(x,y)\tau_x + \sin\varphi(x,y)\tau_y\right)$ then only depends on y parametrically through $\varphi(y)$ and the corresponding eigenvalue equation can be solved for each value of φ. We find that the bound state spectrum of h_0 with eigenenergies $|\varepsilon(\varphi)| < \Delta_0$ is determined by the solutions to the transcendental equation

$$\begin{aligned}\cos\varphi = {} & M^2 s_+ s_- + (2\varepsilon^2/\Delta_0^2 - 1)\left[c_+c_- + (\mu_N^2 - \varepsilon^2)s_+s_-\right] \\ & + 2\varepsilon/\Delta_0\sqrt{1-\varepsilon^2/\Delta_0^2}\left[(\varepsilon+\mu_N)s_+c_- + (\varepsilon-\mu_N)s_-c_+\right],\end{aligned} \tag{5.15}$$

where

$$c_\pm = \cos\left(\sqrt{(\varepsilon \pm \mu_N)^2 - M^2}\, W/\xi\right), \quad s_\pm = \frac{\sin\left(\sqrt{(\varepsilon \pm \mu_N)^2 - M^2}\, W/\xi\right)}{\sqrt{(\varepsilon \pm \mu_N)^2 - M^2}} \tag{5.16}$$

with the superconducting coherence length $\xi = v_F/\Delta_0$.

Note that the spectrum is independent of the chemical potential μ_S in the superconducting regions. If $M = 0$, it can be checked that the solutions to (5.15) are independent of μ_N as well [114]. Examples for the resulting spectrum are shown in Fig. 5.2 and correspond to the results found in Ref. [119]. As noted there, for an increasing width W more branches of bound states appear, which are degenerate at $\varphi = n\pi$, $n \in \mathbb{Z}$, for $M = 0$ (Kramers degeneracy) and eventually merge with the continuum states ($|\varepsilon| \geq \Delta_0$). Finite M breaks time-reversal symmetry and thus can lift all of the degeneracies (apart from the crossing at $\varepsilon = 0$ for $\varphi = \pi$ which is protected by conservation of fermion parity [119]). By tuning the parameters, we can thus find regimes in which only two branches are present in the gap and well separated from the continuum for all φ. This corresponds to our basic approach so far in this thesis and to the case $N = 1$ in the approximation (5.14). This situation will here continue to be our focus.

Let us label the two relevant states by $\sigma = \pm 1$. The effective Hamiltonian in the low-energy subspace, following from Eq. (5.12), then is given by

$$h_{\text{eff}}^{(\sigma,\sigma')} = -\frac{1}{2}\{v_{\sigma,\sigma'}(y), i\partial_y\} - \frac{1}{2}B_{\sigma,\sigma'}(y) + \frac{ev_F}{c}\langle\sigma|A_y(x)\sigma_y|\sigma'\rangle + \varepsilon_n(\varphi(y))\delta_{\sigma,\sigma'}. \tag{5.17}$$

The diagonal components of the effective velocity vanish

$$v_{\sigma,\sigma} = v_F \langle\sigma|\tau_z\sigma_y|\sigma\rangle = 0, \tag{5.18}$$

which follows from an x-inversion symmetry as shown in Appendix C.1.2. We may thus express the effective velocity as

$$v_{\sigma,\sigma'} \equiv v_{\text{eff}}^x(\varphi(y))\,\rho_x^{\sigma,\sigma'} + v_{\text{eff}}^y(\varphi(y))\,\rho_y^{\sigma,\sigma'}, \tag{5.19}$$

where ρ_i are Pauli matrices. By performing the gauge transformation

$$\xi_\sigma \to \xi_\sigma e^{i\sigma\chi(y)/2}, \quad \text{such that} \quad \langle\xi_\sigma|\tau_z\sigma_y|\xi_{\sigma'}\rangle \in \mathbb{R}, \tag{5.20}$$

we eliminate v_{eff}^y and can thus define the effective velocity as $v_{\text{eff}} \equiv v_{\text{eff}}^x$. Note that this gauge transformation generates no additional contributions to $B_{\sigma,\sigma'}$ since

$$\begin{aligned}\langle\sigma|\tau_z\sigma_y|\partial_y\sigma'\rangle - \langle\partial_y\sigma|\tau_z\sigma_y|\sigma'\rangle \quad &\to \quad e^{-i(\sigma-\sigma')\chi/2}\left(\langle\sigma|\tau_z\sigma_y|\partial_y\sigma'\rangle - \langle\partial_y\sigma|\tau_z\sigma_y|\sigma'\rangle\right) \\ &+ \frac{i}{2}\,[\partial_y\chi]\,\underbrace{(\sigma+\sigma')}_{=0 \text{ if } \sigma\neq\sigma'}\,e^{-i(\sigma-\sigma')\chi/2}\,\underbrace{\langle\sigma|\tau_z\sigma_y|\sigma'\rangle}_{=0 \text{ if } \sigma=\sigma'}.\end{aligned} \tag{5.21}$$

From particle-hole symmetry follows furthermore (see Appendix C.1.1)

$$\langle\sigma|\tau_z\sigma_y|\partial_y\sigma'\rangle = \langle\partial_y(-\sigma')|\tau_z\sigma_y|(-\sigma)\rangle\,, \tag{5.22}$$

which allows us to write

$$B_{\sigma,\sigma'}(y) = B_z(y)\rho_z^{\sigma,\sigma'}. \tag{5.23}$$

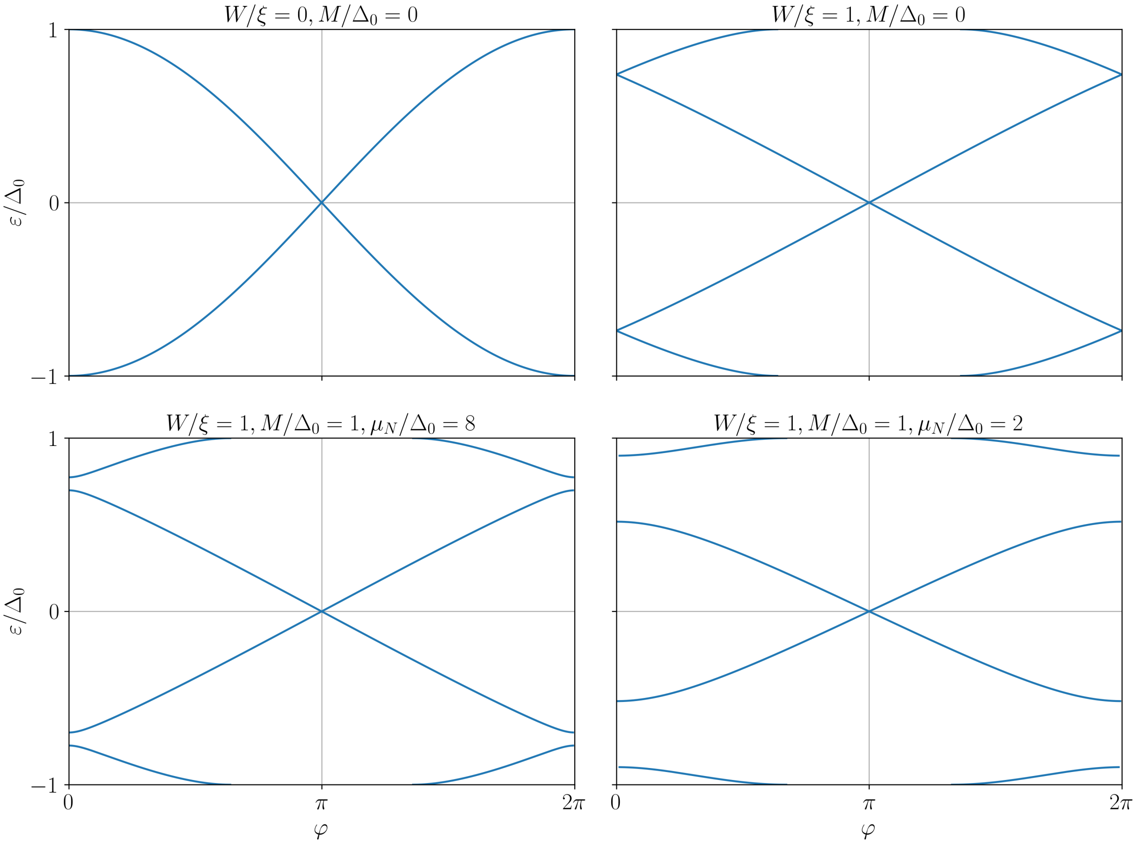

Figure 5.2: **Examples for the bound state spectrum** of the (transverse) Hamiltonian h_0 as a function of φ for the parameters given in each panel, determined from Eq. (5.15). If $M = 0$, the spectrum is independent of μ_N.

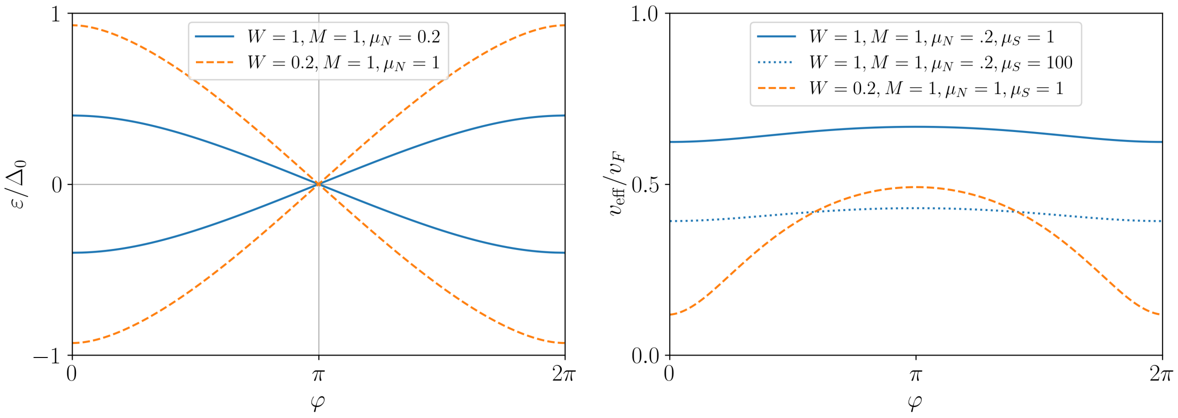

Figure 5.3: **Examples for the effective velocity** shown on the right-hand side as a function of φ in the case of only two branches of bound states present in the gap (left-hand side). Here and in the following, unless specified otherwise, lengths are measured in units of the superconducting coherence length ξ, and energies in units of Δ_0.

Once again from particle-hole symmetry (Appendix C.1) follows finally that $\langle \sigma | \sigma_y | -\sigma \rangle = 0$, such that, defining

$$\frac{ev_F}{c} \langle \sigma | A_y(x) \sigma_y | \sigma' \rangle \equiv \rho_z^{\sigma,\sigma'} \tilde{A}(y), \tag{5.24}$$

we arrive at an effective Hamiltonian of the form

$$h_{\rm eff} = -\frac{1}{2} \big\{ v_{\rm eff}(y),\, i\partial_y \big\} \rho_x + \big(\varepsilon(y) + B_z(y) + \tilde{A}(y) \big)\, \rho_z \tag{5.25}$$

with $\varepsilon \equiv \varepsilon_+$.

5.2.4 Zeros of the effective velocity as black hole-analogues

As mentioned above, in contrast to the effective Hamiltonian (A.4) which we employed in the preceding chapters, within this approach the effective velocity of the one-dimensional modes obtains a y-dependence, while previously we approximated $v = v_{\rm eff}(\varphi = \pi)$. An explicit expression for $v_{\rm eff}(y)$ for the case $M = 0$ is provided in Ref. [114].

In Fig. 5.3, we show some examples of the effective velocity as a function of the phase difference together with the corresponding spectra (remember that $\varphi \propto y$). $v_{\rm eff}$ is symmetric with respect to $\varphi = \pi$ and displays local extrema at φ equal to mutiples of π, while the magnitude and the amount of variation is dependent on the parameters.

For specific parameter combinations, there exist values of φ for which $v_{\rm eff} = 0$. These special points may occur at arbitrary φ (but always symmetric with respect to π). In Fig. 5.4 we show an example of this by tuning μ_S, which has no effect on the spectrum.

Let us have a closer look at the vicinity of these zero-velocity points. To this end, we take $v_{\rm eff}(y) \approx ay$ with some slope a, while we assume $\varepsilon(y) + B_z(y) + \tilde{A}(y) \simeq \varepsilon_0$ to be approximately constant. We then find

$$h_{\rm eff}^2 = -a^2 y^2 \partial_y^2 - 2a^2 y \partial_y + (\varepsilon_0^2 - a^2/4). \tag{5.26}$$

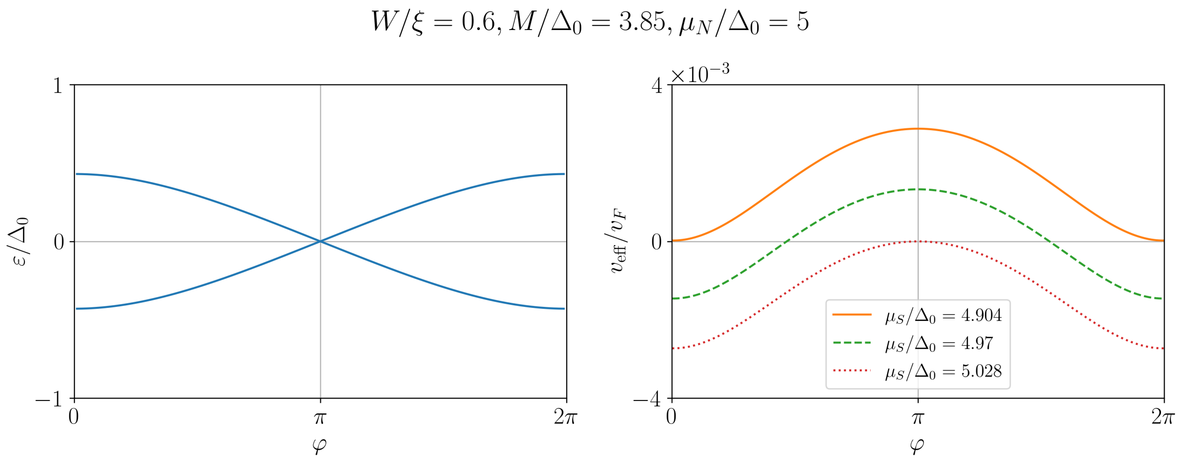

Figure 5.4: **Examples for the effective velocity crossing zero** at different values of φ shown on the right, for parameters indicated above the figure and corresponding to the bound-state spectrum given on the left.

The general solution to $h_{\text{eff}}^2\psi = E^2\psi$ (which can be found by means of the Frobenius method [120]) reads

$$\psi(y) = c_1 y^{-\frac{1}{2}-\sqrt{\varepsilon_0^2-E^2}/a} + c_2 y^{-\frac{1}{2}+\sqrt{\varepsilon_0^2-E^2}/a}. \tag{5.27}$$

A solution which is normalizable thus only exists as long as $E^2 < \varepsilon_0^2$, with the wave function diverging at $y = 0$ if $E^2 < \varepsilon_0^2 - a^2/4$ is not met.

It has been pointed out [121] that the Hamiltonian (5.25) can in fact be mapped to a Dirac Hamiltonian in a 1+1 dimensional curved space-time with a spatially varying mass $m(y) \sim \varepsilon(y)/v_{\text{eff}}(y)$ and metric $ds^2 = v_{\text{eff}}^2(y)dt^2 - dy^2$. The points at which the effective velocity vanishes $v_{\text{eff}}(y) = 0$ then correspond to the event horizons of Schwarzschild black holes, effectively slicing the system into two ‘universes’ between which no information can be passed [122]. This singularity ensues the observed divergences of the wave functions.

These peculiar results, in particular the absence of normalizable solutions for $E^2 \geq \varepsilon_0^2$, hint at a breakdown of the employed approximations and can be attributed to the step of strictly limiting the theory to the low-energy subspace via Eq. (5.14). Naively, one might expect that with only two, well separated branches in the gap, the approximation becomes increasingly accurate as the ‘correction’ induced by h_1, in form of the effective velocity, diminishes. We see here that this line of reasoning is flawed.

To build intuition and illustrate that $v_{\text{eff}} \to 0$ indeed corresponds to instances where the two-level approximation fails, consider the case without any y-dependence. In this setting, Eq. (5.25) reduces to a simple Dirac Hamiltonian with dispersion $E^2 = v_{\text{eff}}^2 k^2 + \varepsilon^2$. Now, as v_{eff} goes to zero and we look for solutions with $E \neq \varepsilon$, arbitrarily large values of k become important. But since $h_1 \propto k$, the matrix elements of h_1 connecting the low- and high-energy subspaces also necessarily grow large and thus can no longer be neglected. Taking them into account adds a correction to the dispersion which then reconciles the necessity of large k, effectively imposing a cut-off.

In order to proceed, we can thus either include the higher-order effects in the low-energy approximation or add an explicit upper cut-off to k. In the following, we examine the first option. We will see that the higher-order corrections indeed regularize the ‘black hole’-like behavior and reproduce some of the features that emerge through an alternative method discussed in the subsequent section.

5.2.5 Second-order corrections to the low-energy theory

Let us go back to the eigenvalue equation for the (exact) expression in Eq. (5.10), ignoring for now the vector potential $A_y(x)$ for simplicity

$$\sum_n \left[-iv_{mn}(y)\partial_y - \tilde{B}_{mn}(y)\right]\alpha_n(y) = (E-\varepsilon_m(y))\alpha_m(y), \tag{5.28}$$

where we defined $\tilde{B}_{mn} \equiv iv_F \langle m|\tau_z\sigma_y|\partial_y n\rangle$. Remember that $v_{nn}=0$ due to the x-inversion symmetry (see Appendix C.1.2). The logic of our original two-level approximation works as follows: if the left-hand side, i.e. the contributions from h_1, are zero, the low-energy solutions read $E=\varepsilon_+$ with $\alpha_1=1$, $\alpha_{n\neq 1}=0$, and $E=\varepsilon_-=-\varepsilon_+$ with $\alpha_{-1}=1$, $\alpha_{n\neq -1}=0$. Then, we assume the corrections induced by h_1 to be small, and therefore the eigenstates to still have $\alpha_{n\neq\pm 1}\approx 0$, such that in the sum on the left-hand side we only have to take into account $n=\pm 1$.

In other words, rewriting Eq. (5.28) as

$$\begin{aligned}\Big[-iv_{\text{eff}}(y)\partial_y - \tilde{B}_{\sigma,-\sigma}(y)\Big]\alpha_{-\sigma}(y) - \Big[E-\varepsilon_\sigma(y)+\tilde{B}_{\sigma\sigma}(y)\Big]\alpha_\sigma(y)&\\ = -\sum_{n\neq\pm 1}\Big[-iv_{\sigma n}(y)\partial_y - \tilde{B}_{\sigma n}(y)\Big]\alpha_n(y)&\end{aligned} \tag{5.29}$$

with $\sigma=\pm 1$, we neglected the right-hand side of the equation since we assumed $\alpha_{n\neq\pm 1}\approx 0$ for $E\sim\varepsilon_\sigma$.

In the following, we instead effectively integrate out the higher-energy contributions to take into account their higher-order effects on the low-energy subspace. To this end, one can rearrange Eq. (5.28)

$$\alpha_m(y) = \frac{1}{E-\varepsilon_m(y)+\tilde{B}_{mm}(y)}\sum_{n\neq m}\left[-iv_{mn}(y)\partial_y - \tilde{B}_{mn}(y)\right]\alpha_n(y) \tag{5.30}$$

and iteratively plug this into the right-hand side of Eq. (5.29) (cf. Brillouin-Wigner perturbation theory). In Appendix C.2, we carry this procedure out up to second-order and obtain an effective Hamiltonian of the form

$$\begin{aligned}h_{\text{eff}}^{(\text{corr})} =& -\partial_y\left(\mathcal{A}(y)\partial_y\right)\rho_z + \left(\varepsilon(y)+\mathcal{B}(y)\right)\rho_z\\ &-\frac{1}{2}\left\{i\partial_y, v_{\text{eff}}(y)+\delta\tilde{v}_x(y)\right\}\rho_x - \frac{1}{2}\left\{i\partial_y,\delta\tilde{v}_y(y)\right\}\rho_y - \frac{1}{2}\left\{i\partial_y,\delta\tilde{v}_0(y)\right\}\rho_0.\end{aligned} \tag{5.31}$$

Most notably, disregarding the details of the individual parameters, in comparison to (5.25) a term $\sim\partial_y^2$ is generated, such that the Dirac nature of the Hamiltonian is lost, the dispersion becomes quadratic. Thus, if the leading contribution v_{eff} becomes comparable to the presumably small corrections, the associated differential equation is governed by a higher-order

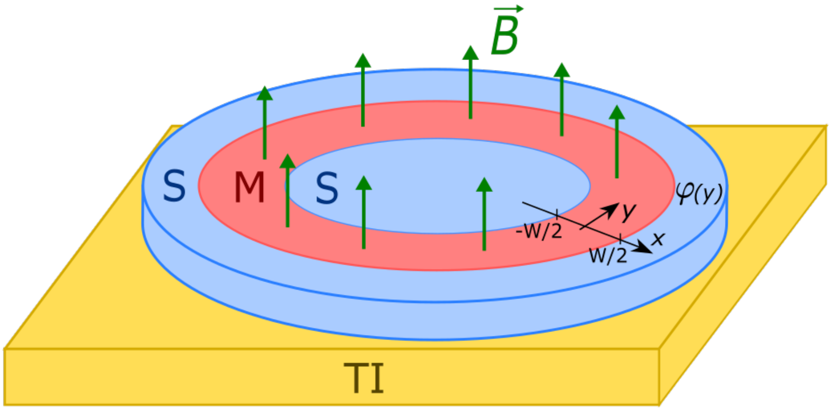

Figure 5.5: **SMS junction on the surface of a 3D TI in an external magnetic field**, as depicted in Fig. 5.1, closed into a Corbino ring geometry such that y and $y + L$ correspond to the same point along the junction. The gauge is chosen such that the phase of the inner superconductor is 0 while the phase of the outer superconducting ring is given by $\varphi(y)$.

derivative. The singular behavior we obtained above is thereby regularized, but the shape of the CdGM modes is to be expected to be altered (compared to the usual simple Gaussian form of the zero-energy state).

As mentioned earlier, although the 'black hole'-anomaly is thus no longer an issue, in the following we are going to see that the effective theory still inherently misses an important aspect of the low-energy physics of the system.

5.3 Spectral matrix

Having encountered the limitations of the effective theory, we would like to pursue a different approach, which does not rely on a limitation to a specific low-energy subspace but instead entails an upper cut-off to the momentum k in y-direction. Expanding in Fourier modes $\sim e^{iky}$, we are going to define the infinite-dimensional spectral matrix $M_{k,k'}(E)$, with entries that are relatively easily found and the zero-modes of which represent solutions to our problem.

5.3.1 Corbino geometry and expansion in Fourier modes

While the expansion in transverse eigenmodes (5.9) is a procedure that is local in y, in the following the boundary conditions will be of immediate significance. In order to gain a physically clear picture, we are going to consider closing the Josephson junction into a Corbino ring geometry such that the system becomes periodic in y (see Fig. 5.5). Consequently, the magnetic flux through the junction can only take on values corresponding to integer multiples of the flux quantum, such that the length of the system L is a multiple of the magnetic length l_B, $L = nl_B$ with $n \in \mathbb{N}$, which ensures the single-valuedness of φ (mod 2π) at each point y. n then corresponds to the number of flux quanta in the junction as well as to the number of Josephson vortices (separated by one magnetic length from each other). For the sake of simplicity, we are going to assume a perfectly screened magnetic field and set the London penetration depth to zero, $\lambda_L = 0$. We expect the presented results to qualitatively hold true for small but non-zero λ_L as well.

Furthermore, we take advantage of the fact that the unitary transformation $U(\varphi) := e^{-i\varphi\tau_z/2}$ satisfies

$$U(\varphi)\tau_x U^{-1}(\varphi) = \cos\varphi\,\tau_x + \sin\varphi\,\tau_y. \tag{5.32}$$

Consider then a complete basis of momentum eigenfunctions in y-direction

$$\langle y|k_\ell\rangle = \frac{1}{\sqrt{L}}e^{ik_\ell y/L}, \qquad \sum_{l=-\infty}^{\infty}|k_\ell\rangle\langle k_\ell| = 1, \quad \langle k_\ell|k_{\ell'}\rangle = \delta_{\ell,\ell'}, \tag{5.33}$$

where to enforce periodic boundary conditions corresponding to the Corbino geometry, one chooses

$$k_\ell = 2\pi\ell. \tag{5.34}$$

In this basis, the Hamiltonian (5.3) reads

$$\begin{aligned} h_{\ell,\ell'} := \langle k_\ell|h|k_{\ell'}\rangle = \delta_{\ell,\ell'}\Big\{\big[-iv_F\partial_x\sigma_x + \left(\frac{v_F k_\ell}{L} + \frac{ev_F}{c}A_y(x)\tau_z\right)\sigma_y - \mu(x)\big]\tau_z + M(x)\sigma_z \\ + \theta(-x-W/2)\Delta_0\tau_x\Big\} + \theta(x-W/2)\Delta_0\sum_p U_{\ell p}\tau_x U^\dagger_{p\ell'} \end{aligned} \tag{5.35}$$

and the energy eigenvalue equation can be written as $\sum_{\ell'} h_{\ell\ell'}(x)\psi_{\ell'}(x) = E\psi_\ell(x)$.

5.3.2 Matching conditions

In each region, i.e. $x < -W/2$ (L) , $|x| < W/2$ (M), $x > W/2$ (R), we can explicitly find the linearly independent solutions to the respective eigenvalue equation. Since we are interested in Andreev bound states with $|E| < \Delta_0$, in the left and right region we choose only those two out of four that are zero at minus/plus infinity, respectively. The general solutions then are given by linear combinations of those

$$\psi_{L,\ell}(x;E) = \left(\psi^{(1)}_{L,\ell}(x;E), \psi^{(2)}_{L,\ell}(x;E)\right)\begin{pmatrix} c^{(1)}_{L,\ell}(E) \\ c^{(2)}_{L,\ell}(E)\end{pmatrix} \equiv \Psi_{L,\ell}(x;E)C_{L,\ell}(E), \tag{5.36}$$

$$\begin{aligned} \psi_{R,\ell}(x;E) = \sum_{\ell'} U_{\ell,\ell'}\left(\psi^{(1)}_{R,\ell'}(x;E), \psi^{(2)}_{R,\ell'}(x;E)\right)\begin{pmatrix} c^{(1)}_{R,\ell'}(E) \\ c^{(2)}_{R,\ell'}(E)\end{pmatrix} \\ \equiv \sum_{\ell'} U_{\ell,\ell'}\Psi_{R,\ell'}(x;E)C_{R,\ell'}(E) \end{aligned} \tag{5.37}$$

where $\psi_{L/R,\ell}$ satisfy

$$\left(\left[-iv_F\partial_x\sigma_x + \frac{v_F k_\ell}{L}\sigma_y - \mu_S\right]\tau_z + \Delta_0\tau_x - E\right)\psi^{(i)}_{L/R,\ell}(x;E) = 0 \tag{5.38}$$

with $\psi^{(i)}_{L/R,\ell}(x \to \mp\infty; E) \to 0$. Even though $A_y(x > W/2) \neq A_y(x < -W/2)$, $\psi_{R,l}$ and $\psi_{L,l}$ are zero modes of the same operator, since for $x > W/2$ there is an additional contribution following from

$$\sum_p U^\dagger_{\ell p} U_{p\ell'} k_p = \delta_{\ell,\ell'} \left(k_\ell - n\pi\tau_z\right), \tag{5.39}$$

which cancels the A_y-term. For the middle region it holds accordingly

$$\psi_{M,\ell}(x;E) = \left(\psi^{(1)}_{L,\ell}(x;E), \dots, \psi^{(4)}_{L,\ell}(x;E)\right) \begin{pmatrix} c^{(1)}_{L,\ell}(E) \\ \vdots \\ c^{(4)}_{L,\ell}(E) \end{pmatrix} \equiv \Psi_{M,\ell}(x;E) C_{M,\ell}(E) \tag{5.40}$$

with

$$\left(\left[-iv_F\partial_x\sigma_x + \left(\frac{v_F k_\ell}{L} + \frac{ev_F}{c}A_y(x)\tau_z\right)\sigma_y - \mu_N\right]\tau_z + M\sigma_z - E\right)\psi^{(i)}_{M,\ell}(x;E) = 0. \tag{5.41}$$

In this form, we can write the matching conditions at the boundaries as

$$\Psi_{L,\ell}(-W/2;E)C_{L,\ell}(E) = \Psi_{M,\ell}(-W/2;E)C_{M,\ell}(E), \tag{5.42}$$

$$\sum_{\ell'} U_{\ell,\ell'}\Psi_{R,\ell'}(W/2;E)C_{R,\ell'}(E) = \Psi_{M,\ell}(W/2;E)C_{M,\ell}(E), \tag{5.43}$$

from which follows

$$\sum_{\ell'=-\infty}^{\infty} M_{\ell,\ell'}(E) \begin{pmatrix} C_{R,\ell'}(E) \\ C_{L,\ell'}(E) \end{pmatrix} = 0 \tag{5.44}$$

with the 4×4 matrices

$$M_{\ell,\ell'} = \Big(U_{\ell,\ell'}\Psi_{R,\ell'}(W/2;E), \quad -\Psi_{M,\ell}(W/2;E)\Psi^{-1}_{M,\ell}(-W/2;E)\Psi_{L,\ell}(-W/2;E)\delta_{\ell,\ell'}\Big). \tag{5.45}$$

Thus, the spectrum of the system is determined by the existence of zero modes of the infinite spectral matrix $M(E)$ with entries $M_{\ell,\ell'}(E)$, which can be found as presented in the following section.

5.3.3 Determining the entries of the spectral matrix

In the superconducting regions, the eigenvalue equation can be rearranged to

$$v_F\partial_x\psi_S = \left[\frac{v_F k_\ell}{L}\sigma_z + i\mu_S\sigma_x + \Delta_0\tau_y\sigma_x + iE\tau_z\sigma_x\right]\psi_S \tag{5.46}$$

which is solved by $\psi_S(x) = \xi_S e^{\kappa_S x/v_F}$ with κ_S the eigenvalues of the matrix in the square brackets and ξ_S the corresponding eigenvectors. For the left/right region we choose $\mathrm{Re}(\kappa_S) \gtrless 0$, respectively.

Then

$$\Psi_{L,\ell}(-W/2;E) = \left(\xi^{(1)}_{L,\ell}(E)e^{-\kappa^{(1)}_{L,\ell}(E)W/2}, \quad \xi^{(2)}_{L,\ell}(E)e^{-\kappa^{(2)}_{L,\ell}(E)W/2}\right) \tag{5.47}$$

and

$$\Psi_{R,\ell}(W/2;E) = \left(\xi^{(1)}_{R,\ell}(E)e^{\kappa^{(1)}_{R,\ell}(E)W/2}, \quad \xi^{(2)}_{R,\ell}(E)e^{\kappa^{(2)}_{R,\ell}(E)W/2}\right). \tag{5.48}$$

Due to the x-dependence of A_y in the middle region, the solutions are a bit more involved. Since the Hamiltonian here is diagonal in particle-hole space, we can consider $\tau_z = \pm 1$ separately. The eigenvalue equation can then be written as

$$\left(\pm v_F(-i\partial_x)\sigma_x + \frac{v_F\pi}{l_BW}\left(x + \frac{W}{2} \pm \frac{l_BW}{\pi}\frac{k_\ell}{L}\right)\sigma_y + M\sigma_z\right)\psi^{(\pm)}_{M,\ell}(x) = (E \pm \mu_N)\psi^{(\pm)}_{M,\ell}(x). \tag{5.49}$$

Defining the dimensionless coordinate

$$\tilde{x}_\pm := \sqrt{\frac{\pi}{l_BW}}\left(x + \frac{W}{2} \pm \frac{l_BW}{\pi}\frac{k_\ell}{L}\right) \quad \Rightarrow \quad \partial_x = \sqrt{\frac{\pi}{l_BW}}\partial_{\tilde{x}_\pm} \tag{5.50}$$

and introducing in each case the harmonic oscillator ladder operators

$$\tilde{x}_\pm = \frac{1}{\sqrt{2}}(a^\dagger + a), \quad -i\partial_{\tilde{x}_\pm} = \frac{i}{\sqrt{2}}(a^\dagger - a) \tag{5.51}$$

we find

$$\left[\pm i(a^\dagger\sigma_\mp - a\sigma_\pm) + \tilde{M}\sigma_z\right]\psi^{(\pm)}_{M,\ell}(\tilde{x}) = \tilde{E}_\pm\psi^{(\pm)}_{M,\ell}(\tilde{x}) \tag{5.52}$$

with $\tilde{M} = \sqrt{\frac{l_BW}{2\pi v_F^2}}M$, $\tilde{E}_\pm = \sqrt{\frac{l_BW}{2\pi v_F^2}}(E \pm \mu_N)$ and $\sigma_\pm = \frac{1}{2}(\sigma_x \pm i\sigma_y)$.

The four linearly independent solutions read (up to normalization)

$$\psi^{(1)}_{M,\ell}(x;E) = \left(i\phi^{K_+-1}_{0,\ell}(\tilde{x}_+)\left|\uparrow_\sigma\right\rangle + (\tilde{M} - \tilde{E}_+)\phi^{K_++1}_{1,\ell}(\tilde{x}_+)\left|\downarrow_\sigma\right\rangle\right)\left|\uparrow_\tau\right\rangle, \tag{5.53}$$

$$\psi^{(2)}_{M,\ell}(x;E) = \left((\tilde{M} + \tilde{E}_+)\phi^{K_+-1}_{1,\ell}(\tilde{x}_+)\left|\uparrow_\sigma\right\rangle - i\phi^{K_++1}_{0,\ell}(\tilde{x}_+)\left|\downarrow_\sigma\right\rangle\right)\left|\uparrow_\tau\right\rangle, \tag{5.54}$$

$$\psi^{(3)}_{M,\ell}(x;E) = \left(-i\phi^{K_-+1}_{0,\ell}(\tilde{x}_-)\left|\uparrow_\sigma\right\rangle + (\tilde{M} - \tilde{E}_-)\phi^{K_--1}_{1,\ell}(\tilde{x}_-)\left|\downarrow_\sigma\right\rangle\right)\left|\downarrow_\tau\right\rangle, \tag{5.55}$$

$$\psi^{(4)}_{M,\ell}(x;E) = \left((\tilde{M} + \tilde{E}_-)\phi^{K_-+1}_{1,\ell}(\tilde{x}_-)\left|\uparrow_\sigma\right\rangle + i\phi^{K_--1}_{0,\ell}(\tilde{x}_-)\left|\downarrow_\sigma\right\rangle\right)\left|\downarrow_\tau\right\rangle \tag{5.56}$$

with $\left|{\uparrow\!\downarrow}_{\{\sigma,\tau\}}\right\rangle$ denoting the eigenvectors of σ_z and τ_z, respectively. We defined here the generalized harmonic oscillator eigenfunctions (see Ref. [123] and Appendix C.3)

$$\phi^K_{0,\ell}(x) = M\left(\frac{1-K}{4}, \frac{1}{2}, x^2\right)e^{-x^2/2}, \tag{5.57}$$

$$\phi^K_{1,\ell}(x) = x\,M\left(\frac{3-K}{4}, \frac{3}{2}, x^2\right)e^{-x^2/2} \tag{5.58}$$

with $K_\pm = \tilde{E}_\pm^2 - \tilde{M}^2$ and $M(a,b,z)$ the confluent hypergeometric function of the first kind.

Finally, it is

$$U_{\ell,\ell'} = \frac{1}{L}\int_0^L dy\, e^{-i\varphi(y)\tau_z/2} e^{-i(k_\ell - k_{\ell'})y/L} = e^{-i\varphi_0\tau_z/2}\int_0^1 d\tilde{y}\, e^{-i\pi(n\tau_z + 2(\ell-\ell'))\tilde{y}} \tag{5.59}$$

$$= e^{-i\varphi_0\tau_z/2}\sigma_0 \begin{cases} \begin{pmatrix} 0 & 0 \\ 0 & 1 \end{pmatrix}, & n = 2(\ell-\ell'), \\ \begin{pmatrix} 1 & 0 \\ 0 & 0 \end{pmatrix}, & n = -2(\ell-\ell'), \\ \frac{i}{\pi}((-1)^n - 1)\begin{pmatrix} (2(\ell-\ell')+n)^{-1} & 0 \\ 0 & (2(\ell-\ell')-n)^{-1} \end{pmatrix}, & \text{else.} \end{cases}$$

where we remember $L = n \cdot l_B$. With this we know all components of $M(E)$.

Practically, we need to cut off $M(E)$ at some $|\ell| = \ell_c$ and argue that high momenta $k_{\ell > \ell_c}$ do not contribute to the low energy physics. Due to this cut-off and finite numerical precision, we will not be able to find exact zero-modes of $M(E)$. The eigenvalue $\lambda_M(E)$ with the smallest magnitude will in general be non-zero. However, we observe that with an appropriately chosen and sufficiently large cut-off, values of the order of $|\lambda_M(E)| \simeq 10^{-4\cdots-15}$, separated from the next largest eigenvalue by multiple orders of magnitude, can be achieved. We argue that, within the employed approximations, these can be interpreted as true zero-modes of $M(E)$.

Note that for the case of even n, each Fourier mode is pairwise coupled to only two others, since the non-diagonal contributions are given by $U_{l,l'} \sim \delta_{n,2|l-l'|}$ (in contrast to odd n, where the coupling between Fourier modes extends infinitely far $\sim [2(\ell-\ell')+n]^{-1}$). When employing a cut-off, the modes with $\ell = \pm\ell_c$ thus only couple to one mode each. This allows for unphysical non-trivial solutions (regardless of the parameters) where the contributions from the subspace $\{-\ell_c, -\ell_c + 2, \ldots, \ell_c\}$ vanish, although these kinds of eigenstates cannot be present in the infinite matrix-limit. To combat this artifact of the cut-off procedure in the case of even n, we artificially introduce an additional matrix element between $+\ell_c$ and $-\ell_c$, such that there exists no decoupled subspace. With the cut-off being chosen large enough for these modes not to significantly contribute to the low-energy physics, one now obtains physically sensible results which are independent of this fictitious coupling.

In Appendix C.4, we confirm that in the appropriate regime the results obtained via this method are in agreement with Ref. [114], where the effective theory-approach presented in Section 5.2.2 had been employed for the case without magnetization $M = 0$. The parameter regimes corresponding to vanishingly small effective velocities, which we established to not be accessible using said approach, will be examined in the following.

5.4 Emergence of additional zero modes near low-effective velocity-points

In Section 5.2.5, we saw close to points with sufficiently small values of $|v_{\text{eff}}|/v_F$, that the effective Dirac-like theory breaks down and higher-order corrections need to be included. We expected this to lead to altered profiles of the probability densities of the CdGM states compared to the usual expectations. In the following, we confirm this suspicion using the spectral matrix-approach just introduced. In doing so, however, we furthermore are able to identify new low-energy degrees of freedom which occur near these points and fundamentally elude the effective theory.

5.4.1 Spectral flow

In Ref. [114], in the Andreev regime the effective velocity near the Josephson vortices has been found to be proportional to $\sin(\mu_N W/v_F)$. Thus, it becomes zero if $\mu_N W/v_F$ is an integer mutiple of π. As a direct consequence, the authors found around such points all bound states in the effective theory to condense around zero energy. In Fig. 5.6a, we sketch an example for the energy of the first excited state as a function of μ_N obtained via the effective theory, which goes to zero at $\mu_N/\Delta_0 = \pi(W/\xi)^{-1}$ (as just mentioned, within the effective theory the energies of *all* excited states go to zero at this point. Here, we only plot the first excited state for better legibility). In color the associated eigenvalue λ_M of the spectral matrix is shown, where we remember that $\lambda_M \simeq 0$ corresponds to an eigenstate of the Hamiltonian.

At small μ_N, the two methods coincide and result in roughly the same energy of the first excited state (see also Appendix C.4). However, as we get closer to the zero-effective velocity point, the disagreement between the two methods grows. While within the spectral matrix approach an accumulation of bound states at low energies is still present, it occurs at a shifted value of μ_N compared to the effective theory. Furthermore, it is only the first excited state that goes to zero energy as μ_N is increased. The other states remain at finite energy. The condensation of all bound states at zero energy within the effective theory can thus be attributed to its previously discussed breakdown in the case of low effective velocities. Curiously, after merging with the zero-energy state at $\mu_N = \mu_N^{(c)}$, what previously was the first excited state remains at this energy and we obtain triply degenerate zero-energy states for $\mu_N > \mu_N^{(c)}$ (triply, because due to particle-hole symmetry there is also a state merging from the negative energies).

In Figs. 5.6b and 5.7a, we confirm that this picture also holds true for differently chosen sets of parameters, not corresponding to the Andreev regime. In Fig. 5.6b, the magnetization is finite and the parameters are chosen such that the transverse Hamiltonian only exhibits two branches of bound states in the gap for all values of μ_N shown (as in Fig. 5.4). In Fig. 5.7a, furthermore the periodic behavior in μ_N (which is also present in the effective theory) is displayed. To exemplify the degeneracy at zero energy, in Fig. 5.8 we additionally show the behavior of the lowest-lying eigenvalues of $M(E=0)$ as a function of μ_N.

Examining the corresponding wave functions, depicted in Fig. 5.7b, we see that the bound states at low energies exhibit an oscillatory behavior in the vicinity of the special point $\mu_N^{(c)}/\Delta_0 \approx 10\pi$, as can be expected from the leading order corrections to the low-energy Hamiltonian in the low-effective velocity case derived in Section 5.2.5. As μ_N grows, what for $\mu_N < \mu_N^{(c)}$ is the second excited state changes shape and takes on the role of the first excited state for $\mu_N > \mu_N^{(c)}$. The newly formed zero-modes are furthermore localized in the Josephson vortex as well.

The emergence of additional zero-modes can be a signature of a topological phase transition (the Hamiltonian (5.3) belongs to the Altland-Zirnbauer symmetry class D, which in $d = 2$ dimensions has a $\mathbb{Z}$-valued topological invariant). Note firstly, however, that the new zero modes are generically not Majorana states, since under charge conjugation, rather than being

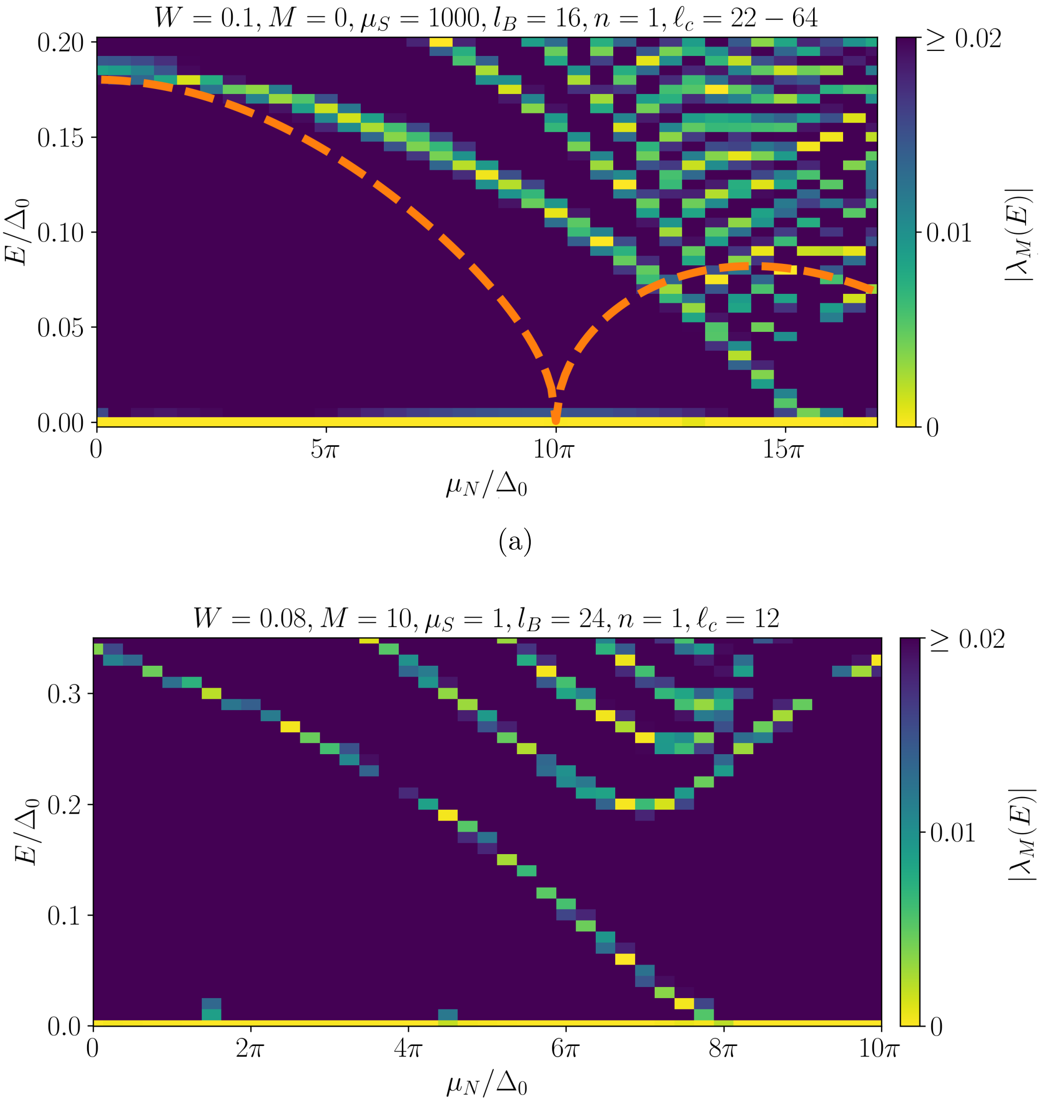

(a)

(b)

Figure 5.6: **Spectral flows in two distinct regimes.** Shown in color is the absolute value of the lowest-lying eigenvalue $\lambda_M(E)$ of the spectral matrix $M(E)$ for the respective parameter combinations and energies. Bright spots indicate the presence of an eigenmode. In both the Andreev regime (a) and the strongly magnetized regime (b), we observe that the first excited state merges with the zero-energy state as a function of μ_N. In (a), the orange dashed line corresponds to the prediction for the first excited state from Ref. [114].

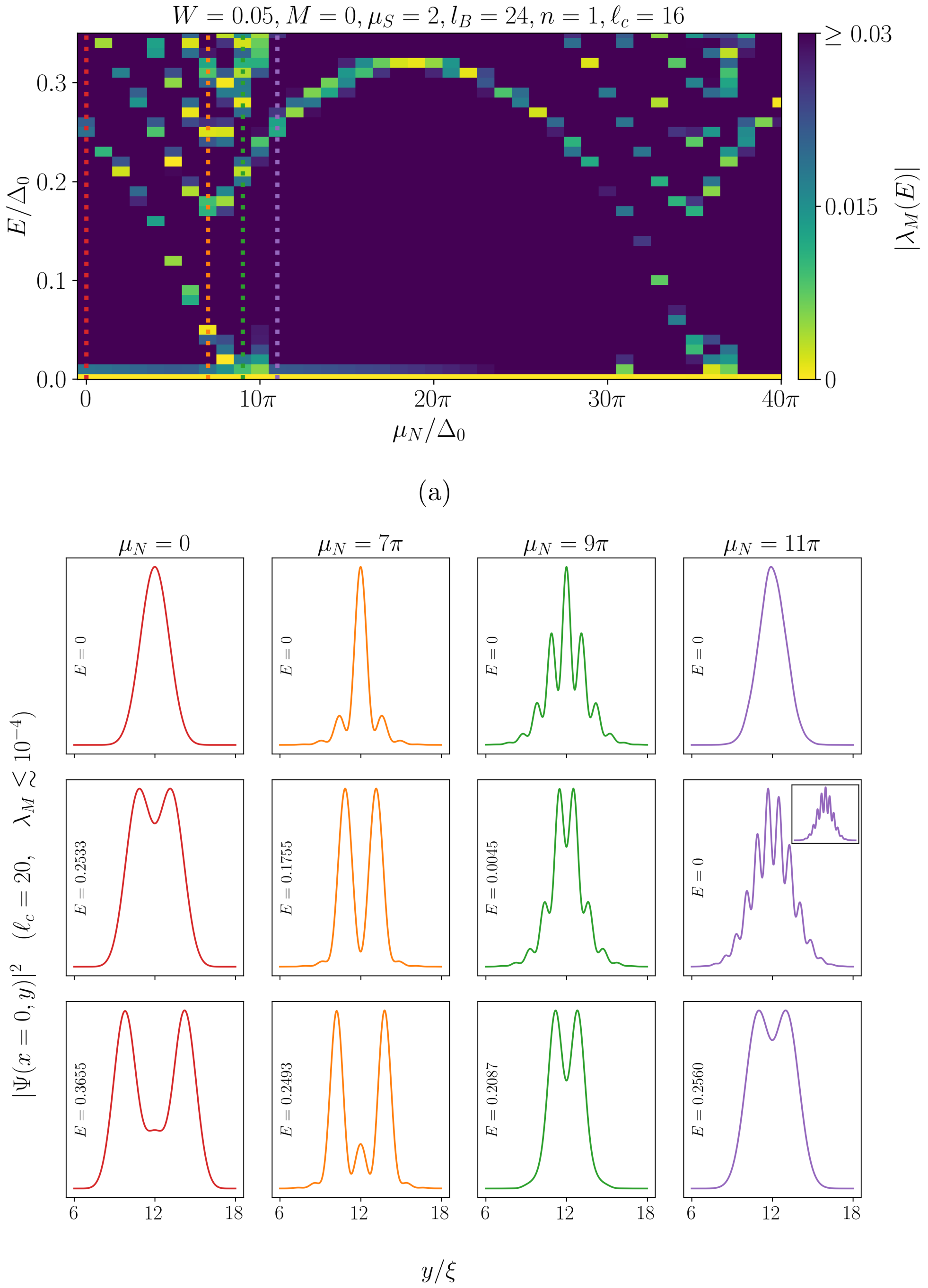

(a)

(b)

Figure 5.7: **Spectral flow and corresponding probability densities.** As in Fig. 5.6 for different parameter combinations, in panel (a) the merging of the first excited state with the zero-energy state is observed. Here, it can additionally be seen that this process is periodic in μ_N. The colored dotted lines indicate the slices for which the respective probability densities of the first three eigenmodes are plotted in panel (b). After the transition near $\mu_N^{(c)}/\Delta_0 \approx 10\pi$, the $E = 0$-state is triply degenerate and (including the inset), we show three linearly independent superpositions within this subspace.

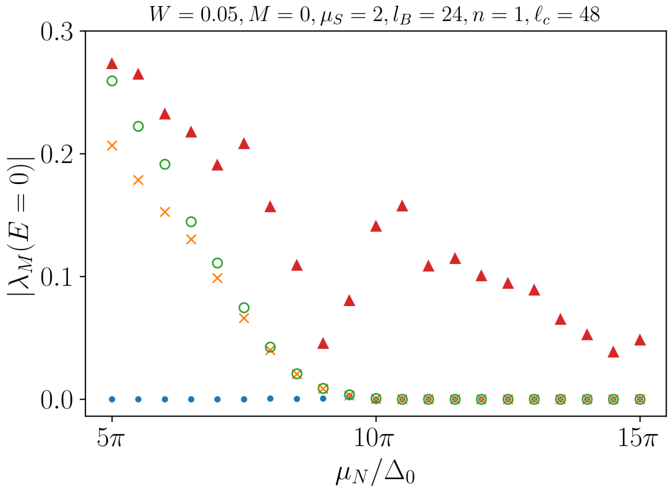

Figure 5.8: **The absolute values of the four lowest-lying eigenvalues** of $M(E = 0)$ near the transition point for the parameter combination indicated above the plot (same as in Fig. 5.7). For $\mu_N > \mu_N^{(c)}$, the $E = 0$ -state can be seen to be triply degenerate.

self-conjugate, they transform into one another. Only appropriately chosen linear combinations are self-conjugate. In fact, further investigation reveals that these zero modes are not robust against small deformations of the Hamiltonian. Introducing a small asymmetry to the junction, for example by taking $\mu_S(x)$ or $\Delta_0(x)$ to be slightly different on the left and right side, leads to a small shift away from zero energy, as can be seen in Appendix C.5. In real systems, these CdGM states thus have to be expected to manifest at very small, but non-zero energies. The observed additional zero modes can thus likely be characterized as accidental zero modes instead of the result of a topological phase transition.

In order to understand the origin of this phenomenon and the reason for it being missed by the effective theory, we need to return to the system without any external magnetic field and a fixed phase difference.

5.4.2 Revisiting the field-free model

In the case of no external magnetic field and thus translational symmetry in y-direction, the momentum $p_y \equiv k$ is conserved and the problem can be solved for each value of k separately. Instead of taking $k = 0$ and subsequently including small values of k perturbatively, as has been the strategy in Ref. [13] and the previous chapters of this thesis, let us here thus find the low-energy eigenmodes of

$$h_k(x) = [-iv_F\partial_x\sigma_x + v_F k\sigma_y - \mu(x)]\,\tau_z + M(x)\sigma_z + \Delta_0(x)\,(\cos\varphi(x)\tau_x + \sin\varphi(x)\tau_y)\,, \quad (5.60)$$

directly for each value of k, with $\mu(x)$, $M(x)$, $\Delta_0(x)$ and $\varphi(x)$ as given in (5.4).

Using the parameters from Fig. 5.7a, for small values of μ_N below the phase transition, we recover the earlier results: plotting in Fig. 5.9a the dispersion, i.e. the energies $E(k)$ at which an eigenmode can be found, for a phase difference of $\varphi = \pi$ two linearly dispersing modes crossing at $E(k = 0) = 0$ are visible. These correspond to the familiar one-dimensional

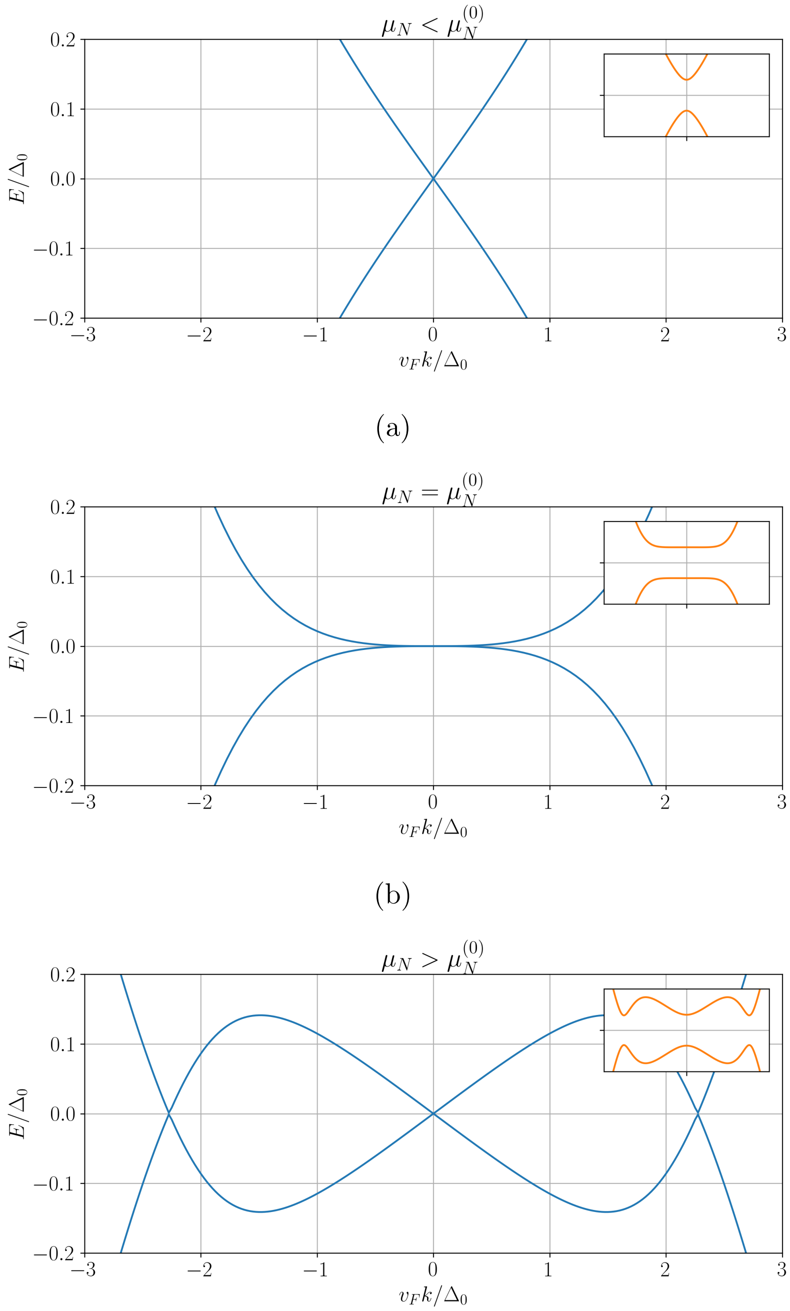

(a)

(b)

(c)

Figure 5.9: **Dispersion of the one-dimensional bound states** following from the Hamiltonian (5.60) with $\varphi = \pi$ and the parameters from Fig. 5.6. At the point $\mu_N^{(0)}/\Delta_0 \approx 3.625\pi$ (b) at which the effective velocity (i.e. the slope at $k = 0$) becomes zero, the non-linear corrections to the previously linear dispersion (shown in (a) with $\mu_N/\Delta_0 = 0.1\pi$, where the naive effective theory is still an adequate description) become apparent. Increasing μ_N further to $\mu_N/\Delta_0 = 5.5\pi$ (c), two additional Dirac cones, i.e. linearly dispersing low-energy modes, at finite momenta appear. The insets show the opening of a gap for $\varphi \neq \pi$ in each case.

counter-propagating Majorana modes. The slope is equal to the effective velocity $dE/dk|_{k=0} = v_{\text{eff}}(\varphi = \pi) = v$. Away from $\varphi = \pi$, a gap opens (see inset), as the hybridization between the Majorana modes is proportional to $\cos(\varphi/2)$ [13], which we remember is exactly what leads to the Majorana zero modes being bound to the Josephson vortices in the preceding sections.

As we increase μ_N, the slope v diminishes and we approach the point $\mu_N^{(0)}$ at which the effective velocity vanishes (Fig. 5.9b). There, the non-linear nature of the dispersion becomes apparent, corresponding to the higher-order corrections derived in Section 5.2.5. Increasing μ_N beyond $\mu_N^{(0)}$ (Fig. 5.9c), two additional low-energy Dirac cones appear at finite momenta $k = \pm K$. These are gapless only at $\varphi = \pi$ as well and thus fully explain the emergence of additional zero modes we observed above via the spectral matrix-approach. Indeed, examining in Fig. 5.10 the shape of the three degenerate zero modes in k-space, they have support only near three distinct values of k_ℓ symmetric around zero. For growing μ_N, more and more such Dirac cones appear (see Fig. 5.11a).

The fact that we find the transition in the Corbino systems to happen at a significantly shifted point $\mu_N^{(c)} > \mu_N^{(0)}$ is partly (but not fully) caused by finite size effects, as can be deduced from tracing $\mu_N^{(c)}$ as a function of increasingly large lengths l_B in Fig. 5.11b.

It is now clear that the effective theory-approach is insufficient not only as $v \to 0$, but that the included expansion around $k = 0$ furthermore does not necessarily capture all relevant low-energy degrees of freedom.

Considering experimentally available topological insulators, the values of μ_N necessary to be able to observe the emergence of the additional Dirac cones can moreover be estimated to be well within the regime in which the effective 2D description (5.3) in terms of Dirac surface states holds. E.g. in Ref. [124], in Sn-doped $\mathrm{Bi_{1.1}Sb_{0.9}Te_2S}$ with $v_F \simeq 400\,\mathrm{meV\,nm}$, it is found that μ_N can become as large as $\sim 100\,\mathrm{meV}$ before entering the bulk bands. Assuming the induced superconducting gap Δ_0 to be of the order of $\sim 1\,\mathrm{meV}$, it holds $\mu_N^{(c)} \sim 25 - 50\,\mathrm{meV}$ with the values we found above. Here, we would like to point out that although we focused on tuning the chemical potential μ_N in the non-superconducting region, other quantities, as for example the width W of the junction, can also be used as control parameters of the transition.

Note that the appearance of the additional 1D Dirac cones is in principle already present in a very similar analysis carried out for a graphene-system in Ref. [117], though it is not explicitly mentioned there.

Breaking the x-inversion symmetry, as shown in Appendix C.5, finally reveals that the crossings at finite momenta are not robust, as a small gap opens. Though these points still introduce relevant low-energy degrees of freedom, the bound states we observed in the preceding section are thus in realistic systems no true zero modes, but ordinary CdGM states with very small energies instead. As such, they have to be still expected to significantly contribute to the low-energy physics of the system and have to be taken into account in the interpretation of e.g. measured Josephson currents and microwave spectroscopies [114, 125].

5.5 Summary

Generalizing the effective low-energy theory employed in the preceding chapters to take into account the spatial variation of parameters along the junction, as for example the linearly growing phase difference due to an external magnetic field, we discovered zeros of the effective

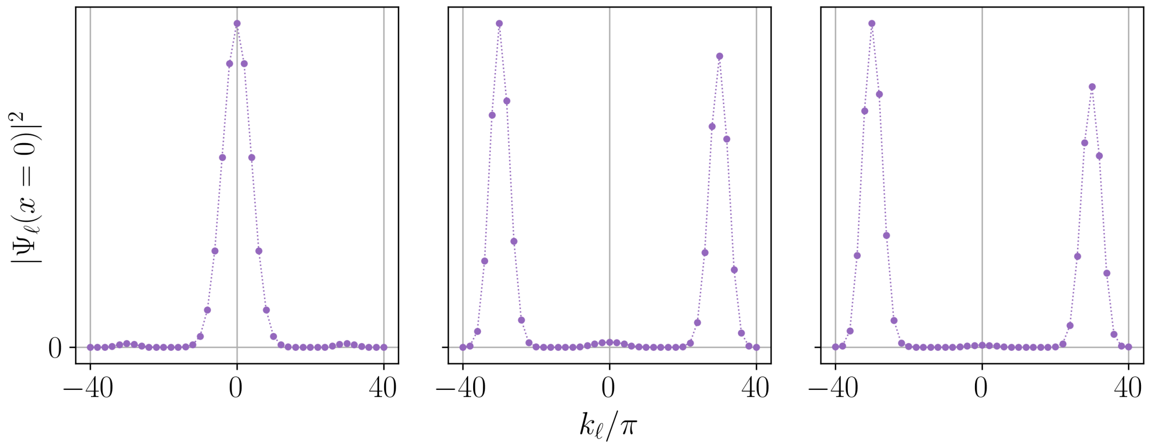

Figure 5.10: **Zero-energy bound states in Fourier space.** Shown are the probability densities for a slice at $x = 0$ corresponding to the three $E = 0$ -states at $\mu_N/\Delta_0 = 11\pi$ in Fig. 5.7b. The subspace thus only has support near three distinct values of k_ℓ symmetric around $k_\ell = 0$, as expected from Fig. 5.9. Shown are arbitrary linearly independent superpositions within the degenerate subspace.

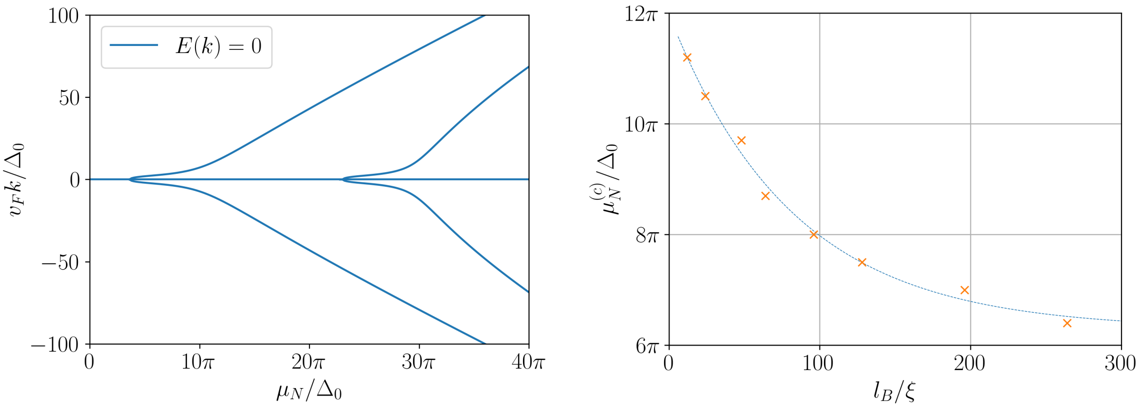

(a)

(b)

Figure 5.11: (a) **Centers of one-dimensional Dirac cones**, determined by the values of k for which $E(k) = 0$, as a function of μ_N following from (5.60) for the parameters given in Fig. 5.7. As μ_N grows, new Dirac cones emerge periodically every time the effective velocity at $k = 0$ vanishes. The first branching occurs at $\mu_N^{(0)}/\Delta_0 \approx 3.6\pi$.
(b) **Scaling of the critical chemical potential with the length of the ring.** As l_B becomes larger, the critical value $\mu_N^{(c)}$, at which the degeneracy of the $E = 0$ -CdGM state is observed to be increased, decreases exponentially. The extrapolation suggests $\mu_N^{(c)}/\Delta_0 \to 6.3\pi$ for $l_B \to \infty$.

velocity to correspond to points at which this frequently utilized effective description breaks down.

Taken at face value, it predicts the zero-velocity points to emulate black hole-event horizons, leading to unexpected divergent behavior. To remedy this, we included higher-order corrections to the low-energy description, stemming from virtual processes coupling the in-gap with the above-gap states. These corrections result in an effective Hamiltonian which no longer posseses Dirac, but rather Schrödinger nature as it is governed by a second-order derivative. This higher-order derivative regularizes the unphysical divergences. However, by means of a different approach, we revealed that the effective theory misses another crucial aspect of the low-energy physics, which relates to the zeros of the effective velocity as well.

In the translationally invariant situation, additional Dirac cones at zero energy, centered at non-zero momenta, emerge periodically anytime the effective velocity vanishes. In our example of the running phase, this leads to additional zero modes being bound to each Josephson vortex.

Although the crossings of the Dirac cones, and thus the zero modes, are not robust under the breaking of inversion symmetry and therefore will not correspond to true zero modes in a realistic scenario due to disorder and irregularities, as long as these effects are small, the additional low-lying states have to be taken into account in the interpretation of experiments.

6

Chapter 6

Conclusions and outlook

In this thesis we presented a study of topological Josephson junctions across a variety of realizations. By extending the well-known description in terms of one-dimensional Majorana modes to incorporate the dynamics of coupled bosonic degrees of freedom, as well as probing the boundaries of said effective theory's applicability, we have uncovered novel phenomena which may prove crucial towards a comprehensive understanding of the low-energy physics in these topological Josephson structures.

One such system is given by the Josephson junction on a topological insulator surface formed between two s-wave superconductors with a ferromagnet deposited between them. Here, the ferromagnet's magnetization induces an exchange field which couples to the spin of the electronic surface states. In Section 3.1, we have seen that the component of the magnetization which is perpendicular to the junction acts similarly to a phase bias between the superconductors in that it hybridizes the counter-propagating Majorana modes. Taking into account that the magnetization dynamics can be described by the Landau-Lifshitz-Gilbert equation and assuming a large magnetic easy-axis anisotropy perpendicular to the surface, we then deduced a logarithmic Peierls instability towards the opening of a Majorana mass gap with a spontaneous $\mathbb{Z}_2$ symmetry breaking. Within mean-field theory, this corresponds to the splitting and tilting of the easy-axis. The mean-field result is stabilized against quantum fluctuations by means of the spatial and temporal rigidities of the magnetization dynamics. By analyzing the Gaussian fluctuations in the associated gap equation, we were able to estimate the parameter regime in which the corresponding quantum phase transition takes place. By analogy to related models, we expect this transition to be described by the tricritical Ising universality class and our system could thus provide a physical realization of the abstract models proposed in Refs. [69, 70]. A possible experimental signature of this broken symmetry is a discontinuous jump in the corresponding current-phase relation. In analogy to the Ising model at low but finite temperatures, we argued that there are exponentially large stretches of ordered phase, which are separated by domain walls, each carrying a Majorana bound state. The energy and width of these domain walls allow an estimate of the magnetic coherence length. We furthermore provided the corresponding self-consistency problem in the case of stationary solitons, for which the solution is known if the exchange coupling can be neglected.

The non-trivial dynamics these solitons exhibit, being governed by the Landau-Lifshitz-Gilbert equation, is an exciting avenue to be explored in future research. Possibly building on similar work which made use of inverse scattering theory [126, 127], understanding dynamical and scattering processes of the solitons ensues prospects for the experimental detection and control of the associated Majorana bound states.

Another system in which we discovered solitons to carry Majorana bound states under interesting circumstances are the Josephson junctions comprised of two-dimensional time-reversal invariant topological superconductors which we studied in Section 3.2. Analogously to the magnetic system, in the TRITOPS-S junction we encountered a Peierls instability which is stabilized by the stiffness of the phase bias' dynamics, leading to a spontaneously broken time-reversal symmetry. Consequently, the solitons in this phase correspond to fractional fluxons, each carrying a single Majorana state. In the TRITOPS-TRITOPS junction, no spontaneous symmetry breaking takes place. Interestingly, though the presence of a fluxon breaks time-reversal symmetry explicitly, here we found Majorana bound states to appear in pairs due to an accidental inversion symmetry which protects the Kramers degeneracy.

In Chapter 4 we returned to the topological SMS junction, extending the effective theory to take into account arbitrary magnetic anisotropies. Both in the easy-plane and weak easy-axis case we identified BKT transitions. In the latter case, this is based on an emergent effective easy-plane, spanned by the easy-axis and the component of the magnetization which couples to the Majoranas. Furthermore, the experimental accessibility of these transitions has been estimated and discussed. By combining the complementary pictures from the mean-field and perturbative RG analysis, which we conducted here, with the results for the strong easy-axis anisotropy from Section 3.1, we arrived at a conjecture for the parts of the phase diagram which are not accessible by these methods. There, prospects for the realization of exotic multicritical points are given.

Establishing and harnessing a connection to related models which were shown to feature multicritical points and emergent supersymmetry [111, 128] is a promising avenue for future work towards confirming and expanding on our conjectures.

Finally, we examined the effective low-energy theory the previous chapters were built on for its range of applicability. To this end, we simplified our previous model of the SMS junction by eliminating the magnetization dynamics in place of an external magnetic field, which leads to the phase bias growing linearly along the junction.

In the first part of Chapter 5, we showed that, if applied naively, the low-energy description erroneously predicts black hole-analogues to occur for specific parameter combinations, leading to anomalous behavior of the bound state wave functions. These points at which the effective theory loses validity correspond to instances of vanishing effective velocity of the one-dimensional Majorana modes. Subsequently, we demonstrated how the black hole-anomalies can be regularized by including corrections from virtual processes via the quasiparticle continuum to the theory, resulting in a quadratic dispersion in place of the Dirac cone.

In order to confirm the breakdown of the effective theory at these zero-velocity points, we derived an alternative approach via an expansion in Fourier modes in a Corbino geometry of the junction. By means of this, we were indeed able to see the growing discrepancy between the two approaches as the effective velocity diminishes. Additionally and surprisingly to us, it also revealed that the zero-velocity points furthermore mark points at which additional low-energy degrees of freedom emerge, leading to an increase of the number of zero modes bound to each Josephson vortex. Although these additional zero modes are not robust against irregularities which break the inversion symmetry, they can be expected to significantly contribute to the low-energy physics of real systems as low-lying CdGM states.

Thus, possible directions for future work lie in an explicit inclusion of these additional states in the interpretation of experiments done in topological Corbino geometry Josephson junctions [115, 116], expanding the employed method to be able to account for irregularities and disorder [114] as well as further investigations of the spectrum in instances where overlap between neighboring CdGM states is present and significant.

To summarize, in this thesis we have thus conducted an extensive analysis on a variety of aspects concerning topological Josephson junctions. In doing so, we were able to identify a range of quantum phase transitions, which not only demonstrate the potential for these systems to serve as a platform for the experimental realization of exotic critical phenomena, but also open new possibilities for the manipulation and detection of Majorana zero modes. In addition, we unveiled previously overlooked shortcomings of the universally employed effective theory, which are crucial for an accurate understanding of the low-energy physics in these structures.

Appendix A

Supplemental material for Chapter 3

A.1 Low-energy BdG Hamiltonian for the SMS junction

Starting from the Hamiltonian given in (3.1), by adopting a semi-classical description of the magnetization and labeling the fermionic states by their momentum $-i\partial_y \to q$, which is valid if $\vec{m}$ and φ only vary slowly with y, a low-energy effective Hamiltonian for the fermionic degrees of freedom in the considered SMS junction can be derived analogously to what has been done in Ref. [13]. To this end, we consider the limit where the width of the junction is much smaller than the superconducting coherence length $W \ll v_{\mathrm{F}}/\Delta_0$, such that there exist only two branches of in-gap bound states (related by particle-hole symmetry). Splitting (3.1) into two parts, $h = h^{(0)} + h^{(1)}$, with $h^{(0)} = h|_{q=m_x=m_y=0,\varphi=\pi}$ and treating $h^{(1)}$ as a small perturbation, one then finds zero-energy solutions $h^{(0)}\zeta_{a=1,2} = 0$, onto which h can be projected to define the effective BdG Hamiltonian. It is convenient to choose them such that they obey $\mathcal{C}\zeta_a = \zeta_a$ with the charge conjugation operator $\mathcal{C} = \tau_y\sigma_y\mathcal{K}$, where $\mathcal{K}$ denotes complex conjugation. They can be written as

$$
\begin{aligned}
\zeta_\pm(x) &\equiv \zeta_1(x) \pm i\zeta_2(x) \\
&\propto e^{i\pi\sigma_z/4}\left[-\sqrt{\mu+M}\begin{pmatrix} -\cos\frac{\mu\vartheta(x)}{v_{\mathrm{F}}} \\ \sin\frac{\mu\vartheta(x)}{v_{\mathrm{F}}} \\ \sin\frac{\mu\vartheta(x)}{v_{\mathrm{F}}} \\ \cos\frac{\mu\vartheta(x)}{v_{\mathrm{F}}} \end{pmatrix} \mp i\sqrt{\mu-M}\begin{pmatrix} \sin\frac{\mu\vartheta(x)}{v_{\mathrm{F}}} \\ \cos\frac{\mu\vartheta(x)}{v_{\mathrm{F}}} \\ \cos\frac{\mu\vartheta(x)}{v_{\mathrm{F}}} \\ -\sin\frac{\mu\vartheta(x)}{v_{\mathrm{F}}} \end{pmatrix}\right] \times \\
&\qquad \times \exp\left[\mp i\sqrt{\mu^2-M^2}(x-\vartheta(x))/v_{\mathrm{F}} - \int_0^{|y|} d\tilde{x}\,\Delta_0(\tilde{x})/v_{\mathrm{F}}\right].
\end{aligned}
\tag{A.1}
$$

Here, we defined $\vartheta(x) = \left(x - \mathrm{sgn}(x)\frac{W}{2}\right)\Theta\left(|x| - \frac{W}{2}\right)$. Small values of q, m_x, m_y and $\pi - \varphi$

are now included by calculating the matrix elements

$$\begin{aligned}\langle\zeta_a|\Delta_0(\pi-\varphi)\Theta(y-W/2)\tau_y|\zeta_b\rangle &= -\sqrt{\frac{\mu^2-M^2}{\mu^2-M^2K^2}}\frac{\Delta_0(\pi-\varphi)}{2}\rho_y^{ab},\\ \langle\zeta_a|v_{\mathrm{F}}q\tau_z\sigma_y|\zeta_b\rangle &= vq\rho_x^{ab},\\ \langle\zeta_a|M\Theta(W/2-|y|)m_y\sigma_y|\zeta_b\rangle &= \langle\zeta_a|M\Theta(W/2-|y|)\frac{m_x^2+m_y^2}{2}\sigma_z|\zeta_b\rangle = 0,\\ \langle\zeta_a|M\Theta(W/2-|y|)m_x\sigma_x|\zeta_b\rangle &= -\sqrt{\frac{\mu^2-M^2}{\mu^2-M^2K^2}}\frac{\Delta_0 MW}{v_{\mathrm{F}}}m_x\rho_y^{ab},\end{aligned} \tag{A.2}$$

where the Pauli matrices $\rho_{x,y,z}$ act on (ζ_1,ζ_2), the effective velocity reads

$$v = \sqrt{\frac{\mu^2-M^2}{\mu^2-M^2K^2}}\frac{\Delta_0^2}{\Delta_0^2+\mu^2}Kv_{\mathrm{F}} \tag{A.3}$$

and the dimensionless constant $K = \cos\left(\sqrt{\mu^2-M^2}W/v_{\mathrm{F}}\right)+\frac{\Delta_0}{\sqrt{\mu^2-M^2}}\sin\left(\sqrt{\mu^2-M^2}W/v_{\mathrm{F}}\right)$ has been defined. With that, the low-energy effective BdG Hamiltonian

$$h_{\mathrm{eff}}^{ab} = \langle\zeta_a|h|\zeta_b\rangle = -iv\partial_y\rho_x^{ab} - \sqrt{\frac{\mu^2-M^2}{\mu^2-M^2K^2}}\Delta_0\left(\frac{\pi-\varphi}{2}+\frac{MW}{v_{\mathrm{F}}}m_x\right)\rho_y^{ab} \tag{A.4}$$

is obtained. We find the component of the magnetization perpendicular to the junction m_x to play a similar role as the deviation of the phase difference from π.

In contrast to m_x, the y-component of the magnetization m_y does not directly couple to the fermionic degrees of freedom. This can also be understood via the symmetries discussed in Appendix C.1, from which follow that all matrix elements of σ_y vanish.

Finally, by fixing $\varphi=\pi$ and introducing the right- and left-moving Majorana fields $\chi_{\mathrm{R/L}}(y) = \frac{1}{\sqrt{L}}\sum_q \chi_q^{\mathrm{R/L}}e^{iqy} = \chi_{\mathrm{R/L}}^\dagger(y)$ with $\chi_q^{\mathrm{R/L}} = \int d\boldsymbol{r}\,(\xi_q^{\mathrm{R/L}}(\boldsymbol{r}))^\dagger\Psi(\boldsymbol{r}) = (\chi_{-q}^{\mathrm{R/L}})^\dagger$, where $\xi_q^{\mathrm{R/L}}(\boldsymbol{r}) = \frac{1}{\sqrt{2}}(\zeta_1(x)\pm\zeta_2(x))e^{iqy}$, we obtain

$$H_{\mathrm{eff}} = \int dy\left[-\frac{iv}{2}(\chi_{\mathrm{R}}\partial_y\chi_{\mathrm{R}}-\chi_{\mathrm{L}}\partial_y\chi_{\mathrm{L}}) - igm_x\chi_{\mathrm{R}}\chi_{\mathrm{L}}\right] \tag{A.5}$$

with the coupling constant $g = M\sqrt{\frac{\mu^2-M^2}{\mu^2-M^2K^2}}\frac{\Delta_0 W}{v_{\mathrm{F}}}$.

A.2 Calculation of the self-energy

Our aim is to calculate the self-energy $\Pi(q,\omega)$ defined in Eq. (3.13), following the method of Ref. [68]. In the zero-temperature, infinite-system limit, we can write

$$\begin{aligned}\Pi(q,\omega) &= g^2\int_{-\infty}^{\infty}\frac{dk}{2\pi}\int_{-\infty}^{\infty}\frac{d\varepsilon}{2\pi}\frac{\left(i(\varepsilon-\frac{\omega}{2})-v(k-\frac{q}{2})\right)\left(i(\varepsilon+\frac{\omega}{2})+v(k+\frac{q}{2})\right)+g^2m_0^2}{\left((\varepsilon-\frac{\omega}{2})^2+v^2(k-\frac{q}{2})^2+g^2m_0^2\right)\left((\varepsilon+\frac{\omega}{2})^2+v^2(k+\frac{q}{2})^2+g^2m_0^2\right)}\\ &= -\frac{g^2}{v}\int\frac{d^2k}{(2\pi)^2}\frac{\boldsymbol{k}_+\cdot\boldsymbol{k}_- + i(\boldsymbol{k}_+)_1(\boldsymbol{k}_-)_2 - i(\boldsymbol{k}_+)_2(\boldsymbol{k}_-)_1 - g^2m_0^2}{(\boldsymbol{k}_+^2+g^2m_0^2)(\boldsymbol{k}_-^2+g^2m_0^2)},\end{aligned} \tag{A.6}$$

where we defined $\boldsymbol{k} = (\varepsilon, vk)^T$, $\boldsymbol{q} = (\omega, vq)^T$ and $\boldsymbol{k}_\pm = \boldsymbol{k} \pm \boldsymbol{q}/2$.

In the following, we make use of the identity

$$\frac{1}{AB} \equiv \int_0^1 du \, \frac{1}{(Au + B(1-u))^2} \tag{A.7}$$

as well as

$$\int_0^1 du \, \frac{1}{m^2 - (u^2-u)q^2} = \frac{4}{q^2} \frac{r}{\sqrt{1+r^2}} \text{Arsinh}(r) \quad \text{with} \quad r^2 = q^2/4m^2. \tag{A.8}$$

We find

$$\begin{aligned} \int \frac{d^2k}{(2\pi)^2} \frac{1}{(\boldsymbol{k}_+^2 + g^2m_0^2)(\boldsymbol{k}_-^2 + g^2m_0^2)} &= \int_0^1 du \int \frac{d^2k}{(2\pi)^2} \frac{1}{(\boldsymbol{k}^2 + \boldsymbol{q}^2/4 + (1-2u)\boldsymbol{k}\cdot\boldsymbol{q} + g^2m_0^2)^2} \\ = \int_0^1 du \int \frac{d^2f}{(2\pi)^2} \frac{1}{(\boldsymbol{f}^2 - (u-u^2)\boldsymbol{q}^2 + g^2m_0^2)^2} &= \frac{1}{4\pi} \frac{4}{\boldsymbol{q}^2} \frac{r}{\sqrt{1+r^2}} \text{Arsinh}(r) := I(\boldsymbol{q}^2) \end{aligned} \tag{A.9}$$

where we defined $r^2 = \boldsymbol{q}^2/4g^2m_0^2$ and made use of the substitution $\boldsymbol{f} = \boldsymbol{k} + \frac{1}{2}(1-2u)\boldsymbol{q}$.

The rest of the terms we need to evaluate are of the form ($\alpha, \beta \in \{1, 2\}$)

$$\begin{aligned} J_{\alpha\beta}(\boldsymbol{q}^2) := \int \frac{d^2k}{(2\pi)^2} \frac{(\boldsymbol{k}_+)_\alpha (\boldsymbol{k}_-)_\beta}{(\boldsymbol{k}_+^2 + g^2m_0^2)(\boldsymbol{k}_-^2 + g^2m_0^2)} &= \int_0^1 du \int \frac{d^2f}{(2\pi)^2} \frac{(\boldsymbol{f} + u\boldsymbol{q})_\alpha (\boldsymbol{f} + (u-1)\boldsymbol{q})_\beta}{(\boldsymbol{f}^2 - (u^2-u)\boldsymbol{q}^2 + g^2m_0^2)^2} \\ = \int_0^1 du \int \frac{d^2f}{(2\pi)^2} \Bigg[\underbrace{\frac{f_\alpha f_\beta}{(\boldsymbol{f}^2 - (u^2-u)\boldsymbol{q}^2 + g^2m_0^2)^2}}_{\to J^{(0)}_{\alpha\beta}(\boldsymbol{q}^2)} &+ q_\alpha q_\beta \underbrace{\frac{u(u-1)}{(\boldsymbol{f}^2 - (u^2-u)\boldsymbol{q}^2 + g^2m_0^2)^2}}_{\to J^{(2)}_{\alpha\beta}(\boldsymbol{q}^2)} \Bigg], \end{aligned} \tag{A.10}$$

where the integrals over terms that are odd in f_α immediately vanish. It is

$$J^{(2)}_{\alpha\beta}(\boldsymbol{q}^2) = \frac{1}{4\pi\boldsymbol{q}^2} \left(\frac{\text{Arsinh}(r)}{r\sqrt{1+r^2}} - 1 \right). \tag{A.11}$$

$J^{(0)}_{\alpha\beta}(\boldsymbol{q}^2)$ diverges logarithmically. We therefore first calculate

$$J^{(0)}_{\alpha\beta}(\boldsymbol{q}^2) - J^{(0)}_{\alpha\beta}(0) = -\frac{\delta_{\alpha\beta}}{4\pi} \left(\frac{\sqrt{1+r^2}}{r} \text{Arsinh}(r) - 1 \right) \tag{A.12}$$

and finally introduce a high-momentum cut-off Λ to find

$$J^{(0)}_{\alpha\beta}(0) \simeq \frac{\delta_{\alpha\beta}}{4\pi} \left(\log \frac{2v\Lambda}{gm_0} - \delta_{\alpha,2} \right). \tag{A.13}$$

Thus, altogether

$$\begin{aligned} \Pi(q,\omega) &= -\frac{g^2}{v} \left(J_{11}(\boldsymbol{q}^2) + J_{22}(\boldsymbol{q}^2) - g^2m_0^2 \, I(\boldsymbol{q}^2) \right) \\ &= \frac{g^2}{2\pi v} \left(\log \frac{gm_0}{2v\Lambda} + \frac{\sqrt{1+r^2}}{r} \text{Arsinh}(r) \right). \end{aligned} \tag{A.14}$$

A.3 Symmetries of the TRITOPS-TRITOPS junction

Consider the BdG Hamiltonian

$$\mathcal{H}^{(\pm)} = -\mu^{(\pm)}(x)\tau_z\sigma_0 + v\tau_x(p_x\sigma_x + p_y\sigma_y), \tag{A.15}$$

modelling a TRITOPS with p-wave pairing up to leading order in the momenta, assuming zero contribution from s-wave pairing. $\mu(x)$ is taken to change sign at the edge of a given sample and the topological phase corresponds to $\mu/v > 0$. Thus, we distinguish $\mu^{(+)}(x \gtrless 0) \lessgtr 0$ and $\mu^{(-)}(x \gtrless 0) \gtrless 0$ describing right and left edges, respectively. For $p_y = 0$, we find in each case two normalizable zero modes bound to the respective edge satisfying $\mathcal{H}\Phi_0(x) = 0$ given by

$$\begin{aligned}\Phi^{(\pm)}_{0,\uparrow}(x) &= \frac{N}{2}e^{\pm\int_0^x dx'\mu(x')/v}(1 \pm i, 0, 0, -1 \pm i)^T,\\ \Phi^{(\pm)}_{0,\downarrow}(x) &= \frac{N}{2}e^{\pm\int_0^x dx'\mu(x')/v}(0, 1 \mp i, 1 \pm i, 0)^T.\end{aligned} \tag{A.16}$$

Note that the solutions are chosen such that they are orthonormal and are invariant under charge conjugation $\mathcal{C}\Phi^{(\pm)}_{0,\sigma}(0) = \Phi^{(\pm)}_{0,\sigma}(0)$, where the charge conjugation operator is given by $\mathcal{C} = \tau_y\sigma_y\mathcal{K} \equiv \mathcal{U}_C\mathcal{K}$. Additionally, it is worth noting that the two respective solutions are Kramers pairs $\mathcal{T}\Phi^{(\pm)}_{0,\downarrow} = \Phi^{(\pm)}_{0,\uparrow}$, with the time-reversal operator $\mathcal{T} = i\sigma_y\mathcal{K}$. Including finite momenta p_y entails projecting the corresponding term in the Hamiltonian onto this basis, which yields

$$\left(\Phi^{(\tau)}_{0,\sigma}(0)\right)^\dagger \tau_x\sigma_y\Phi^{(\tau')}_{0,\sigma'}(0) = (\tilde{\tau}_z)^{\tau,\tau'}(\tilde{\sigma}_z)^{\sigma,\sigma'}, \tag{A.17}$$

as given in Eq. (3.37). Transforming the anti-unitary operators $\mathcal{C}$ and $\mathcal{T}$ to this basis, one finds $\mathcal{C} = \mathcal{K}$ and $\mathcal{T} = i\tilde{\sigma}_y\mathcal{K}$.

Additionally, we can identify the symmetry corresponding to exchanging the right and the left edge with each other. On the level of the Hamiltonian in (A.15), this is achieved by simultaneous inversion along the x-axis P_x, i.e. $P_xf(x) = f(-x)$, and rotating with $U_X = \tau_z\sigma_x$,

$$(U_XP_x)\,\mathcal{H}^{(\pm)}\,(P_xU_X) = -\mu^{(\pm)}(-x)\tau_z + v\tau_x(p_x\sigma_x + p_y\sigma_y). \tag{A.18}$$

This is the same Hamiltonian as (A.15) only with the direction of the sign change of μ, which determined whether we called it a right or left edge, reversed. U_X connects the right and left edge modes in (A.16) with each other

$$U_X\Phi^{(+)}_{0,\uparrow} = \Phi^{(-)}_{0,\downarrow}, \quad U_X\Phi^{(-)}_{0,\uparrow} = \Phi^{(+)}_{0,\downarrow}. \tag{A.19}$$

Expressed in the new basis, it therefore holds

$$U_X = \tilde{\tau}_x\tilde{\sigma}_x. \tag{A.20}$$

A.4 Zero-energy solutions to double mass Dirac equation

The Dirac equation for zero modes in the TRITOPS-TRITOPS junction in the presence of a phase slip soliton reads

$$(-iv\partial_y\tilde{\tau}_z\tilde{\sigma}_z + g_1(y)\tilde{\tau}_y\tilde{\sigma}_z + g_2(y)\tilde{\tau}_0\tilde{\sigma}_y)\,\psi(y) = 0 \tag{A.21}$$

$$\Leftrightarrow \quad (v\partial_y + g_1(y)\tilde{\tau}_x\tilde{\sigma}_0 + g_2(y)\tilde{\tau}_z\tilde{\sigma}_x)\,\psi(y) = 0 \tag{A.22}$$

where asymptotically $g_1(y \to \pm\infty) = \pm g_1^{(0)}$ and $g_2(y \to \pm\infty) = 0$ with both mass terms antisymmetric $g_{1,2}(y) = -g_{1,2}(-y)$. Note that $g_2 \neq 0$ breaks time-reversal symmetry and one would thus expect the Kramers degeneracy to be lifted in its presence. However, as argued in the main text, this turns out not to be the case if both masses have well-defined parity, due to the existence of the two non-commuting "pseudo-parities" $P_1 = \tilde{\tau}_0 \tilde{\sigma}_x p$ and $P_2 = \tilde{\tau}_x \tilde{\sigma}_z p$. As a consequence, the two-fold degeneracy of the zero modes bound to the soliton also persists. Here, in order to demonstrate this, we will explicitly derive the two zero-mode solutions to Eq. (A.22) in the simple case of the soliton profile being given by

$$g_1(y) = g_1^{(0)} \mathrm{sgn}(y), \tag{A.23}$$

$$g_2(y) = g_2^{(0)} \mathrm{sgn}(y)\, \Theta(w/2 - |y|). \tag{A.24}$$

We start by looking for a solution $|\psi_1\rangle$ to (A.22) which is simultaneously an eigenvector of P_1 and make the ansatz

$$|\psi_1\rangle = |\xi_1\rangle \otimes |+\rangle\,, \tag{A.25}$$

where $\tilde{\sigma}_x |\pm\rangle = \pm |\pm\rangle$. Eq. (A.22) then reduces to

$$\left(iv\partial_y + g_1(y)\tilde{\tau}_x + g_2(y)\tilde{\tau}_z\right) \xi_1 = 0, \tag{A.26}$$

to which the normalizable solution can be found to read

$$\xi_1(y) \propto \begin{cases} \begin{pmatrix} 1 \\ 1 \end{pmatrix} e^{g_1^{(0)}(y+w/2)}, & y < -w/2, \\ \begin{pmatrix} 1 \\ 1 \end{pmatrix} \cosh\left(\frac{y+w/2}{\lambda}\right) + \lambda \begin{pmatrix} g_1^{(0)} + g_2^{(0)} \\ g_1^{(0)} - g_2^{(0)} \end{pmatrix} \sinh\left(\frac{y+w/2}{\lambda}\right), & -w/2 < y < 0, \\ \begin{pmatrix} 1 \\ 1 \end{pmatrix} \cosh\left(\frac{y-w/2}{\lambda}\right) - \lambda \begin{pmatrix} g_1^{(0)} + g_2^{(0)} \\ g_1^{(0)} - g_2^{(0)} \end{pmatrix} \sinh\left(\frac{y-w/2}{\lambda}\right), & 0 < y < w/2, \\ \begin{pmatrix} 1 \\ 1 \end{pmatrix} e^{-g_1^{(0)}(y-w/2)}, & y > w/2, \end{cases} \tag{A.27}$$

where we introduced $\left(g_1^{(0)}\right)^2 + \left(g_2^{(0)}\right)^2 \equiv \lambda^{-2}$. The second, degenerate zero mode $|\psi_2\rangle$ is then found by application of P_2 to the first solution

$$|\psi_2\rangle = P_2 |\psi_1\rangle = \tilde{\tau}_x |\xi_1\rangle \otimes |-\rangle\,. \tag{A.28}$$

Note that for $g_2^{(0)} \to 0$, $|\psi_1\rangle$ and $|\psi_2\rangle$ are indeed transformed into one another by the time-reversal operator $\mathcal{T}$.

It is easy to check that for mass profiles of the form as given in (A.23) and (A.24), but with an added asymmetry of some sort, in general no non-trivial solutions to Eq. (A.22) and thus no zero modes exist. Their degeneracy and thus existence is dependent on the parity and with that also sensitive to any impurities or inhomogeneities.

B

Appendix B

Supplemental material for Chapter 4

B.1 Derivation of RG flow equations

In the following we are going to sketch the derivation of the flow equations (4.6)-(4.9) from the action (4.5), where, for convenience, we shift $\beta\phi \to \beta\phi - \frac{\pi}{2}$

$$S = \int d\tau\, dy \Big[\underbrace{\frac{v}{2}\bar{\chi}\not{\partial}\chi + \frac{1}{2}\left(\frac{1}{c}(\partial_\tau\phi)^2 + c(\partial_x\phi)^2\right)}_{S_0} \underbrace{-u\cos 2\beta\phi + \frac{g}{2}\bar{\chi}\chi\sin\beta\phi}_{S_{\text{int}}} \Big]. \tag{B.1}$$

To this end, we employ a Wilson RG and choose a scheme in which the bosonic velocity c flows while the fermionic one v stays fixed. Following the standard approach[65, 129], the fields are split into slow ($\omega^2/v^2 + q^2 < \Lambda^2/b^2$) and fast ($\Lambda^2/b^2 < \omega^2/v^2 + q^2 < \Lambda^2$) components (with v replaced by c for the bosonic fields), $\chi = \chi_s + \chi_f$, $\phi = \phi_s + \phi_f$, and $b = e^l$, $l \ll 1$. For the partition function one then has

$$Z = \int \mathcal{D}s\,\mathcal{D}f\, e^{-S_0[s]-S_0[f]-S_{\text{int}}[s+f]} = Z_0^f \int \mathcal{D}s\, e^{-S_0[s]}\, \langle e^{-S_{\text{int}}[s+f]}\rangle_f\,, \tag{B.2}$$

where $\langle\mathcal{O}\rangle_f \equiv \frac{1}{Z_0^f}\int\mathcal{D}f\,\mathcal{O}\,e^{-S_0[f]}$ denotes averaging over the fast fields and $Z_0^f \equiv \int\mathcal{D}f\,e^{-S_0[f]}$. With this, an effective action only containing slow modes can be obtained via

$$\begin{aligned} S_{\text{eff}}[s] = S_0[s] - \log\langle e^{-S_{\text{int}}[s+f]}\rangle_f = S_0[s] + S^{(1)}[s] - \frac{1}{2}\left[S^{(2)}[s] - (S^{(1)}[s])^2\right] \\ + \mathcal{O}(u^3, g^3, u^2 g, u g^2) \end{aligned} \tag{B.3}$$

where $S^{(n)}[s] \equiv \langle(S_{\text{int}}[s+f])^n\rangle_f$.

The first order contributions evaluate to

$$\langle\cos 2\beta\phi\rangle_f = \cos 2\beta\phi_s\left(1 - \frac{\beta^2}{\pi}l\right), \quad \langle\bar{\chi}\chi\sin\beta\phi\rangle_f = \bar{\chi}_s\chi_s\sin\beta\phi_s\left(1 - \frac{\beta^2}{4\pi}l\right), \tag{B.4}$$

such that the flow equations at this level read

$$\frac{du}{dl} = 2u\left(1 - \frac{\beta^2}{2\pi}\right), \quad \frac{dg}{dl} = g\left(1 - \frac{\beta^2}{4\pi}\right). \tag{B.5}$$

Note that the mass and self-interaction of the bosonic field become irrelevant for $\beta^2 > 2\pi$, while the fermion-boson interaction becomes irrelevant for $\beta^2 > 4\pi$.

For the second order terms, one needs the fact that

$$\begin{aligned}&\left\langle\cos 2\beta\phi(r)\cos 2\beta\phi(r')\right\rangle_f - \left\langle\cos 2\beta\phi(r)\right\rangle_f \left\langle\cos 2\beta\phi(r')\right\rangle_f \\ &= \frac{1}{2}\sum_{\sigma=\pm}\cos 2\beta(\phi_s(r)+\sigma\phi_s(r'))e^{-2\beta^2 l/\pi}\left[\exp\left(-4\sigma\beta^2\int_f \frac{d^2p}{(2\pi)^2}\frac{\cos p\cdot(r-r')}{p^2}\right)-1\right],\end{aligned} \tag{B.6}$$

where $r=(y,c\tau)$, $p=(q,\omega/c)$ and $\int_f d^2p$ implies integration over the fast momenta only. Since the integral over p only includes values $|p|\simeq\Lambda$, the main contribution to it stems from $|r-r'|\lesssim\Lambda^{-1}$. Followingly, we can introduce the center of mass $R=(r+r')/2$ and relative coordinates $\delta r = r-r'$ and expand in small $\Lambda\,\delta r$.

For $\sigma=+1$ then, the resulting operator is proportional to $\cos 4\beta\phi_s$, which we have seen to be irrelevant if $\beta^2>\pi/2$. Since we will focus on the region where either u or g are marginal, i.e. $2\pi\lesssim\beta^2\lesssim 4\pi$, we discard this term and only keep the $\sigma=-1$-contribution.

Performing a gradient expansion of the cosine

$$\cos 2\beta(\phi_s(r)-\phi_s(r'))\simeq \text{const.}-2\beta^2(\delta r\cdot\partial_R\phi_s)^2, \tag{B.7}$$

we finally find

$$\begin{aligned}&\int d^2r d^2r'\left[\left\langle\cos 2\beta\phi(r)\cos 2\beta\phi(r')\right\rangle_f-\left\langle\cos 2\beta\phi(r)\right\rangle_f\left\langle\cos 2\beta\phi(r')\right\rangle_f\right]\\ &\qquad\simeq -\frac{2\beta^4 C_1}{\Lambda^4} l\int d^2R\,(\partial_R\phi_s)^2,\end{aligned} \tag{B.8}$$

where we introduced the numerical constant $C_1\equiv\int_0^\infty d\rho\,\rho^3F(\rho)>0$ with $\int_f\frac{d^2p}{(2\pi)^2}\frac{\cos p\cdot r}{p^2}\equiv\frac{l}{2\pi}F(\Lambda|r|)+\mathcal{O}(l^2)$. For the plots in the main text we used $C_1=8$, as follows from employing a Gaussian cut-off $\int_0^\Lambda dp\to\int_0^\infty dp\,e^{-p^2/\Lambda^2}$.

We proceed similarly for the remaining second-order terms, discarding the generated 4-Majorana- and $\bar\chi\chi\sin 3\beta\phi$-terms as irrelevant in the region of interest. We find

$$\begin{aligned}&\int d^2r\,d^2r'\,\left\langle\bar\chi_f(r)\chi_f(r)\bar\chi_f(r')\chi_f(r')\sin\beta\phi(r)\sin\beta\phi(r')\right\rangle_f\\ &\qquad\simeq-\frac{lc}{\pi v}\int d^2R\,\cos 2\beta\phi_s(R)-\frac{l\beta^2c^2}{2\pi v^2\Lambda^2}\int d\tau\,dy\,\left[\frac{1}{v}(\partial_\tau\phi_s)^2+v(\partial_y\phi_s)^2\right]\end{aligned} \tag{B.9}$$

as well as

$$\begin{aligned}&\int d^2r\,d^2r'\,\bar\chi_s(r)\chi_s(r)\left[\left\langle\sin\beta\phi(r)\cos 2\beta\phi(r')\right\rangle_f-\left\langle\sin\beta\phi(r)\right\rangle_f\left\langle\cos 2\beta\phi(r')\right\rangle_f\right]\\ &\qquad\simeq-\frac{\beta^2C_2}{\Lambda^2}l\int d^2R\,\bar\chi_s(R)\chi_s(R)\sin\beta\phi_s(R)\end{aligned} \tag{B.10}$$

with the numerical constant $C_2\equiv\int_0^\infty d\rho\,\rho F(\rho)>0$ and $C_2=2$ for the Gaussian cut-off.

Plugging these results into (B.3) yields the flow equations (4.6)-(4.9) given in the main text.

B.2 RG flow taking into account irrelevant exchange stiffness

Even though the parameter A' in Eq. (4.4) is strongly irrelevant, in the case $A'\Lambda^2 \gg (-B)$ it is not immediately clear how the (at least initially not neglectable) influence of A' affects the flow. Let us therefore rederive the RG equations at lowest order in $\tilde{u}$ and $\tilde{g}$ taking A' into account. We can write the relevant action as

$$S_{A'} = S + \frac{1}{2}\int \frac{dq\,d\omega}{(2\pi)^2}\frac{\omega^2}{c_0}\frac{A'q^2/B}{1-A'q^2/B}|\phi_{q,\omega}|^2, \tag{B.11}$$

where S is the action given in Eq. (4.5) and $c_0 = c(l=0)$ will not be renormalized. With that, one finds

$$\frac{d\tilde{A}'}{dl} = -2\tilde{A}', \qquad \frac{d\tilde{u}}{dl} = 2\tilde{u}\left(1-\Gamma(\tilde{A}')\frac{\beta^2}{2\pi}\right), \qquad \frac{d\tilde{g}}{dl} = \tilde{g}\left(1-\Gamma(\tilde{A}')\frac{\beta^2}{4\pi}\right) \tag{B.12}$$

with

$$\Gamma(\tilde{A}') = \frac{1}{2\pi}\int_0^{2\pi} d\theta\,\frac{1+\tilde{A}'\cos^2\theta}{\left(\frac{v}{c}\sin^2\theta+\frac{c}{v}\cos^2\theta\right)\left(1+\tilde{A}'\cos^2\theta\right)-\frac{v\tilde{A}'}{c_0}\sin^2\theta\cos^2\theta}, \tag{B.13}$$

where $\tilde{A}' = A'\Lambda^2/(-B)$. Note that $\Gamma(0) = 1$. Let us here for simplicity consider the Lorentz symmetric situation $v = c = c_0$. Then

$$\Gamma(\tilde{A}') = \left(1+\tilde{A}'\right)^{1/4}\cos\left(\frac{1}{2}\arctan\sqrt{\tilde{A}'}\right). \tag{B.14}$$

Generating in Fig. B.1 as an example the same phase diagram as shown in Fig. 4.6b of the main text while taking $\Gamma(\tilde{A}')$ into account, with a value of $\tilde{A}'(0)$ as large as $\tilde{A}'(0) = 100$, clearly shows that quantitative, but no qualitative corrections occur. Considering A' in second order in $\tilde{u}$ and $\tilde{g}$ makes the constants $C_{1/2}$ become dependent on A'. We do not expect this either to lead to any qualitative changes to our findings.

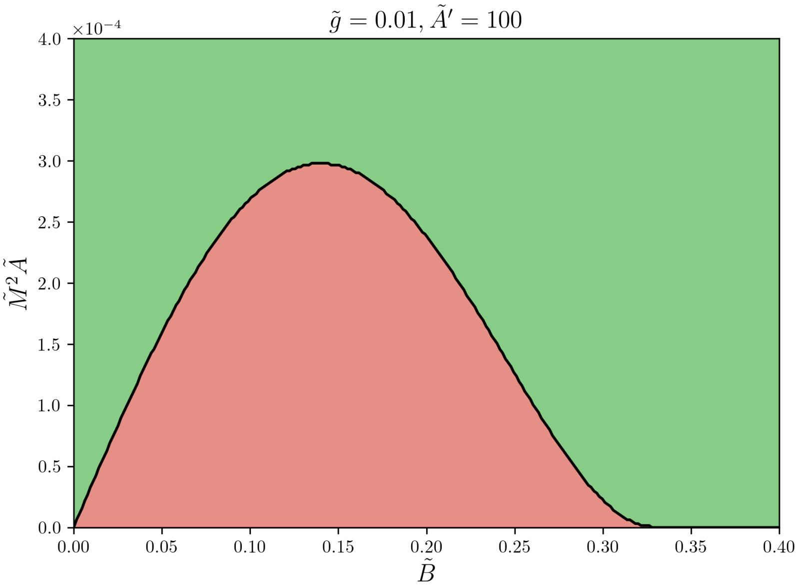

Figure B.1: **Phase diagram taking into account irrelevant exchange stiffness.** Same phase diagram as in Fig. 4.6b, but with $\tilde{A}' = 100$ taken into account. Note the different scale compared to Fig. 4.6b.

C

Appendix C

Supplemental material for Chapter 5

C.1 Symmetries of the BdG Hamiltonian and consequences for matrix elements

C.1.1 Particle-hole symmetry

The particle-hole symmetry of the BdG Hamiltonian h in (5.3) is described by the anti-unitary operator $\mathcal{C} = U_C\mathcal{K}$, where $\mathcal{K}$ denotes complex conjugation and the unitary part is given by $U_C = \tau_y\sigma_y$. It holds $U_C h^* U_C^{-1} = -h$ and thus, given an eigenstate $|n\rangle$ with energy ε_n, an eigenstate with energy $\varepsilon_{-n} = -\varepsilon_n$ exists, for which holds (up to a phase) $|{-n}\rangle = U_C\,|n^*\rangle$.

Consider now a matrix element of the form $\langle m|\tau_z\sigma_y|n\rangle$, relevant in Section 5.2.3. It is

$$\begin{aligned}\langle m|\tau_z\sigma_y|n\rangle &= \langle(-m)^*|U_C\tau_z\sigma_y U_C|(-n)^*\rangle = -\langle(-m)^*|\tau_z\sigma_y|(-n)^*\rangle \\ &= \langle(-m)^*|(\tau_z\sigma_y)^*|(-n)^*\rangle = \langle -m|\tau_z\sigma_y|-n\rangle^* = \langle -n|\tau_z\sigma_y|-m\rangle\,. \qquad \text{(C.1)}\end{aligned}$$

In the same section of the main text we have also made use of the fact that

$$\langle\sigma|\sigma_y|-\sigma\rangle = \langle\sigma|\tau_y|\sigma^*\rangle = \langle\sigma^*|\tau_y|\sigma\rangle^* = -\langle\sigma|\tau_y|\sigma^*\rangle = 0, \qquad \text{(C.2)}$$

where the second equality follows from the hermiticity of τ_y.

C.1.2 Inversion symmetry

For the transverse part of the BdG Hamiltonian h_0, defined in Section 5.2.3, for a given phase difference (at some y) $\varphi(x) = \varphi\,\theta(x)$, it holds

$$h_0^* = e^{i\varphi\tau_z/2}\left(h_0|_{x\to -x}\right)e^{-i\varphi\tau_z/2}, \qquad \text{(C.3)}$$

since

$$\begin{aligned}e^{i\varphi\tau_z/2}\begin{pmatrix}0 & e^{-i\varphi(-x)}\\ e^{i\varphi(-x)} & 0\end{pmatrix}e^{-i\varphi\tau_z/2} &= \begin{pmatrix}0 & e^{i\varphi(1-\theta(-x))}\\ e^{-i\varphi(1-\theta(-x))} & 0\end{pmatrix}\\ &= \begin{pmatrix}0 & e^{i\varphi(x)}\\ e^{-i\varphi(x)} & 0\end{pmatrix}. \qquad \text{(C.4)}\end{aligned}$$

Thus for the eigenmodes $\xi_n(x)$ it holds (up to a phase),

$$\xi_n^*(x) \propto e^{i\varphi\tau_z/2}\xi_n(-x). \tag{C.5}$$

It follows

$$\begin{aligned}\langle n|\tau_z\sigma_y|n\rangle = \langle n|\tau_z\sigma_y|n\rangle^* = -\langle n^*|\tau_z\sigma_y|n^*\rangle &= -\langle n|e^{-i\varphi\tau_z/2}\tau_z\sigma_y e^{i\varphi\tau_z/2}|n\rangle \\ &= -\langle n|\tau_z\sigma_y|n\rangle = 0.\end{aligned} \tag{C.6}$$

By the same logic $\langle n|\tau_0\sigma_y|n\rangle = 0$.

In fact, the inversion symmetry holds even for the full Hamiltonian (5.3). The y-dependence, which the unitary transformation in (C.3) obtains via $\varphi(y)$, is then crucial, since the additional contribution following from the inversion of the vector potential

$$A_y(-x)\sigma_y = -A_y(x)\sigma_y + \frac{\pi}{l_B}\sigma_y \tag{C.7}$$

is compensated by the extra contribution stemming from

$$e^{i\varphi(y)\tau_z/2}\left(-i\tau_z\sigma_y\partial_y\right)e^{-i\varphi(y)\tau_z/2} = -i\tau_z\sigma_y\partial_y - \frac{1}{2}\varphi'(y)\sigma_y, \tag{C.8}$$

since $\varphi'(y) = 2\pi/l_B$.

C.2 Second-order corrections to the effective Hamiltonian

Plugging (5.30) into the right hand side of Eq. (5.29), it follows

$$\begin{aligned}&\left[-\frac{i}{2}\{v_{\text{eff}}(y),\partial_y\}\right]\alpha_{-\sigma}(y) - (E-\varepsilon_\sigma(y))\alpha_\sigma(y) \\ &\quad= -\sum_{n\neq\pm1}\sum_{l\neq n}\left[-iv_{\sigma n}(y)\partial_y - \tilde{B}_{\sigma n}(y)\right]\frac{1}{E-\varepsilon_n(y)+\tilde{B}_{nn}(y)}\left[-iv_{nl}(y)\partial_y - \tilde{B}_{nl}(y)\right]\alpha_l(y).\end{aligned} \tag{C.9}$$

We next approximate in the denominator $E-\varepsilon_n(y)+\tilde{B}_{nn}(y) \approx -\varepsilon_n(y) = \varepsilon_{-n}(y)$. Furthermore, in the sum over l we once again assume the contributions by $l \neq \pm1$ to be negligible compared to the low-energy contributions and are thus left to evaluate

$$\begin{aligned}&\sum_{n\neq\pm1}\left[-iv_{\sigma n}(y)\partial_y - \tilde{B}_{\sigma n}(y)\right]\frac{1}{\varepsilon_n(y)}\left[-iv_{n,\sigma'}(y)\partial_y - \tilde{B}_{n,\sigma'}(y)\right] \\ &= \sum_{n\neq\pm1}\Big[-\frac{1}{\varepsilon_n(y)}v_{\sigma n}(y)v_{n\sigma'}(y)\frac{\partial^2}{\partial y^2} \\ &\qquad -\frac{1}{\varepsilon_n(y)}\Big(v_{\sigma n}(y)v'_{n\sigma'}(y) - i\tilde{B}_{\sigma n}(y)v_{n\sigma'}(y) - iv_{\sigma n}(y)\tilde{B}_{n\sigma'}(y)\Big)\frac{\partial}{\partial y} \\ &\qquad +\frac{1}{\varepsilon_n(y)}\Big(iv_{\sigma n}(y)\tilde{B}'_{n\sigma'}(y) + \tilde{B}_{\sigma n}(y)\tilde{B}_{n\sigma'}(y)\Big)\Big] \\ &\qquad + \sum_{n\neq\pm1}\frac{\varepsilon'_n(y)}{\varepsilon_n^2(y)}\Big[v_{\sigma n}(y)v_{n\sigma'}(y)\frac{\partial}{\partial y} - iv_{\sigma n}(y)\tilde{B}_{n\sigma'}(y)\Big]\end{aligned} \tag{C.10}$$

with $\sigma' = \pm\sigma$. From charge conjugation symmetry, it follows

$$v_{nm} = v_{-m,-n}, \qquad \tilde{B}_{nm} = i\partial_y v_{-m,-n} - \tilde{B}_{-m,-n} = i\partial_y v_{n,m} + \tilde{B}^*_{m,n}. \tag{C.11}$$

With this, we find the coefficient in front of the second derivative

$$\partial_y^2 : \qquad -\sum_{n\neq\pm1} \frac{v_{\sigma n}(y) v_{n\sigma'}(y)}{\varepsilon_n(y)} = \mathcal{A}(y)\rho_z^{\sigma,\sigma'} \tag{C.12}$$

where

$$\mathcal{A}(y) \equiv -\sum_{n\neq\pm1} \frac{v_{+1,n}(y)v_{n,+1}(y)}{\varepsilon_n(y)} = -\sum_{n\neq\pm1} \frac{|v_{+1,n}(y)|^2}{\varepsilon_n(y)} = -\langle\xi_{+1}|\,\tau_z\sigma_y P\tau_z\sigma_y\,|\xi_{+1}\rangle \tag{C.13}$$

$$\text{with} \qquad P \equiv \sum_{n\neq\pm1} \frac{|n\rangle\langle n|}{\varepsilon_n(y)} = \sum_{n\neq\pm1} \frac{|n\rangle\langle n| - |-n\rangle\langle -n|}{2\varepsilon_n(y)}. \tag{C.14}$$

Furthermore, the expression multiplying the first derivative then yields

$$\partial_y : \qquad \mathcal{A}'(y)\rho_z^{\sigma,\sigma'} + i\delta\tilde{v}_0(y)\rho_0^{\sigma,\sigma'} + i\delta\tilde{v}_x(y)\rho_x^{\sigma,\sigma'} + i\delta\tilde{v}_y(y)\rho_y^{\sigma,\sigma'} \tag{C.15}$$

where

$$\delta\tilde{v}_0 = \mathrm{Re}(\delta\tilde{v}_+), \quad \delta\tilde{v}_z = \mathrm{Im}(\delta\tilde{v}_+), \quad \delta\tilde{v}_x = \mathrm{Re}(\delta\tilde{v}_-), \quad \delta\tilde{v}_y = \mathrm{Im}(\delta\tilde{v}_-), \tag{C.16}$$

with

$$\delta\tilde{v}_\pm \equiv 2\sum_{n\neq\pm1} \frac{v_{\pm1,n}\tilde{B}_{n,+1}}{\varepsilon_n} = 2i\,\langle\xi_{\pm1}|\,\tau_z\sigma_y P\tau_z\sigma_y\,|\partial_y\xi_{+1}\rangle\,. \tag{C.17}$$

Finally, for the contributions without derivative, we obtain

$$\begin{aligned} 1 : \qquad & \frac{i}{2}\left(\delta\tilde{v}_0(y)\right)'\rho_0^{\sigma,\sigma'} - \left[\mathcal{D}(y) + \frac{1}{2}\left(\delta\tilde{v}_z(y)\right)'\right]\rho_z^{\sigma,\sigma'} + \\ & \frac{i}{2}\left(\delta\tilde{v}_x(y)\right)'\rho_x^{\sigma,\sigma'} + \frac{i}{2}\left(\delta\tilde{v}_y(y)\right)'\rho_y^{\sigma,\sigma'} \end{aligned} \tag{C.18}$$

with

$$\mathcal{D}(y) \equiv -\sum_{n\neq\pm1} \frac{|\tilde{B}_{n,+1}|^2}{\varepsilon_n} = -\langle\partial_y\xi_{+1}|\tau_z\sigma_y P\tau_z\sigma_y|\partial_y\xi_{+1}\rangle\,. \tag{C.19}$$

All in all, including the second-order corrections, the effective Hamiltonian thus is of the form

$$\begin{aligned} h_{\text{eff}}^{(\text{corr})} = & -\frac{1}{2}\left\{i\partial_y, v_{\text{eff}}(y) + \delta\tilde{v}_x(y)\right\}\rho_x - \frac{1}{2}\left\{i\partial_y, \delta\tilde{v}_y(y)\right\}\rho_y \\ & -\partial_y\left(\mathcal{A}(y)\partial_y\right)\rho_z - \frac{1}{2}\left\{i\partial_y, \delta\tilde{v}_0(y)\right\}\rho_0 + \left[\varepsilon(y) + B_z(y) + \mathcal{D}(y) + \frac{1}{2}\left(\delta\tilde{v}_z(y)\right)'\right]\rho_z. \end{aligned} \tag{C.20}$$

Note that all additional terms comply with the charge conjugation symmetry, the unitary part of which on this level is given by $U_C = \rho_x$.

C.3 Generalized set of harmonic oscillator eigenfunctions

The Schrödinger equation for the harmonic oscillator of the form

$$\left(-\frac{d^2}{dz^2}+z^2\right)\phi(z)=K\phi(z) \tag{C.21}$$

has a well known normalizable solution if $K=2n+1$, $n\in\mathbb{N}_0$. In Section 5.3, we are interested in the complete set of solutions to this equation for arbitrary values of K, regardless of normalizability. In Ref. [123], these are shown to be given by

$$\begin{aligned}\phi_0^K(z)&=M\left(\frac{1-K}{4},\frac{1}{2},z^2\right)e^{-z^2/2},\\ \phi_1^K(z)&=z\,M\left(\frac{3-K}{4},\frac{3}{2},z^2\right)e^{-z^2/2}\end{aligned} \tag{C.22}$$

with the confluent hypergeometric function $M(a,b,x)$. The ladder operators

$$a=\frac{1}{\sqrt{2}}\left(\frac{d}{dz}+z\right),\quad a^\dagger=\frac{1}{\sqrt{2}}\left(-\frac{d}{dz}+z\right) \tag{C.23}$$

act on these in the following way:

$$\begin{aligned}a\phi_0^K(z)&=(1-K)\phi_1^{K-2}(z),\quad &a\phi_1^K(z)&=\phi_0^{K-2}(z),\\ a^\dagger\phi_0^K(z)&=(1+K)\phi_1^{K+2}(z),\quad &a^\dagger\phi_1^K(z)&=-\phi_0^{K+2}(z).\end{aligned} \tag{C.24}$$

C.4 Confirmation of results from Ref. [114]

In Ref. [114] (in the case of zero magnetization $M=0$) the energies and wavefunctions of the CdGM states bound to a Josephson vortex have been derived using the method presented in Section 5.2.2 of this thesis. Here, we compare and confirm the results using the approach of the spectral matrix $M(E)$ (see Section 5.3) for one example set of parameters. In Fig. C.1a, the absolute value of the lowest eigenvalue of $M(E)$ is shown as a function of E. Since eigenmodes of the Hamiltonian correspond to zero modes of M, we expect zero eigenvalues at the energies predicted by the formulas taken from Ref. [114], indicated by the red dashed lines. Indeed, we find that the results closely match, with the agreement becoming increasingly worse for higher excited states. In Figs. C.1b-C.1e, the probability densities for the zero-energy state (MBS) and the first three excited states are plotted and shown to closely resemble the predicted form of the wave functions (for exemplary purposes we chose an offset $\varphi_0=\pi/2$ of the phase difference which shifts the Josephson vortex from being centered at $l_B/2$ to $l_B/4$).

For demonstration purposes, in Fig. C.2 we also show the two degenerate zero-energy states, localized with a distance l_B between each other, we find if we choose $n=2$ flux quanta to be trapped in the junction.

C.5 Introducing asymmetry to the junction

As mentioned in the main text, the additional zero modes we find to emerge by tuning μ_N in Section 5.4 are not robust under breaking of the x-inversion symmetry. Since in any real

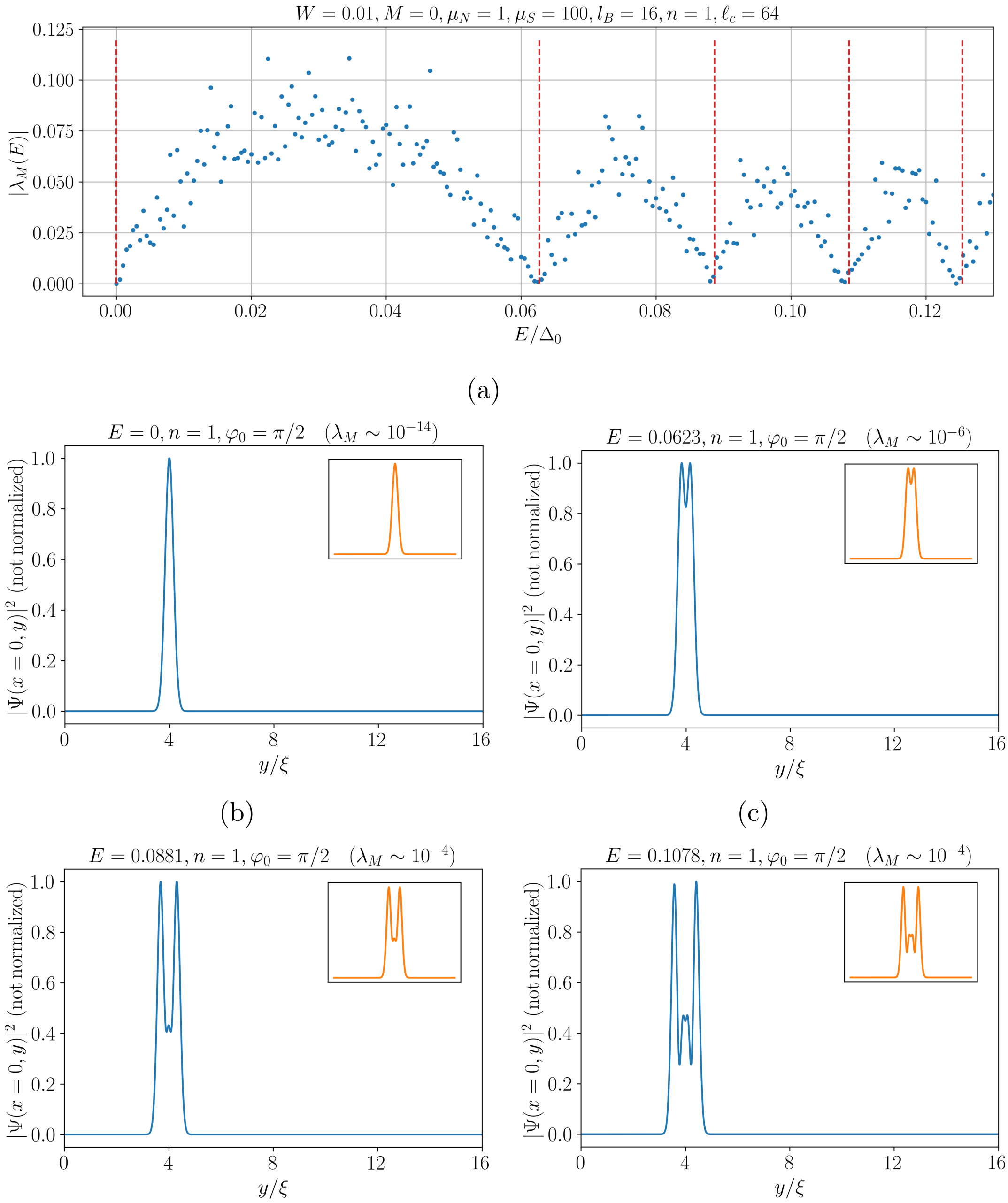

(a)

(b) (c)

(d) (e)

Figure C.1: **CdGM spectrum in the Andreev regime** (a) Absolute value of the lowest-lying eigenvalue $\lambda_M(E)$ of the spectral matrix $M(E)$ for the parameters given above the plot. The red dashed lines indicate the spectrum found in Ref. [114], which closely matches the occurrences of $\lambda_M = 0$ we find here. (b)-(e) Probability densities of the determined CdGM states along a slice at $x = 0$. The profiles are in agreement with the ones predicted in Ref. [114], shown in the insets. Note that for demonstration purposes we chose $\varphi = \pi/2$, leading to the states being localized at $y = l_B/4$.

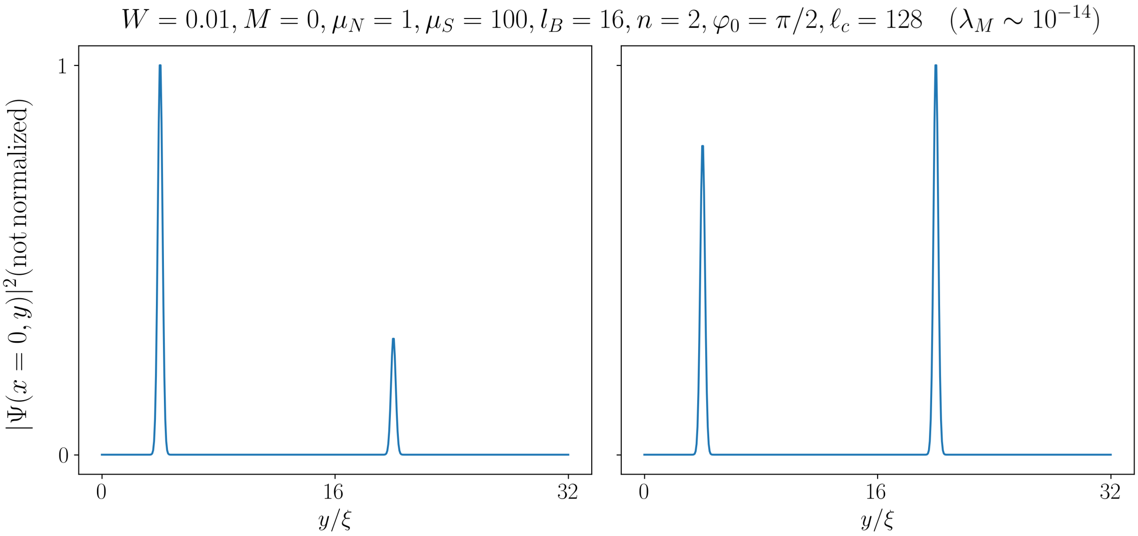

Figure C.2: **Two degenerate zero modes** for $n = 2$ Josepshon vortices in the Andreev regime. Depicted are arbitrary linearly independent superpositions of the two localized solutions at $y_1 = l_B/4$ and $y_2 = y_1 + l_B$.

system irregularities of the width, chemical potential and induced superconducting gap have to be expected to be present, these modes will thus appear at low, but non-zero energies. In Fig. C.3 we show the spectral flow for the case of $\Delta_0(x > W/2) \neq \Delta_0(x < W/2)$ (differing by one percent) and see, compared to Figs. 5.6a, 5.6b and 5.7a, that for $\mu_N > \mu_N^{(c)}$ indeed the first excited state does not become a zero mode but remains at a constant non-zero energy instead.

In accordance, in Fig. C.4 the additional Dirac cones we observed in Fig. 5.9c are gapped out under these circumstances.

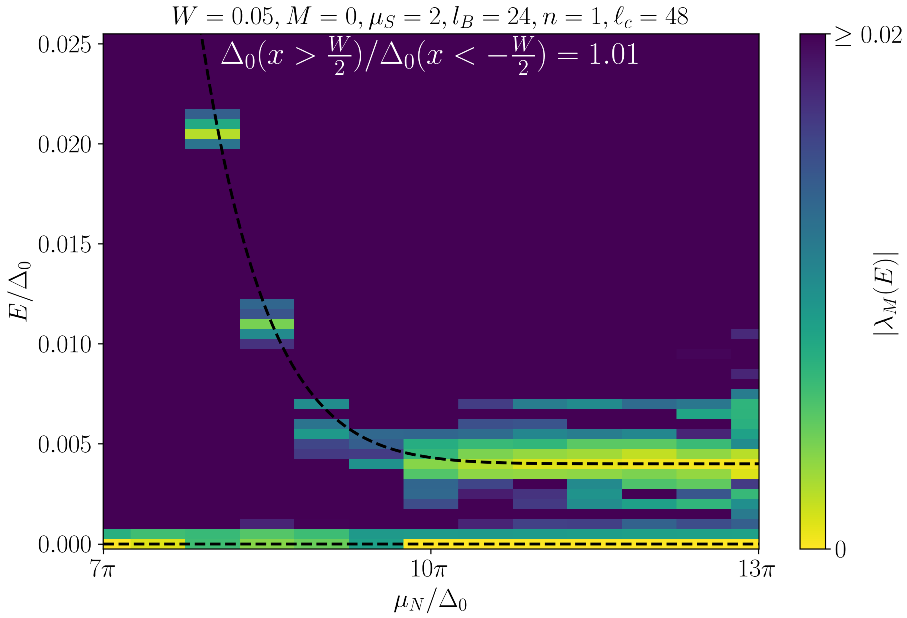

Figure C.3: **Spectral flow for asymmetric superconducting gaps**, breaking the x-inversion symmetry. It can be observed that the previously found emergent zero modes instead remain at a constant, finite energy. The black dashed lines serve as guide to the eye. Note the different energy scale compared to Fig. 5.7a.

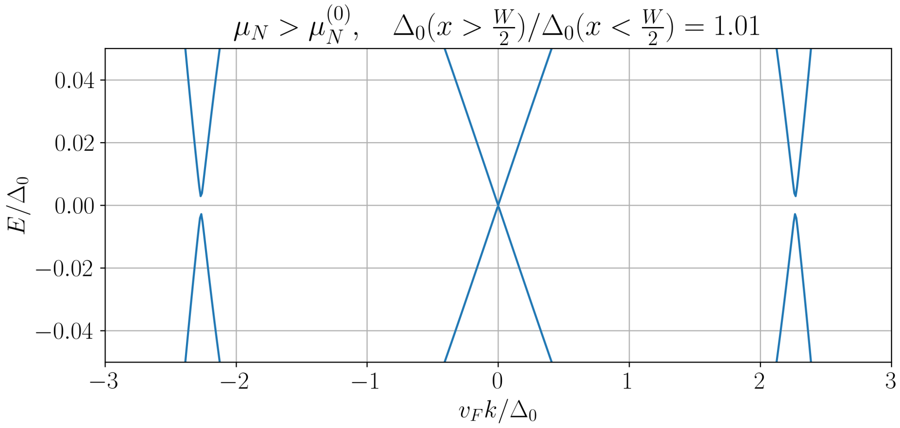

Figure C.4: **Dispersion of the one-dimensional bound states for asymmetric superconducting gaps** for a value of $\mu_N/\Delta_0 = 5.5\pi$ at a phase difference of $\varphi = \pi$. The rest of the parameters are chosen as in Fig. C.3. While the crossing at $k = 0$ is robust against the breaking of x-inversion symmetry, the two additional Dirac points become gapped (note the different energy scale in comparison to Fig. 5.9c to make the gaps more clearly visible).

List of Abbreviations

ABS	Andreev bound state
BCS	Bardeen-Cooper-Schrieffer
BKT	Berezinskii-Kosterlitz-Thouless
BdG	Bogoliubov-de Gennes
CdGM	Caroli-de Gennes-Matricon
CFT	Conformal field theory
LLG	Landau-Lifshitz-Gilbert
MBS	Majorana bound state
MZM	Majorana zero mode
RG	renormalization group
SMS	superconductor-ferromagnet-superconductor
STIS	superconductor-topological insulator-superconductor
SOI	spin-orbit interaction
TCI	tricritical Ising
TI	topological insulator
TRITOPS	time-reversal invariant topological superconductor

List of Figures

Acknowledgments

First and foremost, I would like to express my sincere gratitude to my advisor, Alexander Shnirman. His insights and physical intuition have been invaluable to the creation of this work, as have the encouragements and guidance he provided me with since my master's studies. I am truly grateful for his continuous support and to have had the pleasure of learning from him during these past years.

I am immensely thankful to Jörg Schmalian, not only for agreeing to be my second reviewer, but more importantly for giving me the opportunity to benefit from his deep understanding of physics and his unwavering enthusiasm, in our joint projects and beyond.

I would also like to thank my collaborators, all of whom it has been a pleasure working with. Especially, I would like to express my gratitude to Erez Berg, Gabriel F. R. Ruiz, Liliana Arrachea, Dmitriy Shapiro, Eytan Grosfeld and Kiryl Piasotski, as well as Alexander Mirlin, for many insightful discussions which this thesis has greatly benefited from.

I am furthermore thankful to all my current and former colleagues at TKM for creating a supportive and pleasant working environment, which made the past years both productive and enjoyable.

The organizers and members of the KIT Graduate School of Quantum Matter (KSQM) are very much appreciated as well. Not only have I learned a lot during the retreats, events and workshops, but it also gave me the opportunity to meet many great people who I immensely enjoyed spending time with.

Very special thanks goes to Jan-Phillip Föst and Svenja Heyns for proofreading of this thesis and, above all, for keeping me sane when life got stressful. I could not have asked for better friends with whom to share this physics journey (as well as many a coffee) from the very beginning.

Finally, I would like to thank my family for their abundant and unconditional support, patience and understanding. I do not take it for granted.

Bibliography

[1] L. Sciascia, *La scomparsa di Majorana* (Einaudi, 1975).
(Cited on page 1.)

[2] J. Francese, “Leonardo Sciascia and The Disappearance of Majorana”, Journal of Modern Italian Studies **15**, 715–733 (2010).
(Cited on page 1.)

[3] E. Palma, “La Procura: Ettore Majorana vivo in Venezuela fra il 1955 e il 1959”, Corriere della Sera (2015).
(Cited on page 1.)

[4] E. Majorana, “Teoria simmetrica dell’elettrone e del positrone”, Il Nuovo Cimento **14**, 171–184 (1937).
(Cited on page 1.)

[5] F. Wilczek, “Majorana returns”, Nature Physics **5**, 614–618 (2009).
(Cited on page 1.)

[6] J. Bardeen, L. N. Cooper, and J. R. Schrieffer, “Theory of Superconductivity”, Physical Review **108**, 1175–1204 (1957).
(Cited on page 1.)

[7] G. Volovik, “Fermion zero modes on vortices in chiral superconductors”, Journal of Experimental and Theoretical Physics Letters **70**, 609–614 (1999).
(Cited on page 1.)

[8] N. Read and D. Green, “Paired states of fermions in two dimensions with breaking of parity and time-reversal symmetries, and the fractional quantum Hall effect”, Physical Review B **61**, 10267–10297 (2000).
(Cited on pages 1, 8, 10.)

[9] D. A. Ivanov, “Non-abelian statistics of half-quantum vortices in p-wave superconductors”, Physical Review Letters **86**, 268–271 (2001).
(Cited on pages 1, 10.)

[10] A. Y. Kitaev, “Unpaired Majorana fermions in quantum wires”, Physics-Uspekhi **44**, 131 (2001).
(Cited on pages 1, 10.)

[11] C. Nayak, S. H. Simon, A. Stern, M. Freedman, and S. Das Sarma, “Non-abelian anyons and topological quantum computation”, Reviews of Modern Physics **80**, 1083–1159 (2008).
(Cited on pages 1, 10.)

[12] Microsoft Azure Quantum, M. Aghaee, A. Alcaraz Ramirez, Z. Alam, R. Ali, M. Andrzejczuk, A. Antipov, M. Astafev, A. Barzegar, B. Bauer, et al., “Interferometric single-shot parity measurement in InAs–Al hybrid devices”, Nature **638**, 651–655 (2025).
(Cited on page 1.)

[13] L. Fu and C. L. Kane, “Superconducting Proximity Effect and Majorana Fermions at the Surface of a Topological Insulator”, Physical Review Letters **100**, 096407 (2008).
(Cited on pages 1, 2, 10–12, 15, 17, 53, 54, 71, 73, 81.)

[14] J. Alicea, “New directions in the pursuit of Majorana fermions in solid state systems”, Reports on Progress in Physics **75**, 076501 (2012).
(Cited on pages 1, 5, 10.)

[15] J. R. Williams, A. J. Bestwick, P. Gallagher, S. S. Hong, Y. Cui, A. S. Bleich, J. G. Analytis, I. R. Fisher, and D. Goldhaber-Gordon, “Unconventional Josephson effect in hybrid superconductor-topological insulator devices”, Physical Review Letters **109**, 056803 (2012).
(Cited on page 2.)

[16] M. Veldhorst, M. Snelder, M. Hoek, T. Gang, V. Guduru, X. Wang, U. Zeitler, W. G. van der Wiel, A. Golubov, H. Hilgenkamp, et al., “Josephson supercurrent through a topological insulator surface state”, Nature Materials **11**, 417–421 (2012).
(Cited on page 2.)

[17] I. Sochnikov, L. Maier, C. A. Watson, J. R. Kirtley, C. Gould, G. Tkachov, E. M. Hankiewicz, C. Brüne, H. Buhmann, L. W. Molenkamp, and K. A. Moler, “Nonsinusoidal current-phase relationship in Josephson junctions from the 3D topological insulator HgTe”, Physical Review Letters **114**, 066801 (2015).
(Cited on page 2.)

[18] M. Kayyalha, A. Kazakov, I. Miotkowski, S. Khlebnikov, L. P. Rokhinson, and Y. P. Chen, “Highly skewed current–phase relation in superconductor–topological insulator–superconductor Josephson junctions”, npj Quantum Materials **5**, 7 (2020).
(Cited on page 2.)

[19] J. Wiedenmann, E. Bocquillon, R. S. Deacon, S. Hartinger, O. Herrmann, T. M. Klapwijk, L. Maier, C. Ames, C. Brüne, C. Gould, A. Oiwa, K. Ishibashi, S. Tarucha, H. Buhmann, and L. W. Molenkamp, “4π-periodic Josephson supercurrent in HgTe-based topological Josephson junctions”, Nature Communications **7**, 10303 (2016).
(Cited on page 2.)

[20] C. Kurter, A. D. Finck, Y. S. Hor, and D. J. Van Harlingen, “Evidence for an anomalous current–phase relation in topological insulator Josephson junctions”, Nature Communications **6**, 7130 (2015).
(Cited on page 2.)

[21] G. Yue, C. Zhang, E. D. Huemiller, J. H. Montone, G. R. Arias, D. G. Wild, J. Y. Zhang, D. R. Hamilton, X. Yuan, X. Yao, D. Jain, J. Moon, M. Salehi, N. Koirala, S. Oh, and D. J. Van Harlingen, “Signatures of Majorana bound states in the diffraction patterns of extended superconductor–topological insulator–superconductor Josephson junctions”, Physical Review B **109**, 094511 (2024).
(Cited on pages 2, 54.)

[22] Y. Tanaka, T. Yokoyama, and N. Nagaosa, “Manipulation of the Majorana Fermion, Andreev Reflection, and Josephson Current on Topological Insulators”, Physical Review Letters **103**, 107002 (2009).
(Cited on pages 2, 15.)

[23] A. Zyuzin, M. Alidoust, and D. Loss, “Josephson Junction through a Disordered Topological Insulator with Helical Magnetization”, Physical Review B **93**, 214502 (2016).
(Cited on pages 2, 15.)

[24] M. Amundsen, H. G. Hugdal, A. Sudbo, and J. Linder, “Vortex spin valve on a topological insulator”, Physical Review B **98**, 144505 (2018).
(Cited on pages 2, 15.)

[25] S. Backens and A. Shnirman, “Current–phase relation in a topological Josephson junction: Andreev bands vs. scattering states”, Physical Review B **103**, 115423 (2021).
(Cited on pages 2, 15, 54.)

[26] M. Z. Hasan and C. L. Kane, “Topological Insulators”, Reviews of Modern Physics **82**, 3045–3067 (2010).
(Cited on page 5.)

[27] R. Aguado, “Majorana quasiparticles in condensed matter”, La Rivista del Nuovo Cimento **40**, 523–593 (2017).
(Cited on page 5.)

[28] P. A. M. Dirac, “Quantised singularities in the electromagnetic field”, Proceedings of the Royal Society of London. Series A, Containing Papers of a Mathematical and Physical Character **133**, 60–72 (1931).
(Cited on page 6.)

[29] D. J. Thouless, M. Kohmoto, M. P. Nightingale, and M. den Nijs, “Quantized Hall conductance in a two-dimensional periodic potential”, Physical Review Letters **49**, 405–408 (1982).
(Cited on page 6.)

[30] B. I. Halperin, “Quantized Hall conductance, current-carrying edge states, and the existence of extended states in a two-dimensional disordered potential”, Physical Review B **25**, 2185–2190 (1982).
(Cited on page 6.)

[31] C. L. Kane and E. J. Mele, “Quantum spin Hall effect in graphene”, Physical Review Letters **95**, 226801 (2005).
(Cited on page 7.)

[32] B. A. Bernevig, T. L. Hughes, and S.-C. Zhang, “Quantum spin Hall effect and topological phase transition in HgTe quantum wells”, Science **314**, 1757–1761 (2006).
(Cited on page 7.)

[33] M. König, S. Wiedmann, C. Brüne, A. Roth, H. Buhmann, L. W. Molenkamp, X.-L. Qi, and S.-C. Zhang, “Quantum spin Hall insulator state in HgTe quantum wells”, Science **318**, 766–770 (2007).
(Cited on page 7.)

[34] L. Fu, C. L. Kane, and E. J. Mele, “Topological insulators in three dimensions”, Physical Review Letters **98**, 106803 (2007).
(Cited on page 8.)

[35] D. Hsieh, D. Qian, L. Wray, Y. Xia, Y. S. Hor, R. J. Cava, and M. Z. Hasan, “A topological Dirac insulator in a quantum spin Hall phase”, Nature **452**, 970–974 (2008).
(Cited on page 8.)

[36] R. Jackiw and C. Rebbi, “Solitons with fermion number $\frac{1}{2}$”, Physical Review D **13**, 3398–3409 (1976).
(Cited on pages 9, 28.)

[37] C. Chamon, R. Jackiw, Y. Nishida, S.-Y. Pi, and L. Santos, “Quantizing Majorana fermions in a superconductor”, Physical Review B **81**, 224515 (2010).
(Cited on page 9.)

[38] M. Stone and R. Roy, “Edge modes, edge currents, and gauge invariance in p_x+ip_y superfluids and superconductors”, Physical Review B **69**, 184511 (2004).
(Cited on page 10.)

[39] W. Qin, J. Gao, P. Cui, and Z. Zhang, "Two-dimensional superconductors with intrinsic p-wave pairing or nontrivial band topology", Science China Physics, Mechanics & Astronomy **66**, 267005 (2023).
(Cited on page 10.)

[40] A. Volkov, P. Magnée, B. van Wees, and T. Klapwijk, "Proximity and Josephson effects in superconductor-two-dimensional electron gas planar junctions", Physica C: Superconductivity **242**, 261–266 (1995).
(Cited on page 10.)

[41] L. Fu and C. L. Kane, "Probing Neutral Majorana Fermion Edge Modes with Charge Transport", Physical Review Letters **102**, 216403 (2009).
(Cited on pages 11, 17, 53.)

[42] A. Barone and G. Paterno, *Physics and applications of the Josephson effect* (Wiley, 1982).
(Cited on pages 13, 14, 30, 35.)

[43] E. Grosfeld and A. Stern, "Observing majorana bound states of josephson vortices in topological superconductors", PNAS **108**, 11810–11814 (2011).
(Cited on page 13.)

[44] A. C. Potter and L. Fu, "Anomalous supercurrent from Majorana states in topological insulator Josephson junctions", Physical Review B **88**, 121109(R) (2013).
(Cited on pages 13, 54.)

[45] S. S. Hegde, G. Yue, Y. Wang, E. Huemiller, D. J. Van Harlingen, and S. Vishveshwara, "A topological Josephson junction platform for creating, manipulating, and braiding Majorana bound states", Annals of Physics **423**, 168326 (2020).
(Cited on pages 14, 54.)

[46] A. Reich, E. Berg, J. Schmalian, and A. Shnirman, "Magnetization dynamics and Peierls instability in topological Josephson structures", Physical Review B **107**, 245411 (2023).
(Cited on pages v, 15.)

[47] G. F. R. Ruiz, A. Reich, A. Shnirman, J. Schmalian, and L. Arrachea, "Binding zero modes with fluxons in Josephson junctions of time-reversal invariant topological superconductors", Physical Review B **110**, 245427 (2024).
(Cited on pages v, 15, 35, 37.)

[48] L. Landau and E. Lifshitz, "On the theory of the dispersion of magnetic permeability in ferromagnetic bodies", Phys. Z. Sowjetunion **8**, 153–169 (1935).
(Cited on page 15.)

[49] T. Gilbert, "Formulations, foundations and applications of the phenomenological theory of ferromagnetism", Ph. D. dissertation (1956).
(Cited on page 15.)

[50] T. Gilbert, "A Phenomenological Theory of Damping in Ferromagnetic Materials", IEEE Transactions on Magnetics **40**, 3443–3449 (2004).
(Cited on page 15.)

[51] X. Waintal and P. W. Brouwer, "Magnetic exchange interaction induced by a Josephson current", Physical Review B **65**, 054407 (2002).
(Cited on page 16.)

[52] V. Braude and Y. M. Blanter, "Triplet Josephson effect with magnetic feedback in a superconductor-ferromagnet heterostructure", Physical Review Letters **100**, 207001 (2008).
(Cited on page 16.)

[53] F. Konschelle and A. Buzdin, “Magnetic Moment Manipulation by a Josephson Current”, Physical Review Letters **102**, 017001 (2009).
(Cited on page 16.)

[54] I. Kulagina and J. Linder, “Spin supercurrent, magnetization dynamics, and φ-state in spin-textured Josephson junctions”, Physical Review B **90**, 054504 (2014).
(Cited on page 16.)

[55] E. M. Chudnovsky, “Quantum tunneling of the magnetic moment in the S/F/S Josephson φ_0 junction”, Physical Review B **93**, 144422 (2016).
(Cited on page 16.)

[56] M. Nashaat, I. V. Bobkova, A. M. Bobkov, Y. M. Shukrinov, I. R. Rahmonov, and K. Sengupta, “Electrical control of magnetization in superconductor/ferromagnet/superconductor junctions on a three-dimensional topological insulator”, Physical Review B **100**, 054506 (2019).
(Cited on page 16.)

[57] H. Fröhlich, “On the theory of superconductivity: the one-dimensional case”, Proceedings of the Royal Society of London. Series A. Mathematical and Physical Sciences **223**, 296–305 (1954).
(Cited on pages 16, 20.)

[58] C. Abert, “Micromagnetics and spintronics: models and numerical methods”, The European Physical Journal B **92**, 120 (2019).
(Cited on page 17.)

[59] S. Gongyo, Y. Kikuchi, T. Hyodo, and T. Kunihiro, “Effective field theory and the scattering process for magnons in the ferromagnet, antiferromagnet, and ferrimagnet”, Progress of Theoretical and Experimental Physics **2016**, 083B01 (2016).
(Cited on page 17.)

[60] R. H. McKenzie, “Microscopic theory of the pseudogap and Peierls transition in quasi-one-dimensional materials”, Physical Review B **52**, 16428–16442 (1995).
(Cited on page 20.)

[61] R. Peierls, “On Ising’s model of ferromagnetism”, Mathematical Proceedings of the Cambridge Philosophical Society **32**, 477–481 (1936).
(Cited on page 20.)

[62] R. B. Griffiths, “Peierls Proof of Spontaneous Magnetization in a Two-Dimensional Ising Ferromagnet”, Physical Review **136**, A437–A439 (1964).
(Cited on page 20.)

[63] P. A. Lee, T. Rice, and P. W. Anderson, “Conductivity from charge or spin density waves”, Solid State Communications **14**, 703–709 (1974).
(Cited on pages 20, 22.)

[64] S. A. Brazovskiĭ and I. E. Dzyaloshinskiĭ, “Dynamics of one-dimensional electron-phonon systems at low temperatures”, Zh. Eksp. Teor. Fiz. **71**, 2338–2348 (1976).
(Cited on pages 20, 22.)

[65] A. O. Gogolin, A. A. Nersesyan, and A. M. Tsvelik, *Bosonization and strongly correlated systems* (Cambridge University Press, Cambridge, 2004).
(Cited on pages 20, 22, 87.)

[66] S. Kos, A. J. Millis, and A. I. Larkin, “Gaussian fluctuation corrections to the BCS mean-field gap amplitude at zero temperature”, Physical Review B **70**, 214531 (2004).
(Cited on pages 20, 22.)

[67] S. Fischer, M. Hecker, M. Hoyer, and J. Schmalian, “Short-distance breakdown of the Higgs mechanism and the robustness of the BCS theory for charged superconductors”, Physical Review B **97**, 054510 (2018).
(Cited on page 20.)

[68] V. G. Vaks, V. M. Galitskii, and A. I. Larkin, “Collective excitations in a superconductor”, Soviet Physics JETP **14** (1962).
(Cited on pages 21, 82.)

[69] T. Grover, D. N. Sheng, and A. Vishwanath, “Emergent Space-Time Supersymmetry at the Boundary of a Topological Phase”, Science **344**, 280–283 (2014).
(Cited on pages 22, 32, 50, 77.)

[70] A. Rahmani, X. Zhu, M. Franz, and I. Affleck, “Emergent Supersymmetry from Strongly Interacting Majorana Zero Modes”, Physical Review Letters **115**, 166401 (2015).
(Cited on pages 22, 26, 27, 32, 77.)

[71] H. Kleinert, “Collective Quantum Fields”, Fortschritte der Physik **26**, 565–671 (1978).
(Cited on page 22.)

[72] C. M. Varma, “Higgs Boson in Superconductors”, Journal of Low Temperature Physics **126**, 901–909 (2002).
(Cited on page 22.)

[73] Y. Xia, D. Qian, D. Hsieh, L. Wray, A. Pal, H. Lin, A. Bansil, D. Grauer, Y. S. Hor, R. J. Cava, and M. Z. Hasan, “Observation of a large-gap topological-insulator class with a single Dirac cone on the surface”, Nature Physics **5**, 398–402 (2009).
(Cited on pages 26, 48.)

[74] H. Zhang, C.-X. Liu, X.-L. Qi, X. Dai, Z. Fang, and S.-C. Zhang, “Topological insulators in Bi2Se3, Bi2Te3 and Sb2Te3 with a single Dirac cone on the surface”, Nature Physics **5**, 438–442 (2009).
(Cited on pages 26, 48.)

[75] M. Mogi, T. Nakajima, V. Ukleev, A. Tsukazaki, R. Yoshimi, M. Kawamura, K. S. Takahashi, T. Hanashima, K. Kakurai, T.-h. Arima, et al., “Large anomalous Hall effect in topological insulators with proximitized ferromagnetic insulators”, Physical Review Letters **123**, 016804 (2019).
(Cited on pages 26, 48.)

[76] R. Watanabe, R. Yoshimi, M. Kawamura, M. Mogi, A. Tsukazaki, X. Z. Yu, K. Nakajima, K. S. Takahashi, M. Kawasaki, and Y. Tokura, “Quantum anomalous Hall effect driven by magnetic proximity coupling in all-telluride based heterostructure”, Applied Physics Letters **115**, 102403 (2019).
(Cited on pages 26, 48.)

[77] M. Blume, “Theory of the first-order magnetic phase change in UO_2”, Physical Review **141**, 517–524 (1966).
(Cited on page 26.)

[78] H. Capel, “On the possibility of first-order phase transitions in Ising systems of triplet ions with zero-field splitting”, Physica **32**, 966–988 (1966).
(Cited on page 26.)

[79] E. Grosfeld and A. Stern, “Observing Majorana bound states of Josephson vortices in topological superconductors”, Proceedings of the National Academy of Sciences **108**, 11810–11814 (2011).
(Cited on page 28.)

[80] V. E. Zakharov and A. V. Mikhailov, "On the integrability of classical spinor models in two-dimensional space-time", Communications in Mathematical Physics **74**, 21–40 (1980).
(Cited on page 28.)

[81] S. A. Brazovskiĭ, "Self-localized excitations in the Peierls-Fröhlich state", Soviet Physics JETP **51**, 342 (1980).
(Cited on page 28.)

[82] H. Takayama, Y. R. Lin-Liu, and K. Maki, "Continuum model for solitons in polyacetylene", Physical Review B **21**, 2388–2393 (1980).
(Cited on page 28.)

[83] D. A. Takahashi and M. Nitta, "Self-consistent multiple complex-kink solutions in Bogoliubov-de Gennes and chiral Gross-Neveu systems", Physical Review Letters **110**, 131601 (2013).
(Cited on page 28.)

[84] D. A. Takahashi, "Exhaustive derivation of static self-consistent multi-soliton solutions in the matrix Bogoliubov-de Gennes systems", Progress of Theoretical and Experimental Physics **2016**, 043I01 (2016).
(Cited on page 28.)

[85] S. Ryu, A. P. Schnyder, A. Furusaki, and A. W. Ludwig, "Topological insulators and superconductors: tenfold way and dimensional hierarchy", New Journal of Physics **12**, 065010 (2010).
(Cited on page 29.)

[86] X.-L. Qi, T. L. Hughes, S. Raghu, and S.-C. Zhang, "Time-reversal-invariant topological superconductors and superfluids in two and three dimensions", Physical Review Letters **102**, 187001 (2009).
(Cited on page 29.)

[87] L. Fu and E. Berg, "Odd-parity topological superconductors: theory and application to $\mathrm{Cu}_x\mathrm{Bi}_2\mathrm{Se}_3$", Physical Review Letters **105**, 097001 (2010).
(Cited on page 29.)

[88] C. L. Wong and K. T. Law, "Majorana Kramers doublets in $d_{x^2-y^2}$-wave superconductors with Rashba spin-orbit coupling", Physical Review B **86**, 184516 (2012).
(Cited on page 29.)

[89] E. Dumitrescu and S. Tewari, "Topological properties of the time-reversal-symmetric Kitaev chain and applications to organic superconductors", Physical Review B **88**, 220505 (2013).
(Cited on page 29.)

[90] A. Haim, A. Keselman, E. Berg, and Y. Oreg, "Time-reversal-invariant topological superconductivity induced by repulsive interactions in quantum wires", Physical Review B **89**, 220504 (2014).
(Cited on page 29.)

[91] M. S. Scheurer and J. Schmalian, "Topological superconductivity and unconventional pairing in oxide interfaces", Nature communications **6**, 1–10 (2015).
(Cited on page 29.)

[92] A. Haim and Y. Oreg, "Time-reversal-invariant topological superconductivity in one and two dimensions", Physics Reports **825**, 1–48 (2019).
(Cited on pages 29, 30.)

[93] G. F. R. Ruiz, M. A. Rampp, A. A. Aligia, J. Schmalian, and L. Arrachea, "Josephson junctions of two-dimensional time-reversal invariant superconductors: Signatures of the topological phase",

Physical Review B **106**, 195415 (2022).
(Cited on pages 29–32.)

[94] Z. Hermon, A. Stern, and E. Ben-Jacob, "Quantum dynamics of a fluxon in a long circular josephson junction", Physical Review B **49**, 9757–9762 (1994).
(Cited on page 30.)

[95] A. A. Abdumalikov, G. L. Alfimov, and A. S. Malishevskii, "Nonlocal electrodynamics of Josephson vortices in superconducting circuits", Superconductor Science and Technology **22**, 023001 (2009).
(Cited on page 30.)

[96] M. Tinkham, *Introduction to superconductivity*, 2. ed. (Dover Publ., 2004).
(Cited on page 30.)

[97] D. J. Gross and A. Neveu, "Dynamical symmetry breaking in asymptotically free field theories", Physical Review D **10**, 3235–3253 (1974).
(Cited on page 33.)

[98] A. Reich, D. S. Shapiro, and A. Shnirman, "Berezinskii-Kosterlitz-Thouless transitions in a topological superconductor-ferromagnet-superconductor junction", Phys. Rev. B **111**, 205428 (2025).
(Cited on pages v, 39.)

[99] U. Schollwöck, J. Richter, D. J. J. Farnell, and R. F. Bishop, eds., *Quantum Magnetism*, Vol. 645, Lecture Notes in Physics (Springer Berlin Heidelberg, Berlin, Heidelberg, 2004).
(Cited on page 40.)

[100] H. J. Mikeska, "Solitons in a one-dimensional magnet with an easy plane", Journal of Physics C: Solid State Physics **11**, L29–L32 (1977).
(Cited on page 40.)

[101] E. Witten, "Some properties of the $(\bar{\Psi}\Psi)^2$ model in two dimensions", Nuclear Physics B **142**, 285–300 (1978).
(Cited on page 42.)

[102] C. Chen, "From supersymmetric sine-Gordon equation to the superconformal minimal model", arXiv:1908.10777 [cond-mat] (2019).
(Cited on page 43.)

[103] E. Popova, A. F. Franco Galeano, M. Deb, B. Warot-Fonrose, H. Kachkachi, F. Gendron, F. Ott, B. Berini, and N. Keller, "Magnetic anisotropies in ultrathin bismuth iron garnet films", Journal of Magnetism and Magnetic Materials **335**, 139–143 (2013).
(Cited on page 48.)

[104] X. Zhang, Y. Zhao, Q. Song, S. Jia, J. Shi, and W. Han, "Magnetic anisotropy of the single-crystalline ferromagnetic insulator $Cr_2Ge_2Te_6$", Japanese Journal of Applied Physics **55**, 033001 (2016).
(Cited on page 48.)

[105] A. Talalaevskij, M. Decker, J. Stigloher, A. Mitra, H. Körner, O. Cespedes, C. Back, and B. Hickey, "Magnetic properties of spin waves in thin yttrium iron garnet films", Physical Review B **95**, 064409 (2017).
(Cited on page 48.)

[106] M. Mogi, A. Tsukazaki, Y. Kaneko, R. Yoshimi, K. S. Takahashi, M. Kawasaki, and Y. Tokura, "Ferromagnetic insulator $Cr_2Ge_2Te_6$ thin films with perpendicular remanence", APL Materials

6, 091104 (2018).
(Cited on page 48.)

[107] C. Tian, F. Pan, L. Wang, D. Ye, J. Sheng, J. Wang, J. Liu, J. Huang, H. Zhang, D. Xu, et al., “DyOCl: a rare-earth based two-dimensional van der Waals material with strong magnetic anisotropy”, Physical Review B **104**, 214410 (2021).
(Cited on page 48.)

[108] Y. Tian, M. J. Gray, H. Ji, R. J. Cava, and K. S. Burch, “Magneto-elastic coupling in a potential ferromagnetic 2d atomic crystal”, 2D Materials **3**, 025035 (2016).
(Cited on page 48.)

[109] X. Wang, K. Du, Y. Y. Fredrik Liu, P. Hu, J. Zhang, Q. Zhang, M. H. S. Owen, X. Lu, C. K. Gan, P. Sengupta, C. Kloc, and Q. Xiong, “Raman spectroscopy of atomically thin two-dimensional magnetic iron phosphorus trisulfide ($FePS_3$) crystals”, 2D Materials **3**, 031009 (2016).
(Cited on page 48.)

[110] B. Huang, G. Clark, E. Navarro-Moratalla, D. R. Klein, R. Cheng, K. L. Seyler, D. Zhong, E. Schmidgall, M. A. McGuire, D. H. Cobden, et al., “Layer-dependent ferromagnetism in a van der waals crystal down to the monolayer limit”, Nature **546**, 270–273 (2017).
(Cited on page 48.)

[111] L. Huijse, B. Bauer, and E. Berg, “Emergent Supersymmetry at the Ising–Berezinskii-Kosterlitz-Thouless Multicritical Point”, Physical Review Letters **114**, 090404 (2015).
(Cited on pages 50, 78.)

[112] S.-J. Choi and H.-S. Sim, *Josephson junction of finite-size superconductors on a topological insulator under a magnetic field*, arXiv:1908.11403 [cond-mat], Aug. 2019.
(Cited on page 54.)

[113] S. Backens, A. Shnirman, and Y. Makhlin, “Topological Josephson Junction in Transverse Magnetic Field”, JETP Letters **116**, 891–895 (2022).
(Cited on page 54.)

[114] K. Piasotski, O. Lesser, A. Reich, P. Ostrovsky, E. Grosfeld, Y. Makhlin, Y. Oreg, and A. Shnirman, “Current flow in topological insulator josephson junctions due to imperfections”, Phys. Rev. B **111**, 174527 (2025).
(Cited on pages v, 54, 58, 60, 67–69, 73, 79, 94, 95.)

[115] Y. Zhang, Z. Lyu, X. Wang, E. Zhuo, X. Sun, B. Li, J. Shen, G. Liu, F. Qu, and L. Lü, “AC Josephson effect in Corbino-geometry Josephson junctions constructed on Bi_2Te_3 surface”, Chin. Phys. B **31**, 107402 (2022).
(Cited on pages 54, 79.)

[116] J. Y. Park, T. Werkmeister, J. Zauberman, O. Lesser, L. Anderson, Y. Ronen, S. Kushwaha, R. Cava, Y. Oreg, and P. Kim, “Corbino Josephson interferometry on a surface of topological insulator Sn-doped $Bi_{1.1}Sb_{0.9}Te_2S$”, Bulletin of the American Physical Society (2024).
(Cited on pages 54, 79.)

[117] M. Titov and C. W. J. Beenakker, “Josephson effect in ballistic graphene”, Physical Review B **74**, 041401 (2006).
(Cited on pages 54, 73.)

[118] C. Caroli, P. de Gennes, and J. Matricon, “Bound fermion states on a vortex line in a type II superconductor”, Physics Letters **9**, 307–309 (1964).
(Cited on page 54.)

[119] L. Fu and C. L. Kane, “Josephson current and noise at a superconductor/quantum-spin-Hall-insulator/superconductor junction”, Physical Review B **79**, 161408 (2009).
(Cited on page 58.)

[120] G. Teschl, *Ordinary differential equations and dynamical systems*, Vol. 140 (American Mathematical Soc., 2012).
(Cited on page 61.)

[121] K. Piasotski, Private communication, 2025.
(Cited on page 61.)

[122] R. B. Mann, S. M. Morsink, A. E. Sikkema, and T. G. Steele, “Semiclassical gravity in 1+1 dimensions”, Physical Review D **43**, 3948–3957 (1991).
(Cited on page 61.)

[123] I. Sen, “Physical interpretation of non-normalizable harmonic oscillator states and relaxation to pilot-wave equilibrium”, Scientific Reports **14**, 669 (2024).
(Cited on pages 66, 94.)

[124] S. Kushwaha, I. Pletikosić, T. Liang, A. Gyenis, S. Lapidus, Y. Tian, H. Zhao, K. Burch, J. Lin, W. Wang, et al., “Sn-doped $Bi_1.1Sb_{0.9}Te_2S$ bulk crystal topological insulator with excellent properties”, Nature Communications **7**, 11456 (2016).
(Cited on page 73.)

[125] K. Laubscher and J. D. Sau, *Detection of Majorana zero modes bound to Josephson vortices in planar S-TI-S junctions*, arXiv:2411.00756 [cond-mat.mes-hall], 2024.
(Cited on page 73.)

[126] G. V. Dunne and M. Thies, “Time-Dependent Hartree-Fock Solution of Gross-Neveu Models: Twisted-Kink Constituents of Baryons and Breathers”, Physical Review Letters **111**, 121602 (2013).
(Cited on page 78.)

[127] D. A. Takahashi, “Bogoliubov-de Gennes Soliton Dynamics in Unconventional Fermi Superfluids”, Physical Review B **93**, 024512 (2016).
(Cited on page 78.)

[128] O. Foda, “A supersymmetric phase transition in Josephson-tunnel-junction arrays”, Nuclear Physics B **300**, 611–636 (1988).
(Cited on page 78.)

[129] T. Giamarchi, *Quantum physics in one dimension* (Clarendon Press, Oxford, 2004).
(Cited on page 87.)